Petrogenesis of metaophiolitic granulites from SE Anatolia

A Thesis
SUBMITTED TO THE FACULTY OF THE
UNIVERSITY OF MINNESOTA
BY

Mitchell Burgess Awalt

IN PARTIAL FULFILLMENT OF THE REQUIREMENTS
FOR THE DEGREE OF
MASTER OF SCIENCE

Donna L. Whitney, Christian Teyssier

June 2016

Acknowledgements

Thanks to my advisors, Donna Whitney and Christian Teyssier, for giving me the opportunity to engage in this research and participate in the Structure, Tectonics, and Metamorphic Petrology group at the University of Minnesota. Thanks to Côme Lefebvre and Erkan Toraman for their help with samples and field work, as well as numerous discussions about this research. Thanks to Anette von der Handt for her assistance with the microprobe. Thanks also to Jeff Thole and Karth Wirth at Macalester College for use of the SEM, XRF, and sample preparation facilities. I would also like to thank all of the members of the STAMP group for contributing their perspectives, advice, and cheese during many presentations. Finally, thanks to all of my friends and family. Thank you for all of your help and support.

Abstract

High-grade metaophiolitic rocks exposed in the Doğanşehir region of southeastern Anatolia record the evolution of the Southern Neotethys ocean and Tauride plate margin. The Berit metaophiolite contains a suite of granulite and amphibolite facies rocks metamorphosed in the middle Eocene. Granulite facies metagabbroic rocks occur as meter-scale pods hosted by folded amphibolite. The granulite pods are texturally complex, and contain corona structures and symplectites. Coronas of clinopyroxene and garnet around orthopyroxene indicate a prograde path from intermediate- to high-pressure granulite facies. Equilibrium assemblage diagrams (pseudosections) indicate that the granulites partially equilibrated at 700-900 °C and 1.1-1.5 GPa. Corundum-clinopyroxene and kyanite-clinopyroxene symplectites in the granulites suggest rapid isobaric cooling following the thermal peak. Hornblende-plagioclase thermobarometry of the pod-hosting amphibolites indicates retrograde hydration of the granulite facies rocks to 615-700 °C and 0.5-0.8 GPa. Together, textural evidence and pseudosection calculations for the Berit metagabbros show an anticlockwise *P-T* path. The anticlockwise path is attributed to magmatic loading associated with the development of an Eocene magmatic arc. Following cooling of ~150 °C at ~1.2 GPa, extension of the arc exhumed the granulites and was accompanied by fluid infiltration, which produced the retrograde host amphibolite. Folding of the Berit metaophiolitic rocks and associated granitoids is the result of late compression associated with collision. These interpretations suggest consumption of Southern Neotethys oceanic crust continued through the Eocene.

Table of Contents

List of Tables

List of Figures

Introduction

The presence of oceanic lithosphere tectonically emplaced into continental margins (ophiolites) reflects a link between formation at spreading centers and consumption at convergent margins. As such, the processes of ophiolite formation and emplacement are key pieces of the evolution of orogens. In some cases, ophiolites can undergo significant metamorphism and deformation as a result of incorporation into the plate margin (Coleman, 1977; Wakabayashi and Dilek, 2003). In particular, high-grade metaophiolitic rocks require the addition of considerable amount of heat, pressure, and/or fluids. As tectonic settings where oceanic lithosphere can experience these conditions are relatively rare, metaophiolitic rocks can serve as useful records of crustal dynamics and orogenic evolution.

High-grade metamorphism of oceanic rocks than can become incorporated into continental margins are most commonly produced in three settings: 1) subduction complexes, 2) island arc roots, and 3) subophiolitic thrusts (soles). In each of these settings, the metamorphic and structural features of the metaophiolites are characteristic of the processes by which the rocks were formed and, in some cases, emplaced.

Blueschist and eclogite facies metamorphism of mafic rocks has long been recognized as a result of subduction of oceanic lithosphere (Miyashiro, 1961; Ernst, 1973). The descent of refrigerated crust, overlying sediments, and fluids into the mantle results in high-pressure-low-temperature metamorphism as well as complex interactions between the slab and overlying mantle wedge (Peacock, 2003; Faccenda, 2014; Bebout and Penniston-Dorland, 2016). Metamafic blueschist and eclogite are found globally, and

well exposed examples are found in the Franciscan Complex (USA) and the Tavşanlı belt (Turkey) (Okay, 1980; Wakabayashi, 1990).

Metamorphism of mafic crust also occurs in the lower crust of island arcs. The best exposed example of metamorphism in this setting is the Kohistan arc (Pakistan), where lower crustal gabbro was metamorphosed to amphibolite and intermediate- to high-pressure granulite facies by a combination of crustal loading, heating, and contraction (Bard, 1983; Yamamoto, 1993; Petterson, 2010).

High-grade metaophiolitic rocks are also produced by heating of downgoing oceanic crust by overthrust hot oceanic mantle to form metamorphic soles, which are relatively thin (<500 m thick) zones of high strain rocks recognized at the base of many ophiolites (e.g. Samail [Oman], Bay of Islands [Newfoundland]) (Jamieson, 1986; Wakabayashi and Dilek, 2003). These zones show extreme inverted metamorphic gradients (ranging from greenschist to upper amphibolite and granulite facies), and are thought to represent the initiation of subduction and first stages of ophiolite emplacement (Jamieson, 1986; Hacker et al., 1996).

In southeastern Anatolia, consumption of oceanic lithosphere due to closure of the Southern Neotethys led to accretion of ophiolites and terranes that trace the magmatic, structural, and metamorphic development of the collision between the Arabian and Eurasian plates (Fig. 1). Included among the platform carbonates, nappes, and imbricated sedimentary sequences within this suture zone are granitoids and metamorphosed ophiolitic rocks that record subduction of Neotethyan oceanic crust into the middle Eocene (Fig. 2) (Robertson et al., 2007; Parlak et al., 2009; Karaoğlan et al., 2013). The Berit metaophiolite, which outcrops in the Berit and Doğanşehir areas of SE Anatolia, is

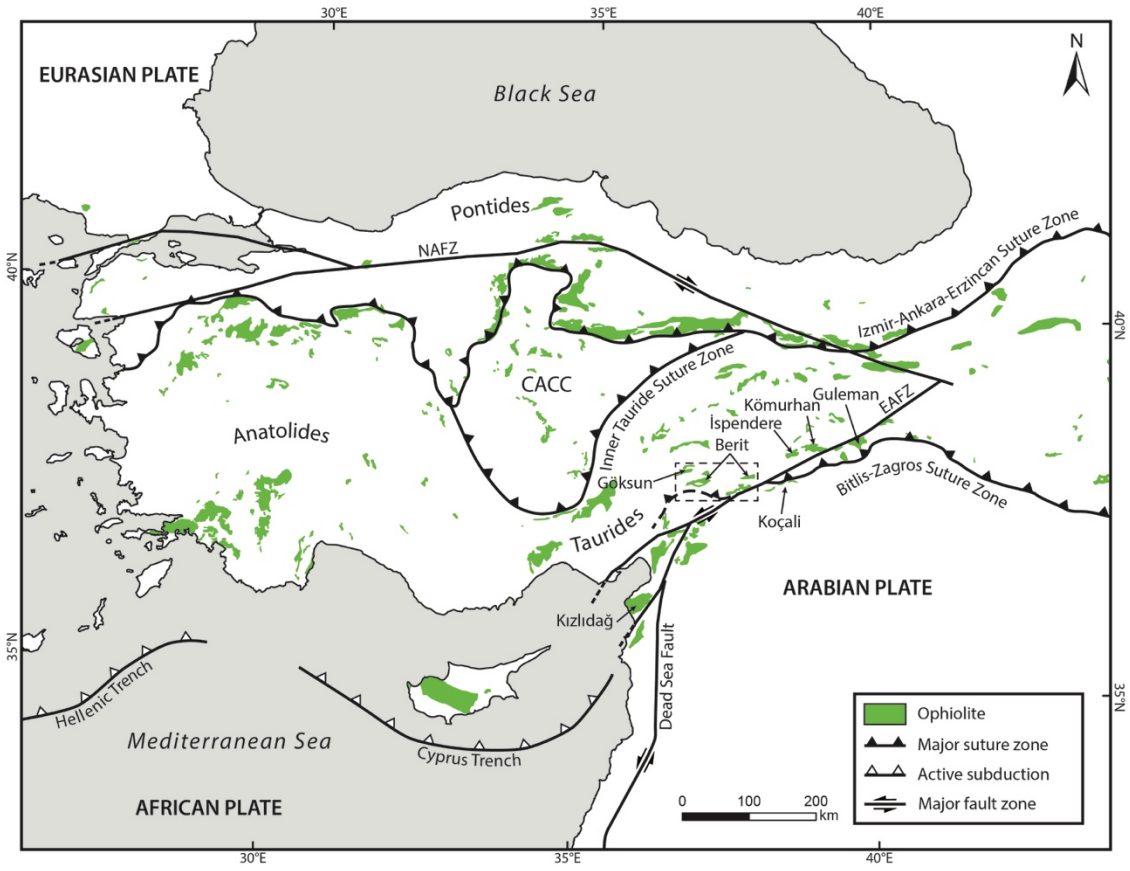

Figure 1. Simplified tectonic map of Turkey showing major sutures, fault zones, and rocks of ophiolitic origin (after Dilek and Flower, 2003). Dashed box indicates location of Fig. 2. Data from MTA (Directorate of Mineral Research and Exploration) 1:500,000 scale geological maps. NAFZ, North Anatolian Fault Zone; EAFZ, East Anatolian Fault Zone; CACC, Central Anatolian Crystalline Complex.

a tectonically dismembered ophiolite sequence correlated with other Late Cretaceous ophiolites in the Bitlis-Zagros suture zone (Figs. 1, 2, 3). These are thought to represent a single ophiolite sheet emplaced between the Late Cretaceous and middle Eocene (Genç et al., 1993; Robertson et al., 2006, 2007; Parlak et al., 2009; Karaoğlan et al., 2013).

Metagabbroic rocks within the Berit metaophiolite show evidence for metamorphism at amphibolite, granulite, and eclogite facies. Recent geothermobarometry of the granulite facies rocks suggests metamorphism at 690-941 °C and 1.3-1.7 GPa, corresponding with depths of 40-45 km (Karaoğlan et al., 2013). There is, however, considerable evidence for mineral disequilibrium textures within the granulites, such as

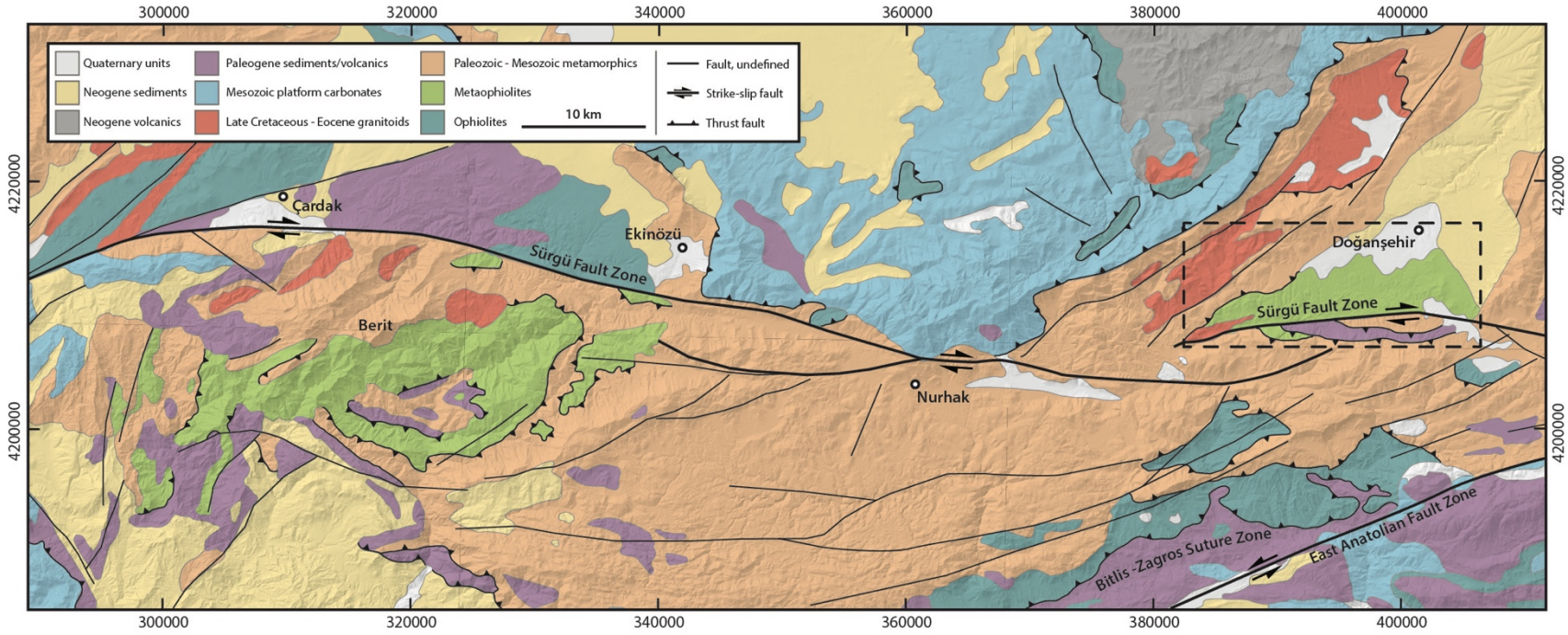

Figure 2. Simplified geologic map of the Berit-Doğanşehir region in SE Anatolia draped onto a Digital Elevation Model. Box indicates location of Fig. 3. After MTA (Directorate of Mineral Research and Exploration) 1:500,000 scale geological maps and Koç and Kaymakçi (2013).

symplectites and corona structures. While disequilibrium complicates conventional thermobarometry, these textures also offer a means of interpreting pressure-temperature (*P*-*T*) paths for the Berit metaophiolite. The aim of this study is to investigate the *P*-*T*-deformation evolution of the Berit metaophiolite using textural, geochemical, and structural data. Accurate interpretation of the petrogenesis of the Berit metaophiolite is crucial to understanding the origins of the metaophiolitic rocks and deciphering tectonic events during closure of the Southern Neotethys and collision between the Arabian and Eurasian plates.

Geologic Setting

The Anatolian microplate is a composite of multiple continental fragments and intervening oceanic units that coalesced in the Late Mesozoic and Cenozoic (Şengör and Yılmaz, 1981; Yılmaz, 1993; Robertson et al., 2007). Today, the sutures between these terranes are marked by thin and relatively continuous zones of ophiolitic rocks that were tectonically emplaced during collision of the continental fragments (Fig. 1). The Pontide and Tauride belts, separated by suture zones, represent two terranes that were sutured during the construction of Anatolia (Fig. 1). In southeastern Anatolia, the Bitlis-Zagros suture zone marks the former location of the southern branch of the Neotethys ocean and defines the zone of collision between the Taurides and the Arabian continent in the Oligo-Miocene (Jolivet and Faccenna, 2000; McQuarrie, 2003; Allen and Armstrong, 2008; McQuarrie and Van Hinsbergen, 2013). Northward subduction of the Neotethyan oceanic lithosphere was followed by collision between the Taurides and the Arabian continent, resulting in widespread deformation along this margin (Yılmaz et al., 1993;

Yılmaz, 1993). Continued northward movement of the Arabian plate relative to Anatolia contributed to the transition to westward tectonic escape that is mostly accommodated by the North and East Anatolian fault zones (Fig. 1) (Molnar and Tapponnier, 1975; Dewey et al., 1986; Le Pichon, 1995).

The Tauride belt in southern Anatolia consists of platform carbonates, ophiolites, metamorphic massifs, granitoids, and volcanic and sedimentary rocks with continental margin affinity (Fig. 2) (Yılmaz, 1993; Robertson et al., 2006, 2007; Parlak et al., 2012). These rocks are thought to represent a single microcontinent or collection of microcontinents that were rifted from the margin of Gondwana (Şengör and Yılmaz, 1981; Garfunkel and Derin, 1984; Garfunkel, 1998). Along the Bitlis-Zagros suture zone, the Tauride rocks are typically divided into three major tectonic units separated by thrusts: 1) Arabian platform carbonates, 2) a complex of nappes composed of accreted continental margin and oceanic units, and 3) imbricated sedimentary sequences (Genç et al., 1993; Yılmaz et al., 1993; Yılmaz, 1993; Robertson et al., 2006, 2007). The nappes consist of sedimentary cover, metamorphic massifs, and variably metamorphosed ophiolites, which are locally intruded by Late Cretaceous – Eocene granitoids (Fig. 2) (Perinçek and Kozlu, 1984; Yılmaz et al., 1993; Genç et al., 1993; Parlak, 2006; Karaoğlan et al., 2013). Post-collisional convergence between Eurasia and Arabia and onset of escape tectonics triggered strike-slip faulting and reactivation of thrusts (Şengör et al., 1985; Dewey et al., 1986; Kaymakçı et al., 2010; Koç and Kaymakçı, 2013).

The ophiolites of the Bitlis-Zagros suture zone in southeastern Anatolia occur in two belts. The peri-Arabic ophiolites (Kızıldağ and Koçali) were tectonically emplaced onto the Arabian platform, whereas the southeastern Anatolian ophiolites (Göksun, Berit,

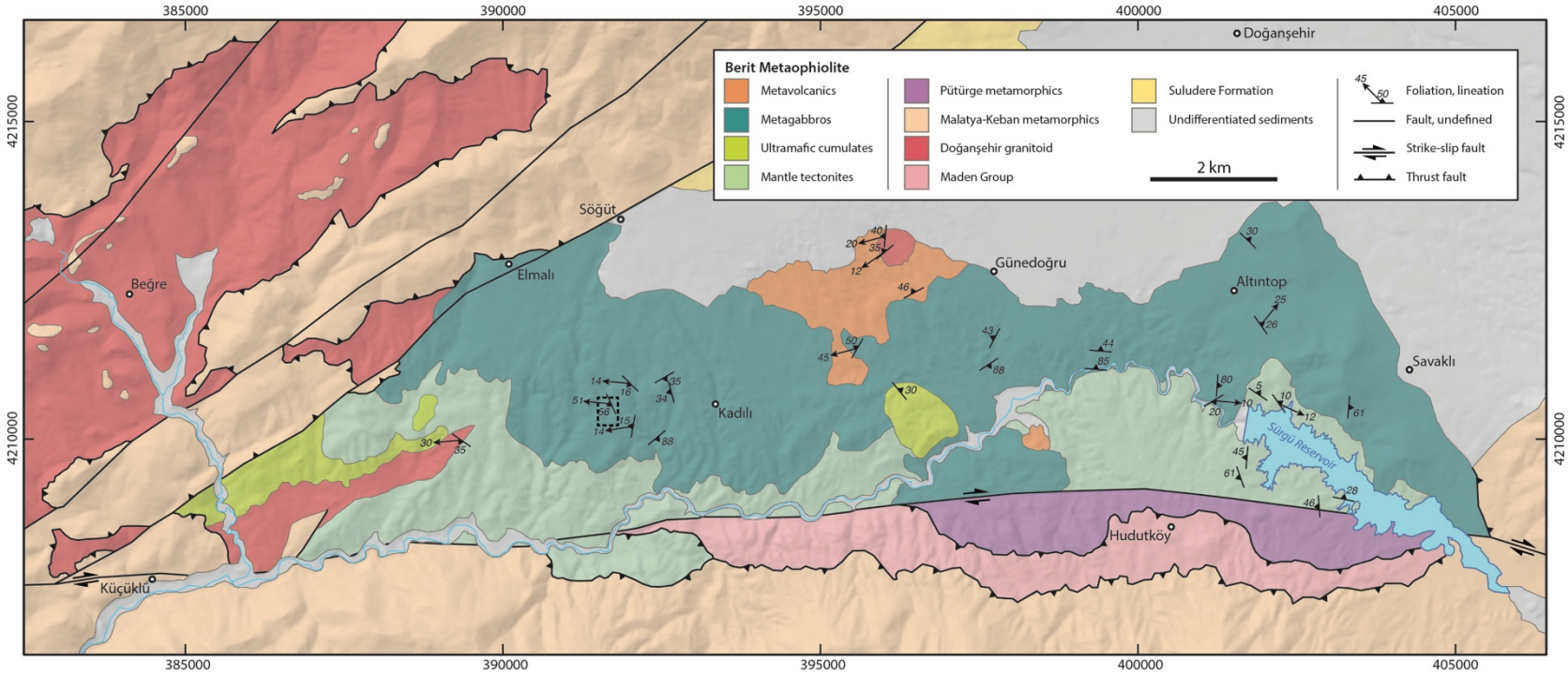

Figure 3. Geological map and representative structural data of the Doğanşehir region (modified from Karaoğlan et al., 2013) draped onto a Digital Elevation Model. Box indicates the location of Fig. 7.

Ispendere, Kömürhan, and Guleman) were emplaced onto the Tauride platform (Fig. 1) (Parlak et al., 2004). With the exception of Berit, these ophiolites are unmetamorphosed and exhibit complete but variably dismembered ophiolite pseudostratigraphy (Parlak et al., 2012). The geochemistry of these ophiolites suggests that they formed in a suprasubduction zone (SSZ) setting, likely in the Southern Neotethys (Parlak et al., 2004, 2009). A succession including evolved andesitic, volcaniclastic, and pelagic sedimentary rocks supports the existence of an associated volcanic arc (Robertson et al., 2006).

The Berit ophiolite contains one of the few exposures of metamorphosed ophiolitic rocks in the Southeast Anatolian orogenic belt. Variably metamorphosed ophiolitic rocks occur in the Berit and Doğanşehir regions to the north and south of the dextral Sürgü fault zone (Figs. 2, 3) (Perinçek and Kozlu, 1984; Yılmaz et al., 1993; Genç et al., 1993; Robertson et al., 2006; Karaoğlan et al., 2013). Numerous names have been applied to these rocks, including the Berit ophiolite, south Berit ophiolite, Berit Group, Berit metaophiolite, and Göksun metaophiolite. Here, the term 'Berit ophiolite' is chosen to refer to unmetamorphosed ophiolitic rocks in the Berit region and 'Berit metaophiolite' to refer to metamorphosed ophiolitic rocks in the Berit and Doğanşehir regions.

In the Berit region, high-pressure-high-temperature (H*P*-H*T*) metaophiolitic rocks occur within and at the base of the Berit ophiolite. These include granulite-eclogite, amphibolite, and epidote-amphibolite facies mafic rocks that have been interpreted as a metamorphic sole (Perinçek and Kozlu, 1984; Genç et al., 1993; Robertson et al., 2006). The metaophiolitic rocks also show evidence of H*T* ductile deformation (folds, mylonites) related to accretion to the Tauride margin and continued subduction

(Robertson, 2006). Similar metaophiolitic rocks of amphibolite to granulite facies are exposed ~60 km east of Berit in the Doğanşehir region, north of the dextral Sürgü fault (Figs. 2, 3).

The H*P*-H*T* metaophiolitic rocks in the Berit region are tectonically interleaved with unmetamorphosed ophiolite and are in turn folded into a large, recumbent, south-verging anticline (Genç et al., 1993). The unmetamorphosed ophiolitic rocks contain an intact section of layered ultramafic rocks and mafic cumulates, as well as gabbro, plagiogranite, and basaltic dikes. Geochemistry of the Berit ophiolite indicates formation in a SSZ setting, similar to other southeastern Anatolian ophiolites (Parlak et al., 2004; Robertson et al., 2006).

The Berit ophiolite is unconformably overlain by the Maden Group, a middle Eocene volcanic and sedimentary sequence attributed to a short-lived back-arc basin (Genç et al., 1993; Yiğitbaş and Yılmaz, 1996; Robertson et al., 2006). The Berit ophiolite is thrust over the Maden Group, and in turn overthrust by the low-grade Late Paleozoic – Early Mesozoic platform carbonates of the Malatya-Keban Metamorphic unit (Perinçek and Kozlu, 1984; Genç et al., 1993; Yılmaz et al., 1993; Robertson et al., 2006).

The Berit metaophiolite in Doğanşehir

As is the case with the unmetamorphosed Berit ophiolite, metaophiolitic rocks in the Doğanşehir region are overthrust by the Malatya-Keban metamorphic unit (Figs. 2, 3, 4). The metaophiolitic rocks and Malatya-Keban metamorphic unit are intruded by the 54-45 Ma Doğanşehir granitoid (Karaoğlan et al., 2013; Karaoğlan et al., 2016). South of

the Sürgü fault, rocks correlated with the Pütürge metamorphic unit are overlain by Maden Group sedimentary units and overthrust by Malatya-Keban metamorphic rocks (Perinçek and Kozlu, 1984; Yılmaz et al., 1993; Parlak et al., 2004; Robertson et al., 2006, 2007; Parlak et al., 2009; Karaoğlan et al., 2013).

Metaophiolitic lithologies in Doğanşehir include metamorphosed mantle tectonite, ultramafic cumulate, metagabbro, and metavolcanic rocks and therefore display an

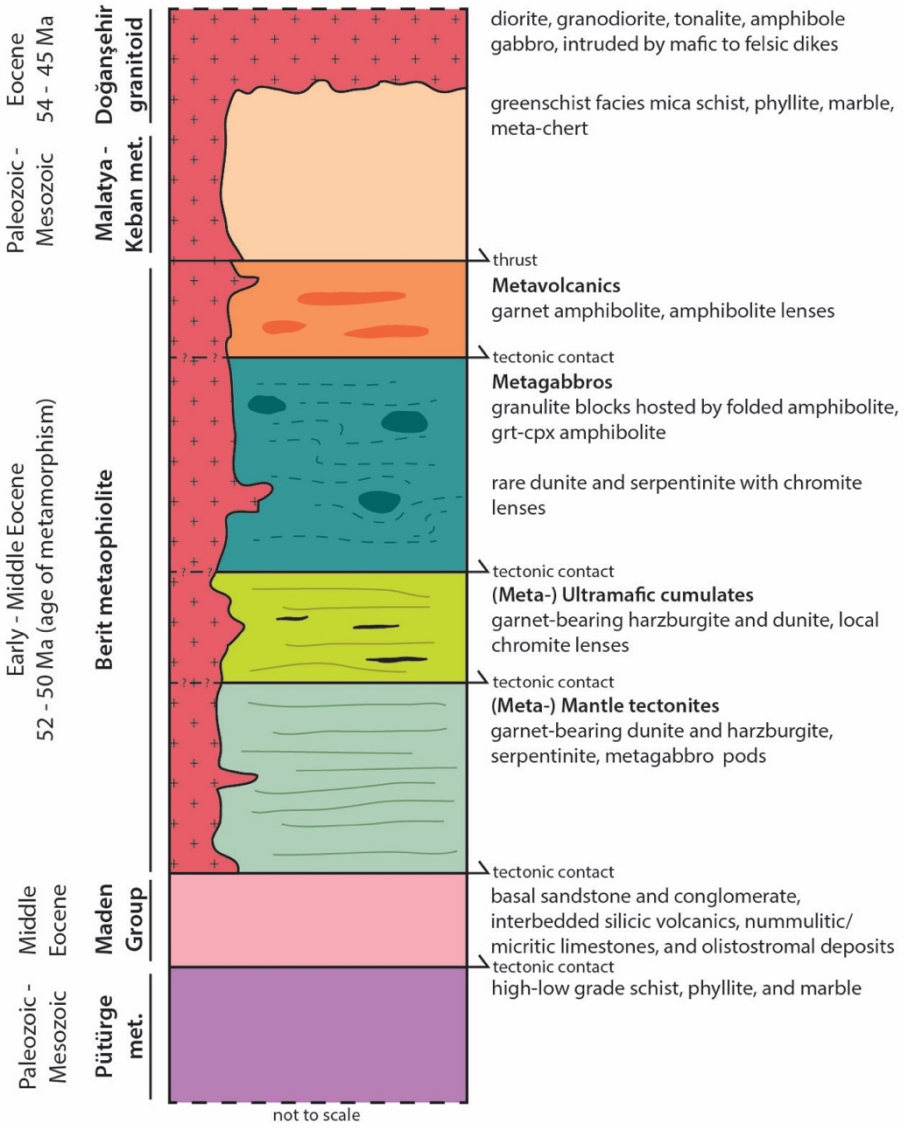

Figure 4. Schematic tectonostratigraphic column of the Berit metaophiolite and related units in the Doğanşehir region after Karaoğlan et al. (2013).

approximate ophiolite pseudostratigraphy (Perinçek and Kozlu, 1984; Genç et al., 1993; Yılmaz et al., 1993; Robertson et al., 2006, 2007; Parlak et al., 2009; Karaoğlan et al., 2013) (Figs. 3, 4). The nature of the contacts between the units is unclear, although they have been interpreted as late extensional faults based on the presence of asymmetrical folds, normal faults, and C-S structures (Karaoğlan et al., 2013). The metamorphosed mantle tectonites and ultramafic cumulates consist of garnet-bearing harzburgite, dunite, and serpentinite as well as rare metagabbro. Metamorphosed ultramafic cumulates locally contain podiform chromite. The metagabbro contains a diverse suite of rock types that includes amphibolite (± corundum), garnet-clinopyroxene amphibolite, and pods of granulite hosted by amphibolite. Serpentinite and chromite-bearing dunite also occur locally within the metagabbro (Genç et al., 1993; Yılmaz et al., 1993; Parlak et al., 2009). The metavolcanic rocks are garnet amphibolites that locally contain lenses of amphibolite lacking garnet.

Recent garnet-clinopyroxene geothermobarometry suggests that the granulite pods experienced peak metamorphism at pressures of 1.3-1.5 GPa and temperatures in excess of 900 °C (Karaoğlan et al., 2013). A Sm-Nd age for a kyanite granulite, based on a clinopyroxene-garnet-whole rock isochron, yielded 50.6 ± 3.2 Ma, which is interpreted as a cooling age (Karaoğlan et al., 2013). The authors attributed the granulite facies conditions to metamorphism within the root of a Neotethyan island arc, where the source of additional heat was provided by subduction of an inferred ridge. Granulite-hosting amphibolites, amphibole rims on garnet and clinopyroxene in the granulites, and clinopyroxene-plagioclase-kyanite symplectites were taken as evidence for isothermal

decompression and exhumation of the metaophiolitic rocks during extension and basin formation (Karaoğlan et al., 2013).

Field relations and petrography

The metabasalt, metagabbro, ultramafic cumulate, and mantle tectonite units of the Berit metaophiolite outcrop in a tectonic window ~10 km south of the town of Doğanşehir (Figs. 2, 3). The ophiolitic pseudostratigraphy is generally northward dipping. Metavolcanic rocks outcrop in the north of the tectonic window, whereas the metagabbro, ultramafic cumulate, and mantle tectonite units occupy more southerly positions. Contacts between the metaophiolitic units are mostly obscured. To the north, low-grade marble and schist of the Malatya-Keban metamorphic unit are thrust over the Berit metaophiolite. Both the Malatya-Keban metamorphic rocks and Berit metaophiolite are intruded by the Doğanşehir granitoid (Fig. 2). The Berit metaophiolite is truncated in the south by the dextral Sürgü Fault, which juxtaposes the metaophiolite with Pütürge marble and schist as well as Maden Group sedimentary rocks (Fig. 2).

The rocks of the Berit metaophiolite – particularly the metagabbroic rocks – have a foliation defined by modal variation in mineralogy as well as alignment of platy minerals. A lineation defined by aligned amphibole is common in the metagabbroic amphibolites. There is considerable field evidence for folding that likely disrupts the northward tectonostratigraphy of the metaophiolitic units. Folds occur on scales of centimeters to meters, and fold geometries are typically open to close and southward-verging. Minor folds measured in the field have roughly east-west trending fold hinges and a slight plunge to the west (Fig. 5). These are parallel to fold hinges calculated from

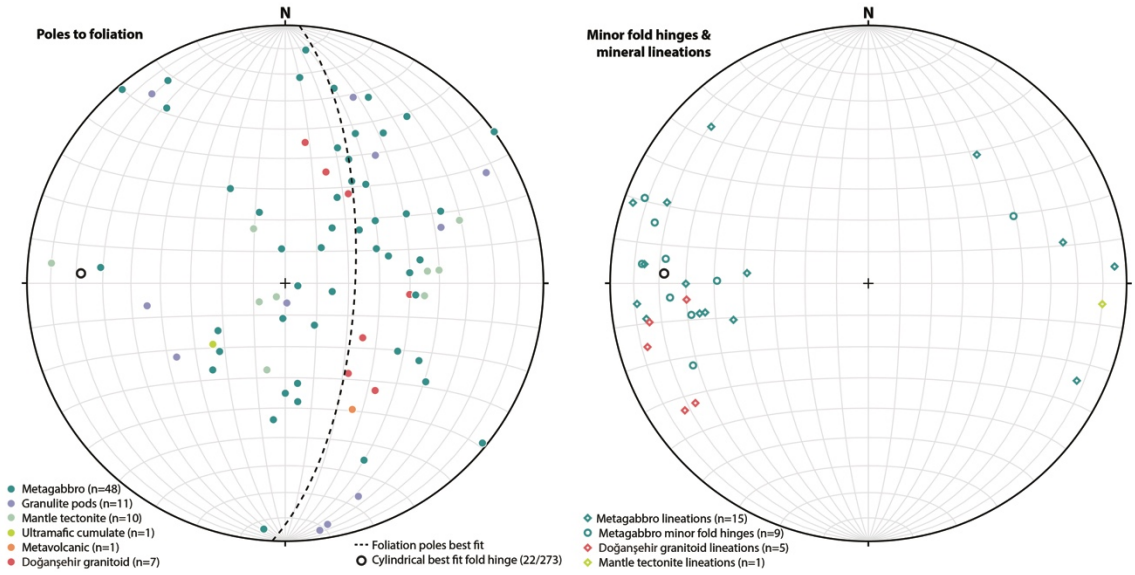

Figure 5. Equal area, lower hemisphere stereonets showing structural data from the Doğanşehir region. The fold hinge calculated from poles to foliation is similar to minor fold hinges measured in the field. Mineral lineations are sub-parallel with fold hinges.

poles to foliation of the metaophiolitic units (Fig. 5). Lineations also have an east-west trend and a shallow plunge. C-S fabrics and shear zones at centimeter and meter scales are also observed, although they are not commonly seen *in situ*. Therefore, a systematic and regional kinematic analysis is not possible.

Felsic and intermediate plutonic rocks of the Doğanşehir granitoid intrude the metaophiolitic rocks in the northern and western regions of the field area (Figs. 2, 3). Meter-scale felsic dikes and pegmatites have intrusive relations to the metagabbro, metabasalt, and mantle tectonite units (Fig. 3, 4). Some granitoid rocks display a foliation and lineation defined by biotite and magnetite. Small protomylonitic shear zones and C-S fabrics are also observed near the boundaries of the intrusive bodies.

The units of the Berit metaophiolite also contain significant internal lithological variation. The metagabbro unit includes serpentinite, lenses of chromite-rich peridotite, amphibolite, garnet-clinopyroxene amphibolite, and granulite. With the exception of the

granulite, these lithologies are mappable over tens of meters to kilometers, and do not appear to be a mélange. Granulite facies metagabbroic rocks occur as podiform bodies within the amphibolite facies rocks of the metagabbro unit.

Mafic pods

Granulite and amphibolite pods are distributed across the east-west extent of the field area, although the majority occur in three clusters west of Kadılı and another cluster west of Savaklı (Fig. 3). Three different granulite pod lithologies are observed in the field. Kyanite granulites are observed west of Kadılı (Fig. 3). Garnet-clinopyroxene granulites occur west of Kadılı (with kyanite granulite pods) and just north of the Sürgü reservoir. Samples of the garnet-clinopyroxene granulite from both regions appear to have similar fabrics, mineral modes, and textures. Corona granulites are only observed in a small cluster west of Savaklı. The pods typically occur as meter-scale ellipsoids hosted by folded amphibolite (Figs. 6, 7). Most pods are weathered out of the host amphibolite, although some can be observed in outcrop with the contact between pod and host preserved (Fig. 6). In outcrops where the contact is intact, the foliation of the matrix amphibolite is observed to wrap around the pods. Along particularly well-preserved contacts, the pod fabric is sheared into the host amphibolite foliation, and increasing amphibolitization of the granulite assemblage from core to rim is typical (Fig. 6). Long axes of pods are commonly parallel to the strike of the host amphibolite foliation.

Pods of amphibolite also occur in close proximity to the granulite-facies pods (Fig. 7). Like the granulite pods, amphibolite pods are distinctive from the host rocks because they weather out of the host rocks. They also appear finer grained and more

massive than their host counterparts. It is noted, however, that some amphibolite pods may represent rinds on an otherwise obscured granulite-facies pod.

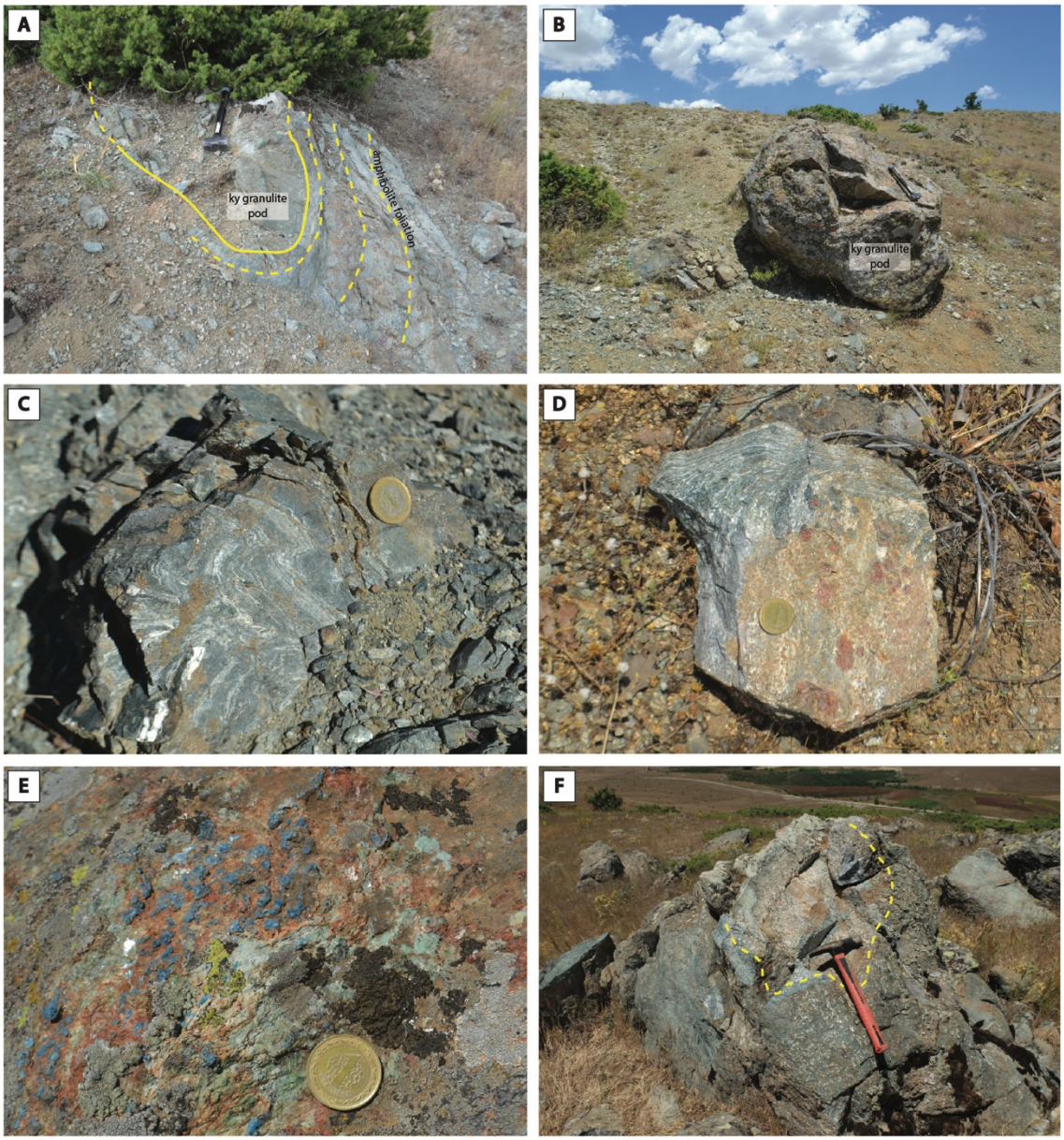

Figure 6. Field photographs of granulite pods and host amphibolites. A) Granulite pod wrapped by foliated amphibolite. B) Large granulite pod weathered out of host amphibolite. C) Small folds in amphibolite. D) Sample of a granulite pod with coarse-grained garnet showing progressive growth of amphibole rims towards the amphibolite host rind. E) Coarse-grained kyanite in a granulite pod. F) Corona granulite pod with amphibolite rind.

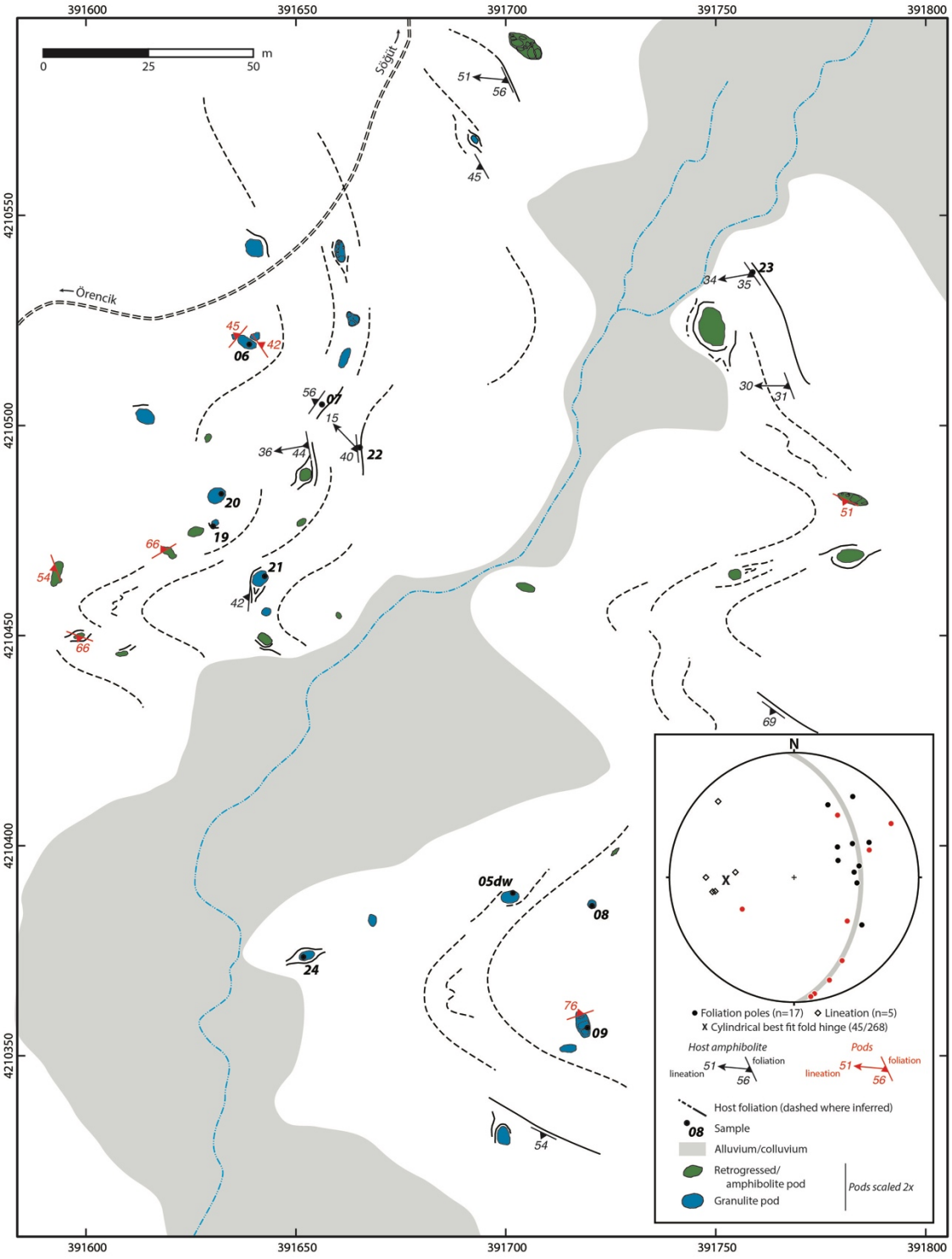

Figure 7. Map of granulite pods west of Kadılı. Host foliation is inferred from field observations and structural measurements shown in the inset stereonet. The local deformation mimics that of the regional structure shown in Fig. 5. All samples have the prefix CAT15.

Sample descriptions

Ninety-four representative samples of the Berit metaophiolite were collected from the Doğanşehir region and sixty-five were prepared as thin sections (Appendix 1). Modal abundances of phases in three samples are given in Table 1 (grain size descriptions as follows: fine-grained < 0.5 mm; medium-grained = 0.5–1 mm; and coarse-grained > 1 mm; mineral abbreviations after Whitney and Evans, 2010). Analytical methods are given in Appendix 2. Mineral compositional data are given in Appendix 3.

Corona granulite

Corona granulites contain garnet + clinopyroxene + plagioclase + orthopyroxene and minor sapphirine, corundum, rutile, and spinel. Corona granulites also contain secondary amphibole and chlorite. The corona granulites are characterized by orthopyroxene surrounded by coronas of clinopyroxene and garnet in a matrix of plagioclase (Figs. 8-11; Table 1). Orthopyroxene (En_{92}) occurs as aggregates of fine-grained granoblastic polygonal grains surrounded by a corona of clinopyroxene (Fig. 9a). In some cases, a thin rim of amphibole occurs between the inner orthopyroxene aggregate and clinopyroxene corona (Fig. 9a). Coronitic clinopyroxene displays similar granoblastic textures and fine to medium grain size. The clinopyroxene is diopside ($Jd_{04-07}Ae_{01}Q_{92-95}$) and is zoned with slightly higher jadeite contents (Jd_{07}) at the outer rim of

Table 1. Mineral modes for representative granulite samples

Sample	Lithology	Amp	Cpx	Crn	Grt	Ky	Opx	Pl	Rt	Spr
CAT15-02	Corona granulite	5	34	sympl	26		4	31	tr	i
CAT15-09A	Grt-Cpx granulite	10	38	tr	39	6	tr	7	tr	i
CAT15-24	Kyanite granulite	5	59	tr	24	12			tr	

tr - trace; i - as inclusions; sympl - in symplectite

the corona (Appendix 3). The clinopyroxene is surrounded by a corona of garnet, and the two coronas are locally separated by a rim of pargasite or magnesio-hornblende (Fig. 9a). In some cases, garnet appears intergrown with clinopyroxene.

Garnet coronas (~0.5 mm thick) contain fine-grained inclusions of sapphirine (Fig. 10a). Garnet is gradually zoned from a higher Mg/lower Ca inner rim ($Prp_{68-74}Alm_{14-15}Grs_{15-19}Sps_{0-01}$) to a lower Mg/higher Ca outer rim ($Prp_{60-66}Alm_{13-17}Grs_{21-22}Sps_{0-01}$). Sapphirine inclusions occur across the garnet zoning (Fig. 10a). The garnet corona is surrounded by a symplectic intergrowth of lamellar corundum in clinopyroxene ($Jd_{03-09}Ae_{0-01}Q_{91-96}$). The clinopyroxene-corundum symplectite is not present in all coronas, even within individual samples.

Matrix plagioclase is anhedral and fine- to coarse-grained. Plagioclase is anorthite rich (An_{90}) and shows a slight increase in albite content (An_{85}) towards the rim. Coarse plagioclase grains contain numerous fine-grained inclusions of clinopyroxene.

Clinopyroxene also occurs in the matrix as coarse, anhedral grains. Matrix diopside ($Jd_{01-04}Ae_{01-04}Q_{94-95}$) shows similar minor increases in jadeite towards the rim. Matrix and symplectite clinopyroxene are partially replaced by pargasite and magnesio-hornblende (Mg# = 0.96-1.00) (Fig. 10a). In pod rim samples, the corona texture is almost completely erased by amphibole replacing garnet and clinopyroxene.

Garnet-clinopyroxene granulite

The garnet-clinopyroxene granulites contain an assemblage of garnet + clinopyroxene + plagioclase + kyanite ± orthopyroxene, as well as accessory corundum, sapphirine, rutile, and secondary pargasite, zoisite, and chlorite (Figs. 8-11; Table 1). The

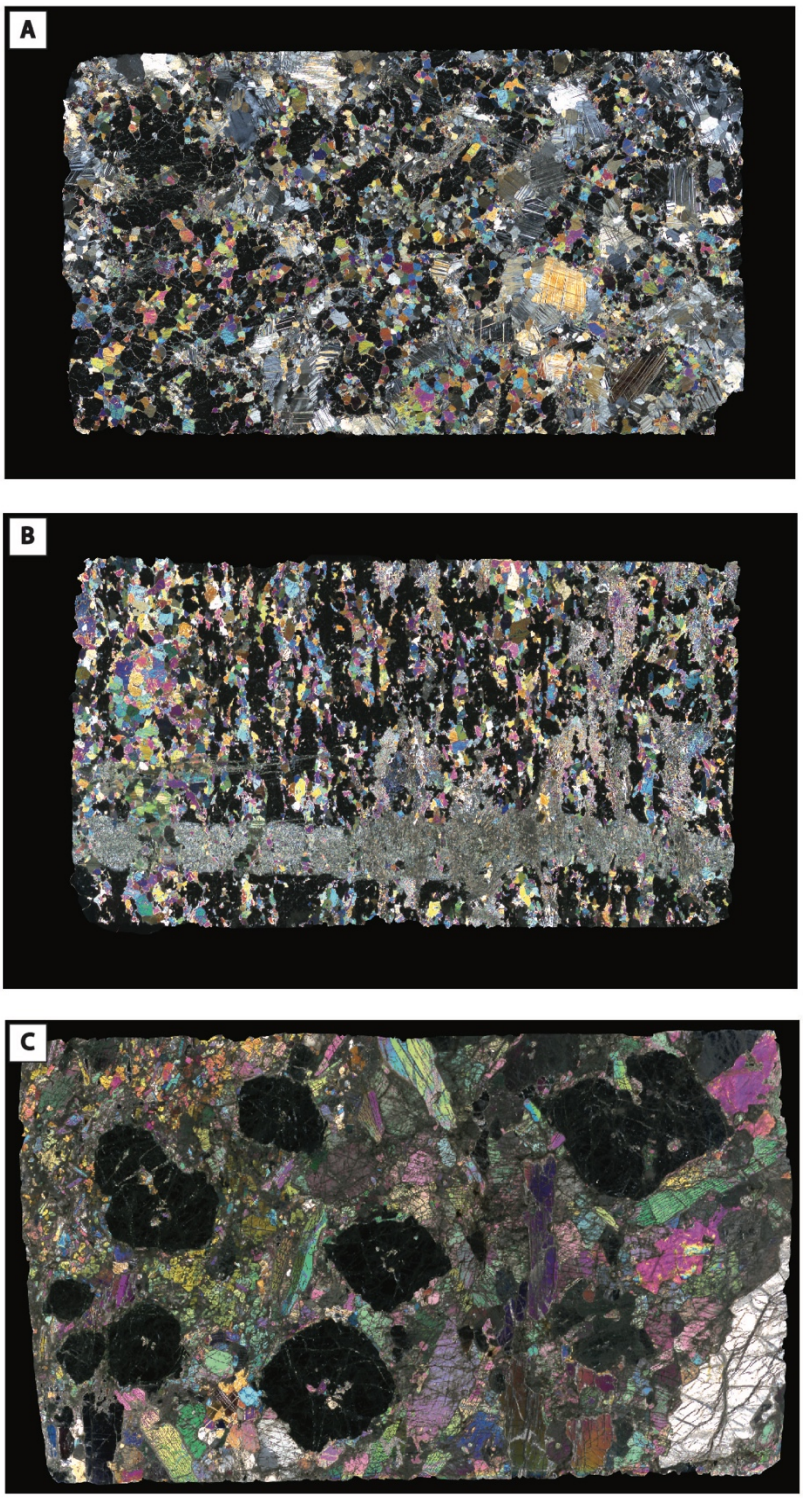

Figure 8. Thin section scans of representative granulite textures under crossed polarized light. All images 26 mm x 46 mm. A) Corona granulite (CAT15-02) showing coarse-grained plagioclase and Grt+Cpx coronas on orthopyroxene. B) Garnet-clinopyroxene granulite (CAT15-09A) with vein of chlorite. A large shape-preferred aggregate of polygonal clinopyroxene is visible on the left side of the thin section. Mottled regions towards the right side of the section are Cpx+Ky symplectites. C) Kyanite granulite (25613O) showing very coarse-grained garnet porphyroblasts and kyanite laths. Garnets contains inclusions of clinopyroxene.

garnet-clinopyroxene granulite pods have a moderate to well-defined foliation and lineation. The foliation is defined by mm to cm-scale modal variation of garnet and clinopyroxene. The lineation is formed by shape-preferred orientation of clinopyroxene aggregates.

Garnet occurs in ~0.5 mm clusters of subhedral to anhedral grains (Fig. 9c). In some samples, garnet contains fine-grained inclusions of sapphirine. Although garnet displays a range of compositions between samples, it typically has Mg-rich cores ($Prp_{60-73}Alm_{12-18}Grs_{14-25}Sps_{0-01}$) and increasing Ca and Fe^{2+} content within ~50 μm of the rim ($Prp_{51-67}Alm_{14-21}Grs_{19-30}Sps_{0-01}$) (Appendix 3). Clinopyroxene occurs as a matrix phase and as oriented aggregates of fine to medium granoblastic grains (Fig. 9c). In samples with less well-developed planar fabrics, clinopyroxene aggregates are surrounded by garnet coronas that resemble those of the corona granulites. Matrix and aggregate clinopyroxene is diopside and is typically unzoned, although can have slightly higher rim jadeite values ($Jd_{04-13}Ae_{0-01}Q_{89-95}$). Clinopyroxene also occurs in fine-grained symplectic intergrowths with kyanite (Figs. 9c-d, 10b).

Kyanite-clinopyroxene symplectites are adjacent to garnet and plagioclase, and typically separate the two phases (Fig. 9c). Garnet boundaries with symplectite are mottled and irregular. Clinopyroxene in the symplectites has higher jadeite content than matrix clinopyroxene and approaches omphacite in composition ($Jd_{13-18}Ae_{0-01}Q_{81-87}$). Rare corundum and plagioclase also occur in the symplectites, although the plagioclase commonly appears to be a partially replaced ‘core’ completely surrounded by symplectite (Fig. 9c).

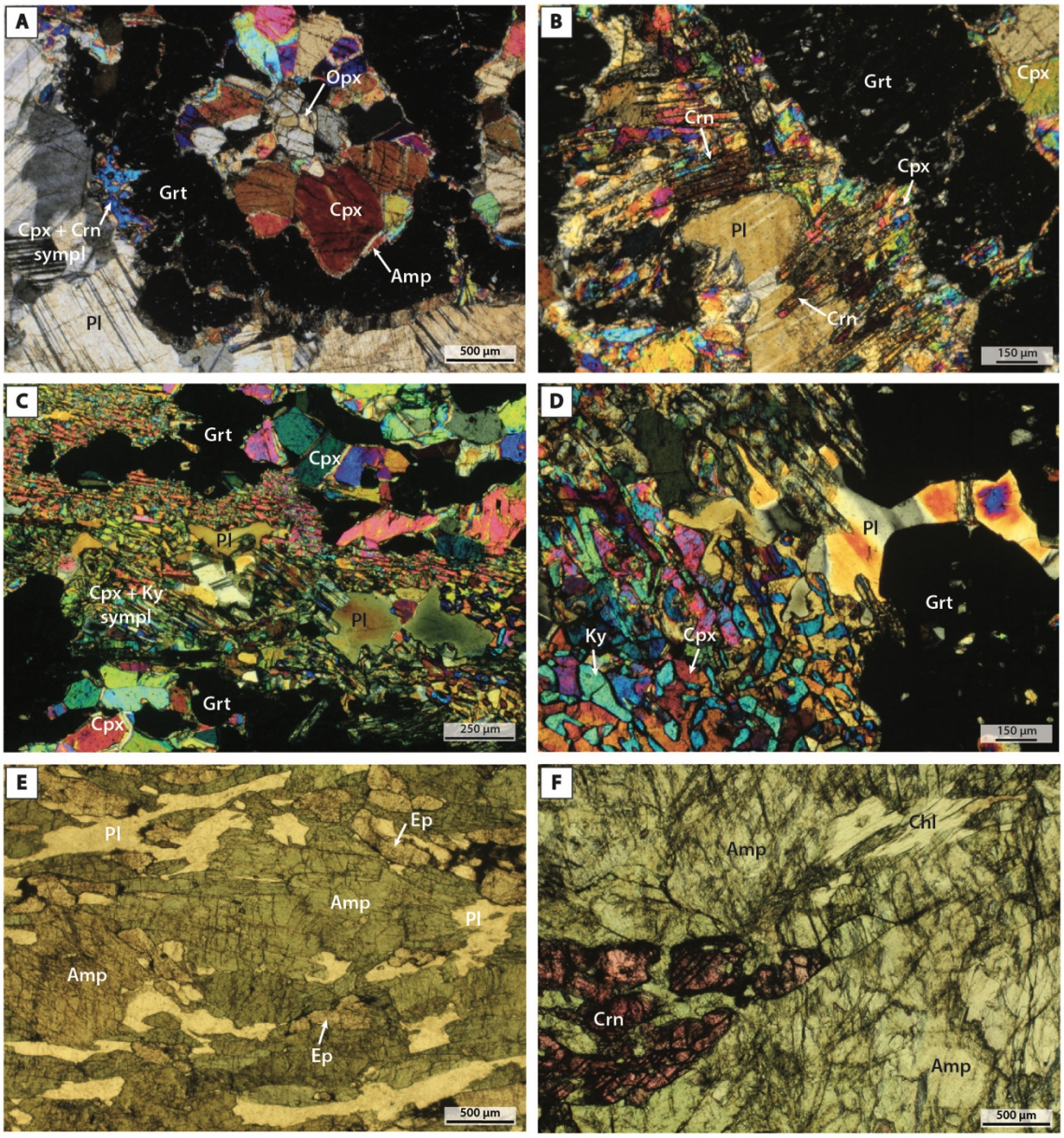

Figure 9. Photomicrographs of representative textures in the Berit granulites and amphibolites. A) Photomicrograph of corona granulite (CAT15-02) with cores of orthopyroxene and coronas of clinopyroxene and garnet in plagioclase matrix (crossed polars). A thin rim of Crn-Cpx symplectite surrounds portions of the garnet corona. B) Crn-Cpx symplectite surrounding a garnet corona in sample CAT15-02 (crossed polars). C) Anhedral plagioclase surrounded by Ky-Cpx symplectite in sample CAT15-09A (crossed polars). D) Ky-Cpx symplectite adjacent to plagioclase and garnet in sample CAT15-09A (crossed polars). E) Amphibolite host (CAT15-23) showing coarse grained amphibole, plagioclase, and epidote (plane light). F) Corundum-bearing amphibolite (CAT15-01dw). Amphibole adjacent to corundum has deeper green pleochroism than amphibole at a greater distance from corundum.

Plagioclase cores are anorthite rich (An_{56-77}) and increase in albite content to the rim (An_{32-49}) (Fig. 10b). Orthopyroxene (En_{92}) occurs as foliation-parallel, fine-grained

clusters. Pargasite and magnesio-hornblende (Mg# = 0.91-0.98) occur as anhedral grains and are observed replacing matrix and aggregate clinopyroxene.

Kyanite granulite

The most common pod lithology contains clinopyroxene + garnet + kyanite ± plagioclase (Figs. 8, 11; Table 1). Accessory phases include corundum and rutile. Magnesio-hornblende, zoisite, and chlorite appear secondary. Kyanite granulite pods are primarily massive but in some cases display foliation defined by cm-scale variation in modal amounts of clinopyroxene, plagioclase, and garnet. Fine to coarse-grained clinopyroxene displays granoblastic and decussate textures. Matrix clinopyroxene is diopside ($Jd_{04\text{-}12}Ae_{0\text{-}03}Q_{87\text{-}93}$) and is typically unzoned.

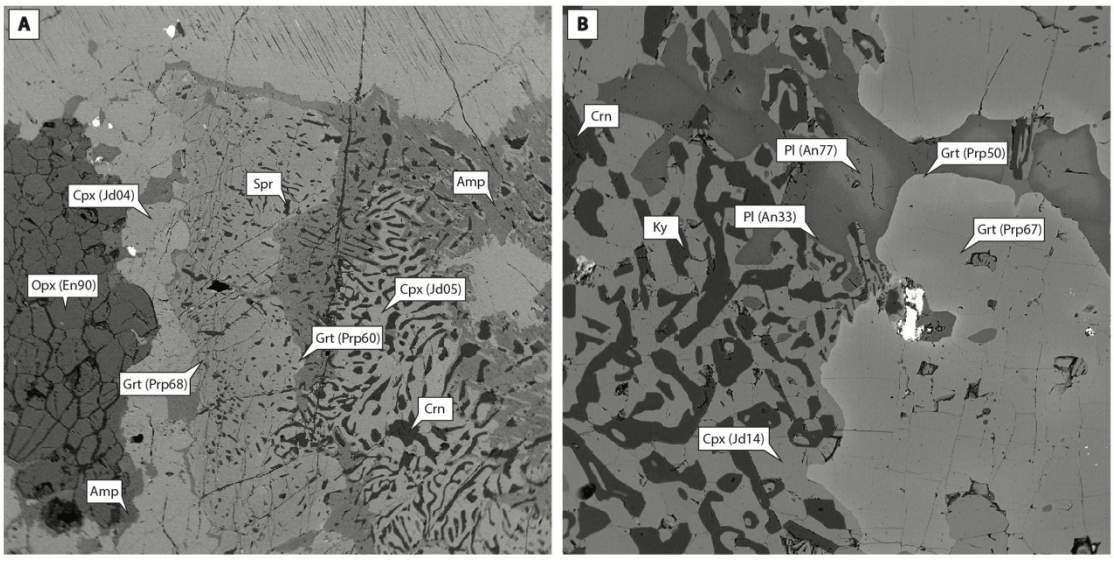

Figure 10. Back-scatter electron images of representative granulite textures annotated with mineral compositions. A) Corona granulite sample CAT13-27C1. Coronas of clinopyroxene and garnet on orthopyroxene. Garnet contains numerous inclusions of sapphirine. The coarse grained Crn-Cpx symplectite is partially replaced by amphibole. B) Grt-Cpx granulite sample CAT15-09A. Ky-Cpx symplectite adjacent to garnet and plagioclase. Garnet and plagioclase have irregular grain boundaries in contact with symplectite. Same view as Fig. 9d.

Garnet occurs as euhedral to subhedral porphyroblasts that exhibit a large range of grain sizes (~0.5 mm to 3 cm). Garnet is commonly inclusion-free, although coarse grains contain inclusions of clinopyroxene ($Jd_{08}Ae_{03}Q_{88}$) and kyanite (Fig. 8c). Garnet is relatively homogeneous but displays some variability between samples ($Prp_{50-64}Alm_{16-28}Grs_{18-27}Sps_{0-01}$).

Kyanite appears as two texturally distinct varieties. Matrix kyanite occurs as medium to coarse-grained subhedral laths (Fig. 8c). Kyanite also appears as rare fine-grained intergrowths with clinopyroxene in some samples. These kyanite-clinopyroxene symplectites are globular and are typically adjacent to garnet and plagioclase. Clinopyroxene in the symplectites is more sodic ($Jd_{12-16}Ae_{0-01}Q_{84-88}$) than matrix clinopyroxene ($Jd_{04-12}Ae_{0-03}Q_{87-93}$).

Plagioclase occurs as anhedral fine- to medium-grained crystals and appears slightly zoned with increasing albite content to the rim (An_{36-30}). Magnesio-hornblende (Mg# = 0.94-0.98) forms rims on garnet and is observed replacing clinopyroxene. The margins of kyanite granulite pods display higher degrees of amphibolitization than pod core assemblages. Zoisite is present in more amphibole-rich samples as fine subhedral grains or coarse, in some cases poikiloblastic grains with inclusions of amphibole and clinopyroxene.

Amphibolite

Amphibolites that host the granulite pods contain magnesio-hornblende + epidote ± corundum ± plagioclase ± quartz as well as minor amounts of zoisite, rutile, titanite, and chlorite (Figs. 9, 11). Pod rim amphibolite samples that appear transitional between

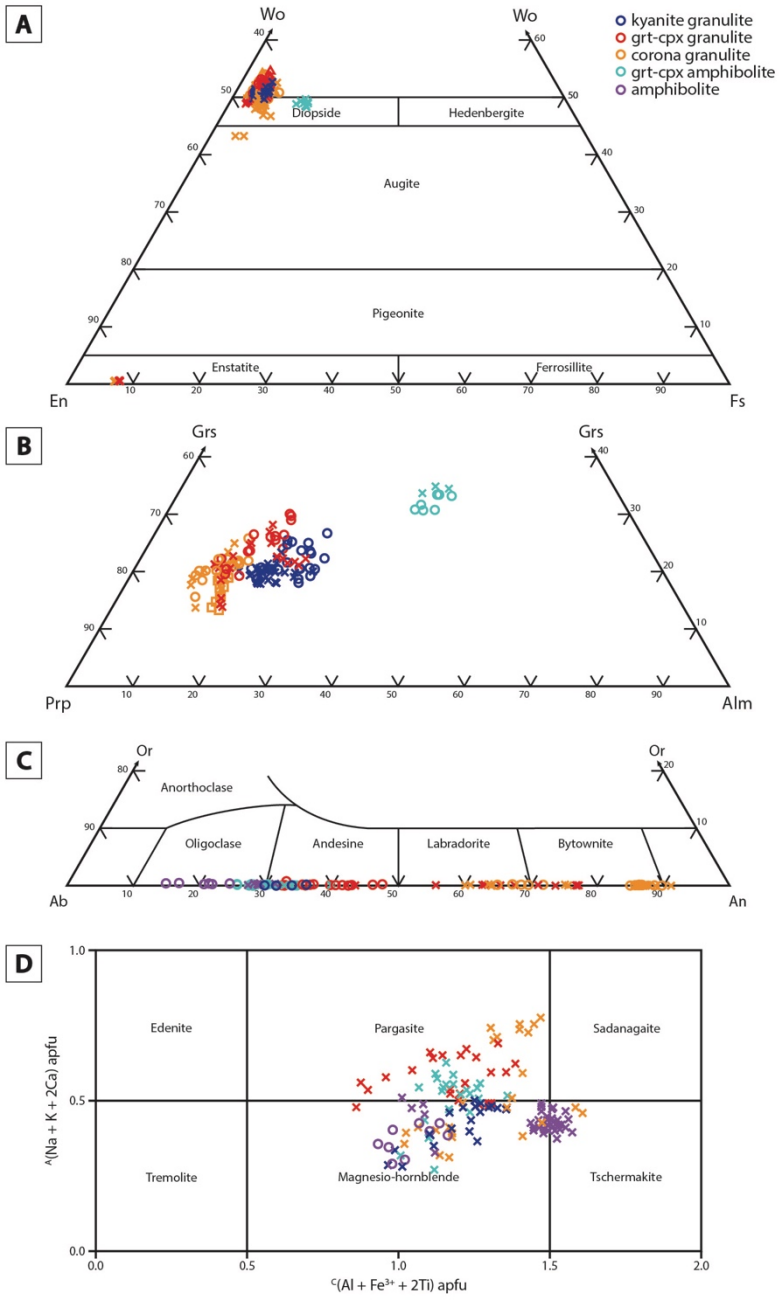

Figure 11. Mineral composition plots of clinopyroxene, garnet, feldspar, and amphibole; ×, cores; ○, rims. Cpx and Opx from the granulites cluster, while Cpx from the Grt-Cpx amphibolites have slightly different composition. B) Garnet cores from granulites are more pyrope-rich than rims. Garnet in the Grt-Cpx amphibolites are more almandine and grossular-rich. C) Plagioclase in corona granulites have the highest An content, reaching An_{90}. Rims in all samples are typically more albite-rich than cores. D) Amphiboles are pargasite, magnesio-hornblende, and tschermakite. Amphiboles from a corundum-bearing amphibolite cluster at the edge of the tschermakite field.

granulite assemblages and the amphibolite host also contain relict garnet and clinopyroxene. The amphibolite foliation is defined by variation in modal amphibole,

plagioclase, and epidote. The long axes of amphibole and epidote grains define a lineation. Nematoblastic amphibole is fine to coarse-grained and contains inclusions of plagioclase and epidote (Fig. 9e). Amphibole composition is variable between samples, but is typically magnesio-hornblende and tschermakite. Some amphiboles show core to rim zoning with magnesio-hornblende cores (Mg# = 0.75-0.80) and magnesio-ferri-hornblende rims (Mg# = 0.81-0.89).

Epidote occurs as fine- to coarse-grained subhedral and anhedral grains (Fig. 9e). Plagioclase forms fine to medium subhedral grains that display increasing albite content from core (An_{27-31}) to rim (An_{15-24}). Corundum is subhedral and ranges from medium to coarse grained (Fig. 9f). In some cases, individual corundum grains reach up to 5 cm. Corundum is also notable for its pink color in hand sample and thin section, owing to its high Cr_2O_3 content (up to 2 wt%) (Fig. 9f). Amphibole adjacent to corundum displays deep green pleochroism and high Cr_2O_3 content (up to 1 wt%) that decreases with distance from the corundum.

Garnet-clinopyroxene amphibolite

Unlike the pod-hosting amphibolites, the garnet-clinopyroxene amphibolites are not observed to host pods and occur as a coherent body (~1 km^2) within the metagabbro unit northwest of the Sürgü reservoir (Fig. 3). The garnet-clinopyroxene amphibolites consist of garnet + pargasite + clinopyroxene + plagioclase + epidote, along with minor amounts of rutile, chlorite, titanite, quartz, and corundum (Fig. 11). Matrix amphibole and modal variation in garnet, amphibole, and plagioclase define the layering and foliation. Garnet forms subhedral to euhedral medium and coarse-grained porphyroblasts

that contain inclusions of pyroxene, quartz, and epidote. Garnet is fairly homogeneous ($Prp_{25-31}Alm_{37-42}Grs_{31-34}Sps_{01-04}$). Magnesio-hornblende and pargasitic amphibole (Mg# = 0.68-0.83) form anhedral and poikiloblastic crystals and also occur as rims on garnet and clinopyroxene. Fine to medium-grained plagioclase displays granoblastic textures and is slightly zoned from core to rim (An_{40-26}). Diopside clinopyroxene occurs as unzoned ($Jd_{07-11}Ae_{03-05}Q_{86-89}$) fine to coarse anhedral grains. The compositions of garnet and clinopyroxene in these rocks are distinct from the granulite facies garnet and clinopyroxene. Garnet in the granulites is more Mg-rich than that of the garnet-clinopyroxene amphibolites and contains less Fe and Ca (Fig. 11a). Clinopyroxene in the granulites also contains lower Fe (Fig. 11b).

Garnet amphibolite

Samples of garnet amphibolite from the metavolcanic unit contain garnet + amphibole ± epidote ± plagioclase ± quartz and minor rutile. Coarse-grained garnet porphyroblasts are subhedral to anhedral and contain numerous inclusions of rutile. Amphibole is medium to coarse grained and in some cases displays poikiloblastic textures. Epidote occurs as fine to coarse-grained subhedral masses. Rare plagioclase is fine grained and anhedral. Analyses of garnet amphibolite mineral compositions were not obtained.

Geochemistry

Twenty-two representative samples from the Berit metaophiolite in the Doğanşehir region were selected for whole-rock major-element analysis. A subset of

fifteen samples was analyzed for whole-rock trace-element geochemistry (Table 2). Major and trance element analyses were obtained at Macalester College using a Philips PW2400 X-ray fluorescence spectrometer. Analytical methods are given in Appendix 2. Samples for major element analysis include: kyanite granulite (5 samples), garnet-clinopyroxene granulite (2 samples), corona granulite (3 samples), amphibolite (5 samples), garnet-clinopyroxene amphibolite (5 samples), and garnet amphibolite (2 samples).

Major elements

Samples of the Berit metaophiolite have low SiO_2 content, between 37.10 and 49.26 wt%. Values of Na_2O (0.78–3.36 wt%) and K_2O (0.02–0.26 wt%) are also low. On a plot of total alkali-silica content modified for plutonic rocks (Middlemost, 1994), the rocks plot in the gabbro and olivine gabbro fields, reflecting their mafic protoliths (Fig. 12a). Total iron (expressed as Fe_2O_3) ranges from 2.53 to 13.31 wt%. MgO content ranges from 9.20 to 15.73 wt% with the exception of one sample of mylonitic garnet-clinopyroxene amphibolite (3.93 wt%). Plotted on an AFM diagram, these rocks fall along a tholeiitic trend (Fig. 12b). Major elements CaO (9.92–18.48 wt%) and Al_2O_3 (15.44–25.67 wt%) are also high in the Berit rocks. Calculated CIPW normative minerals plotted using the modal classification scheme of Le Maitre et al. (1989) indicate that the rocks of the Berit metagabbro unit are olivine gabbro (or norite) and troctolite (Fig. 12c). TiO_2 is typically low and varies from 0.02 to 1.52 wt%. MnO content ranges from 0.05 to 0.36 wt%. On a discrimination diagram of MnO-TiO_2/P_2O_5 (Mullen, 1983) these rocks plot in the boninite and island-arc tholeiite fields (Fig. 12d).

Table 2. Major and trace element XRF data for the Berit metaophiolite

Lithology	Amphibolite					Corona granulite		
Sample	CAT15-01dw	CAT15-07	CAT15-19B	CAT15-22	CAT15-23	25613B	CAT13-27C2	CAT15-02
Major Elements (wt. %)								
SiO_2	42.07	45.77	48.37	44.80	48.54	44.03	46.15	44.34
TiO_2	0.06	0.10	0.13	0.58	0.67	0.03	0.07	0.02
Al_2O_3	22.86	19.16	16.33	16.42	16.59	23.22	24.30	25.67
Fe_2O_3*	4.61	4.34	3.69	7.84	8.47	4.29	3.27	3.31
MnO	0.07	0.08	0.07	0.14	0.14	0.06	0.05	0.05
MgO	14.41	13.12	12.82	12.75	9.33	15.18	10.42	12.25
CaO	11.94	12.65	15.65	14.67	12.82	11.70	14.27	13.30
Na_2O	1.74	2.21	1.31	0.99	2.76	1.00	1.14	1.04
K_2O	0.12	0.20	0.04	0.06	0.10	0.02	0.02	0.03
P_2O_5	0.01	0.01	b.d.	0.02	0.03	0.01	b.d.	b.d.
LOI	1.45	2.21	1.80	1.80	0.65	0.70	0.89	0.60
Total	99.34	99.83	100.22	100.06	100.11	100.25	100.57	100.60
Trace Elements (ppm)								
Sc	6.8		44.4		41.3	7.2	12.4	7.0
V	21.9		117.4		213.9	11.8	28.6	6.6
Cr	2759.3		711.0		353.8	487.2	500.7	105.3
Co	44.0		37.0		41.6	47.0	31.7	38.0
Ni	492.7		209.7		113.8	521.0	352.1	466.4
Cu	b.d.		64.2		46.3	22.3	17.9	b.d.
Zn	18.5		13.6		47.1	18.6	14.8	14.2
Ga	10.7		8.8		13.6	9.4	10.7	10.0
Rb	2.6		0.4		1.5	1.2	0.6	0.8
Sr	421.0		110.0		251.2	110.7	150.2	102.3
Y	1.1		3.4		13.6	0.2	0.9	0.1
Zr	6.1		1.3		23.0	0.9	0.6	0.1
Nb	0.3		0.3		0.9	0.3	0.3	0.3
Ba	21.9		0.8		10.9	11.3	10.4	0.5
La	3.3		0.7		b.d.	b.d.	b.d.	b.d.
Ce	b.d.		b.d.		5.5	b.d.	0.9	2.6
Nd	7.2		0.9		7.4	2.6	2.7	3.4
Sm	0.8		b.d.		1.8	b.d.	1.5	1.9
Yb	12.1		6.5		5.2	12.2	9.3	12.5
Hf	b.d.		b.d.		0.7	0.8	b.d.	b.d.
Ta	0.7		2.2		1.2	1.0	1.1	0.4
Pb	b.d.		2.0		2.8	0.6	1.4	0.6
Th	3.2		1.3		2.1	1.1	1.2	1.5
U	1.8		1.3		1.1	0.9	1.0	0.2

* - Total iron as Fe_2O_3; LOI - loss on ignition; b.d. - below detection limit

Table 2 (continued)

Lithology	Grt-Cpx granulite		Ky granulite				
Sample	CAT15-09A	CAT15-26B	25613K	25613O	CAT15-08B	CAT15-11	CAT15-24
Major Elements (wt. %)							
SiO_2	45.82	45.81	46.09	45.73	48.82	46.22	47.72
TiO_2	0.05	0.07	0.16	0.04	0.14	0.15	0.10
Al_2O_3	24.52	23.32	18.63	25.64	15.44	18.53	16.64
Fe_2O_3*	3.39	3.96	6.78	2.81	2.92	4.78	4.15
MnO	0.05	0.06	0.12	0.05	0.06	0.10	0.08
MgO	10.41	10.94	13.44	9.20	11.78	12.01	14.54
CaO	13.88	14.21	14.13	14.22	18.48	16.84	15.70
Na_2O	1.43	1.38	1.05	1.50	1.22	0.90	0.93
K_2O	0.18	0.04	0.04	0.10	0.14	0.04	0.05
P_2O_5	0.01	0.01	0.06	0.01	b.d.	0.01	0.01
LOI	0.87	0.63	0.24	1.27	0.98	0.62	0.20
Total	100.62	100.41	100.72	100.57	99.98	100.19	100.12
Trace Elements (ppm)							
Sc	12.7			10.8			36.5
V	28.2			22.4			104.0
Cr	559.6			330.0			2690.1
Co	34.7			33.1			42.1
Ni	331.3			259.8			353.9
Cu	108.5			1.4			111.3
Zn	19.1			9.7			19.7
Ga	10.7			11.7			8.0
Rb	4.4			2.3			1.8
Sr	119.0			188.7			60.4
Y	0.8			0.6			2.3
Zr	1.0			0.9			2.1
Nb	0.4			0.4			0.5
Ba	53.3			32.2			10.7
La	b.d.			b.d.			b.d.
Ce	b.d.			b.d.			b.d.
Nd	1.7			b.d.			4.0
Sm	b.d.			3.1			b.d.
Yb	9.7			7.1			11.4
Hf	b.d.			0.9			0.1
Ta	0.7			1.1			1.2
Pb	1.2			0.8			1.6
Th	1.6			1.7			1.8
U	0.5			0.7			b.d.

Table 2 (continued)

Lithology	Grt-Cpx amphibolite					Grt amphibolite	
Sample	CAT13-25A	CAT13-25C	26613B	CAT15-17B	CAT15-28	CAT15-04B	CAT15-12B
Major Elements (wt. %)							
SiO_2	48.78	46.36	48.33	49.26	48.38	40.45	37.10
TiO_2	0.21	0.15	0.99	0.55	0.47	1.52	1.34
Al_2O_3	17.23	23.98	15.66	16.62	17.21	16.84	18.58
Fe_2O_3*	6.66	9.92	9.83	8.43	8.28	14.79	13.46
MnO	0.18	0.36	0.13	0.13	0.14	0.34	0.27
MgO	10.67	3.93	9.24	8.88	9.17	11.55	11.49
CaO	12.90	9.92	13.15	13.11	12.65	12.75	12.50
Na_2O	2.06	3.36	2.07	2.79	2.96	0.83	2.01
K_2O	0.11	0.12	0.08	0.05	0.04	0.05	0.26
P_2O_5	0.02	0.52	0.03	0.02	0.01	0.02	0.31
LOI	1.32	1.99	0.75	0.51	0.87	1.38	2.55
Total	100.15	100.60	100.27	100.36	100.19	100.53	99.87
Trace Elements (ppm)							
Sc	46.1		46.2	44.7	47.8	46.8	47.1
V	137.4		295.9	203.0	209.1	485.1	477.3
Cr	605.5		238.1	274.8	281.7	288.7	17.4
Co	35.9		46.0	43.9	47.9	55.3	49.5
Ni	150.4		76.2	96.8	100.8	243.5	89.7
Cu	47.8		83.9	43.5	53.1	b.d.	44.5
Zn	46.7		46.4	47.1	45.6	49.7	34.6
Ga	11.3		14.7	14.6	14.6	10.1	15.7
Rb	1.2		1.4	1.0	0.9	0.3	4.2
Sr	172.9		144.5	152.9	155.9	44.7	319.6
Y	9.5		20.4	13.1	11.2	22.5	35.6
Zr	11.0		21.6	14.0	10.8	39.2	49.3
Nb	0.2		0.7	0.7	0.5	4.5	3.8
Ba	15.3		3.1	14.1	2.4	0.9	67.4
La	b.d.		b.d.	b.d.	b.d.	b.d.	22.7
Ce	b.d.		5.7	1.6	2.5	6.0	45.6
Nd	4.5		9.3	6.2	4.7	8.8	24.2
Sm	1.1		1.7	4.5	0.1	0.2	3.7
Yb	6.8		6.8	5.2	4.9	9.9	7.5
Hf	b.d.		2.7	b.d.	0.5	b.d.	2.8
Ta	0.9		0.8	0.9	0.8	0.4	2.3
Pb	1.5		1.3	0.5	0.8	1.6	1.7
Th	1.6		2.2	2.7	2.1	1.7	7.1
U	1.1		1.1	1.0	1.0	1.1	3.8

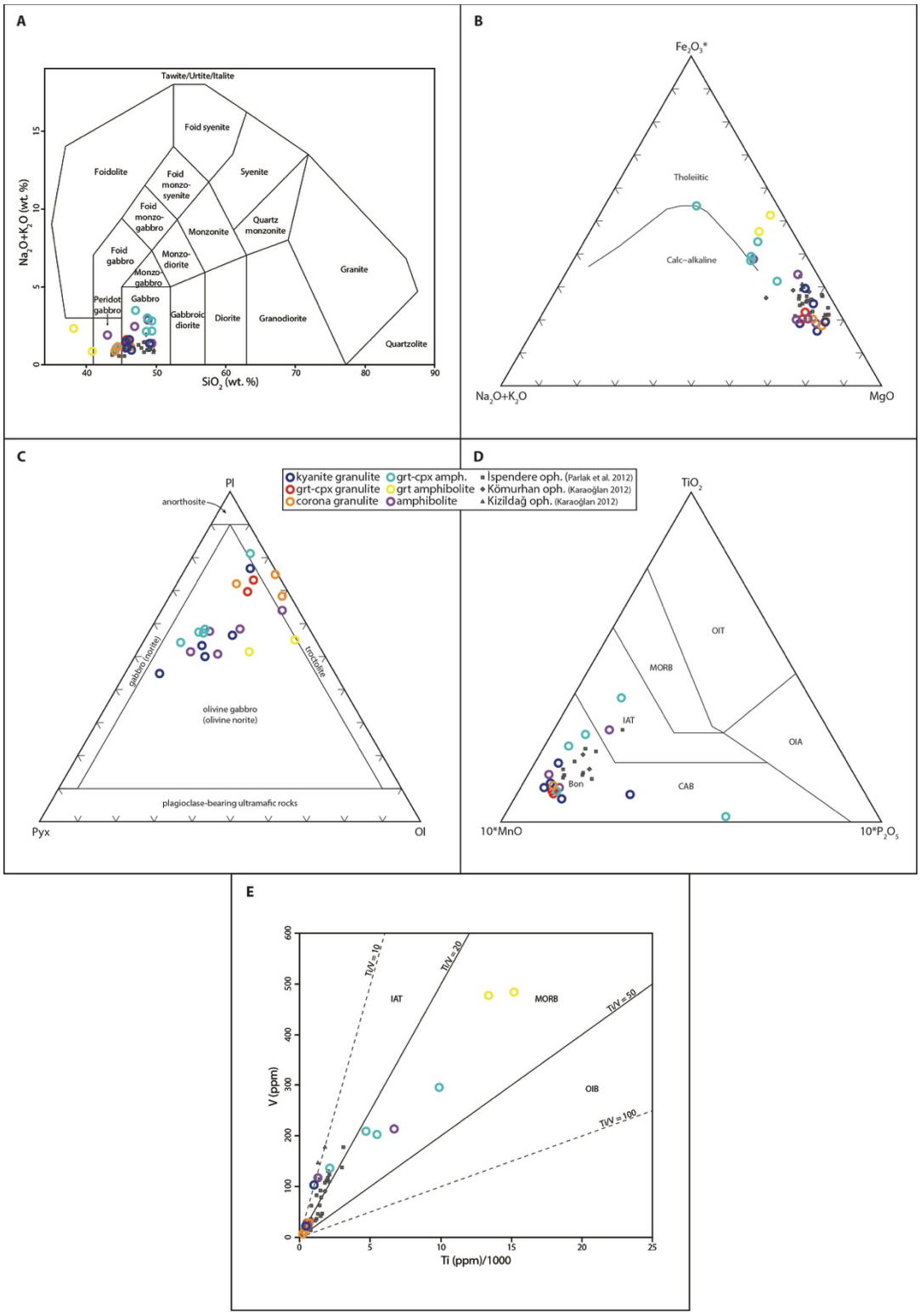

Figure 12. Geochemical classification and discrimination diagrams of selected Berit lithologies. A) Total alkali-silica plot (Middlemost, 1994). B) AFM diagram. C) CIPW normative minerals (LeMaitre et al., 1989). D) MnO-TiO_2/P_2O_5 discrimination diagram after Mullen (1983). E) Ti/V discrimination diagram (Shervais, 1982). IAT, island arc tholeiite; MORB, mid-ocean ridge basalt; OIT, ocean island tholeiite; OIA, ocean island alkaline basalt; OIB, ocean island basalt.

Trace elements

Owing to the potential mobility of some elements during alteration and metamorphism, immobile trace elements (e.g. Ti, Zr, Y) are used for classification and discrimination of oceanic crustal rocks. The high field strength elements: Zr (0.1-49.3 ppm), Nb (0.2-4.5 ppm), and Y (0.1-35.6 ppm) have low abundances in the Berit metagabbroic rocks. Cr values are highly variable in the Berit rocks (17.4-2759.3 ppm). The host amphibolites and granulites commonly have the highest values, whereas the garnet-clinopyroxene amphibolite and garnet amphibolite have typically lower values. Ni (76.2-521.0) mimics the variation of Cr. Co is consistent in all samples (31.7-55.3 ppm). The granulites and amphibolites have low values of V (6.6-213.9 ppm), whereas the garnet-bearing amphibolites typically have higher values (137.4-485.1 ppm). On a plot of Ti/V (Shervais, 1982) the Berit rocks plot in the island-arc tholeiite and mid-ocean ridge basalt fields (Fig. 12e).

Thermobarometry

Granulites

Petrography and mineral chemistry show that there is extensive evidence for textural and compositional disequilibrium within the Berit granulites. Corona and symplectite textures, as well as compositional zoning within garnet, clinopyroxene, and plagioclase, complicate the interpretation of equilibrium relationships among phases and thus the use of traditional exchange and net transfer reactions for geothermobarometry. In order to determine *P-T* conditions and assess metamorphic paths, equilibrium assemblage

diagrams (pseudosections) are calculated from whole-rock analyses for representative samples of the Berit granulites.

Pseudosection modeling is also not immune to the textural complexities exhibited by the Berit granulites. For example, the presence of corona structures suggests the existence of chemical domains, indicating that the measured bulk composition does not reflect the *effective* bulk composition during much of the metamorphism. Instead, efforts must be made to model the effective bulk composition of the rock. One method of estimating the effective bulk composition at the peak of metamorphism involves identifying phases that do not appear to be in equilibrium with the rest of the assemblage (sites of potential chemical sequestration) and removing those phases from the bulk composition. Similar approaches have been successfully implemented by other workers to model the *P-T* conditions of texturally complex rocks (Tinkham and Ghent, 2005; Goergen and Whitney, 2012; Haifler and Kotková, 2016).

Pseudosections were calculated using the software package Perple_X (Connolly, 2009) version 6.6.6 using the hp04ver.dat thermodynamic data set. Calculations were performed in the MnO-Na_2O-CaO-FeO-MgO-Al_2O_3-SiO_2-TiO_2 (MnNCFMAST) system, which is representative of the Berit granulites (Table 2). K was ignored as there are no significant K-bearing phases. In addition, Fe^{3+} was not considered because mineral compositions suggest that Fe^{3+} is not present in substantial amounts, however this remains a potential source of error in these calculations (Appendix 3). Minor element Ti was included because rutile is present in the granulite assemblage. Although Mn is present only as minor spessartine in garnet, it was included so as to ensure the accuracy of the stability field of garnet. Calculations were performed with no H_2O. The granulites

are assumed to be dry because hydrous phases (e.g. amphibole, zoisite, chlorite) appear to be texturally secondary. The following solution models are used in the calculations: Opx(HP) (orthopyroxene, Powell and Holland, 1999), Gt(HP) (garnet, Holland and Powell, 1998), Omph(GHP2) (clinopyroxene, Diener and Powell, 2012), O(HP) (olivine, Holland and Powell, 1998), Sapp(HP) (sapphirine, Holland and Powell, 1998), and Pl(h) (feldspar, Newton et al., 1980). The omphacitic clinopyroxene model is chosen to assess changes in X_{Jd} at high pressure and binary plagioclase is used because K is ignored.

Corona granulite (CAT15-02)

The presence of clinopyroxene and garnet coronas on orthopyroxene suggest disequilibrium in the corona granulites, requiring careful interpretation of calculated phase diagrams. Observed modal abundances of garnet (26%), and plagioclase (31%) in the stability field of sapphirine are in close agreement with calculated values at 700-900°C and 0.9-1.1 GPa, suggesting partial equilibration at or near these conditions (Fig. 13a, Table 1). The orthopyroxene and garnet-in boundaries are relatively flat, suggesting that reactions producing or consuming these phases are highly *P* dependent. The sapphirine-out and corundum-in boundaries are closely associated and appear *P* and *T* dependent, suggesting that the two are related by reactions that occur as a result of decreasing temperature or increasing pressure.

In order to assess the influence of corona formation on phase composition, a *P*-*X* phase diagram was calculated at 800°C and orthopyroxene was removed from the bulk composition (Fig. 13b). Garnet compositional isopleths are sensitive to the removal of orthopyroxene, as both are major Mg-bearing phases. Garnet coronas are zoned in X_{prp}

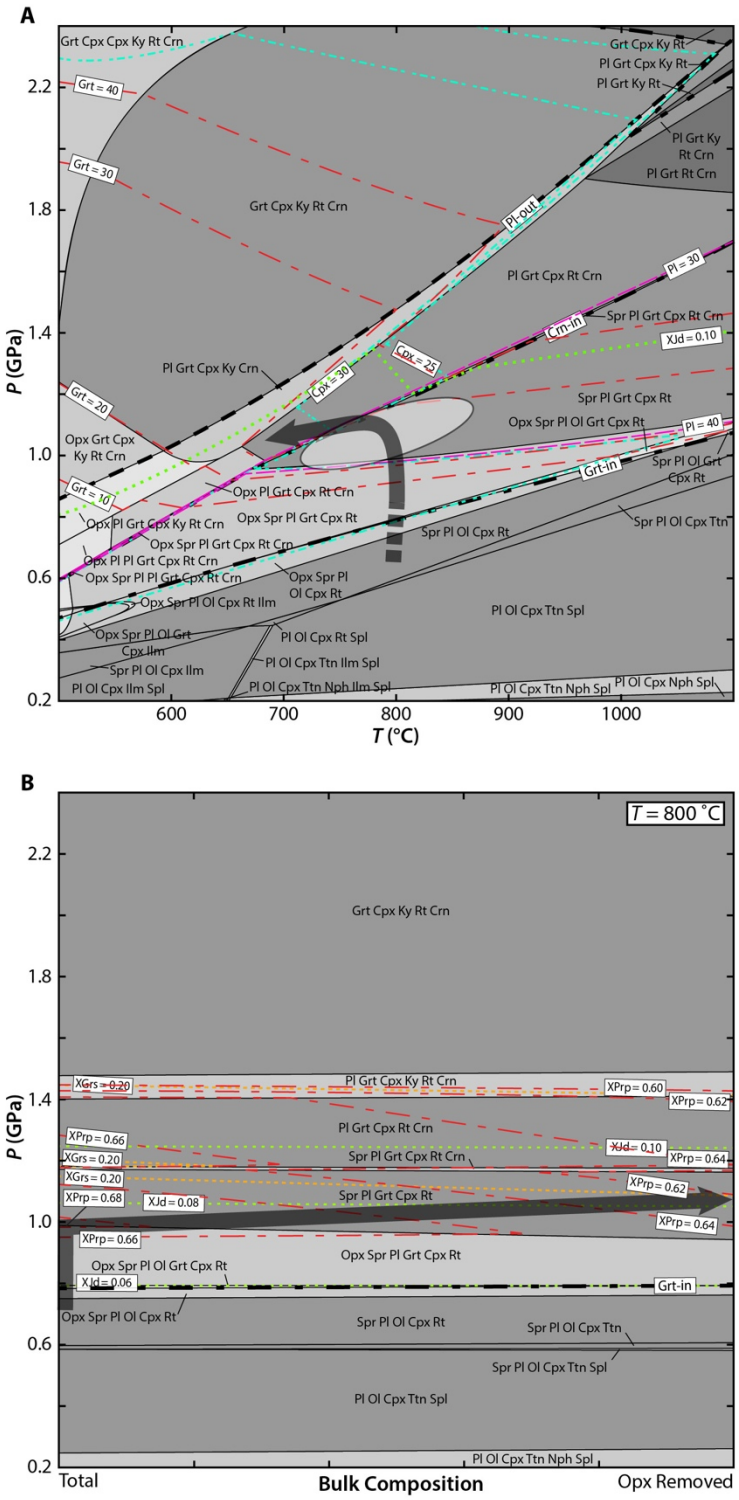

Figure 13. Pseudosections calculated for corona granulite sample CAT15-02. A) P-T diagram, with an ellipse indicating an area of stability consistent with modal abundance of Grt + Pl. The arrow represents an inferred path based on compositional zoning and modal abundances. B) P-X diagram, where X ranges from the measured bulk composition to Opx-removed composition (SiO_2 43.99, TiO_2 0.02, Al_2O_3 26.75, FeO 2.89, MnO 0.05, MgO 11.22, CaO 13.96, Na_2O 1.10). Arrow based on compositional zoning in garnet.

and X_{grs} from inner rim ($X_{prp} \approx 0.69$, $X_{grs} \approx 0.15$) to outer rim ($X_{prp} \approx 0.64$, $X_{grs} \approx 0.21$) and contain inclusions of sapphirine. This zoning is consistent with increasing effective removal of orthopyroxene from the bulk composition between 1.0 and 1.1 GPa around 800°C. Calculated modal abundance of clinopyroxene increases while garnet abundance decreases with cooling to 650-700°C at ~1.1 GPa. Cooling would also stabilize corundum at the expense of sapphirine, consistent with the formation of clinopyroxene-corundum symplectites after garnet and sapphirine.

Garnet-clinopyroxene granulite (CAT15-09A)

Like the corona granulites, the garnet-clinopyroxene granulite is clearly not fully equilibrated. The presence of trace amounts of orthopyroxene and cores of low-Na plagioclase ($X_{Ab} = 0.23$) indicate that the sample initially experienced orthopyroxene-stable conditions below 1.0 GPa (Fig. 14). Corona-like textures in the rock suggest a similar initial prograde path to the corona granulites. Isopleths for modal abundances of garnet (39%) and clinopyroxene (38%) overlap at 750-900°C and 1.1-1.5 GPa supporting partial equilibration at or near those conditions. Further pressure increase or cooling would move the rock into the kyanite stability field and eventually into plagioclase-free conditions. Calculated isopleths of X_{Ab} and X_{Jd} show increasing albite in the plagioclase and jadeite in the clinopyroxene along these paths. Simultaneously, modal abundance of plagioclase decreases and clinopyroxene and kyanite increase. This is consistent with core ($X_{Ab} \approx 0.30$) to rim ($X_{Ab} \approx 0.65$) increase of Na in plagioclase as well as jadeite-rich clinopyroxene in the kyanite-clinopyroxene symplectites ($X_{Jd} = 0.13$-0.18). Cooling to ~700°C at 1.3 GPa would also result core to rim increases in Ca and Fe^{2+} content in

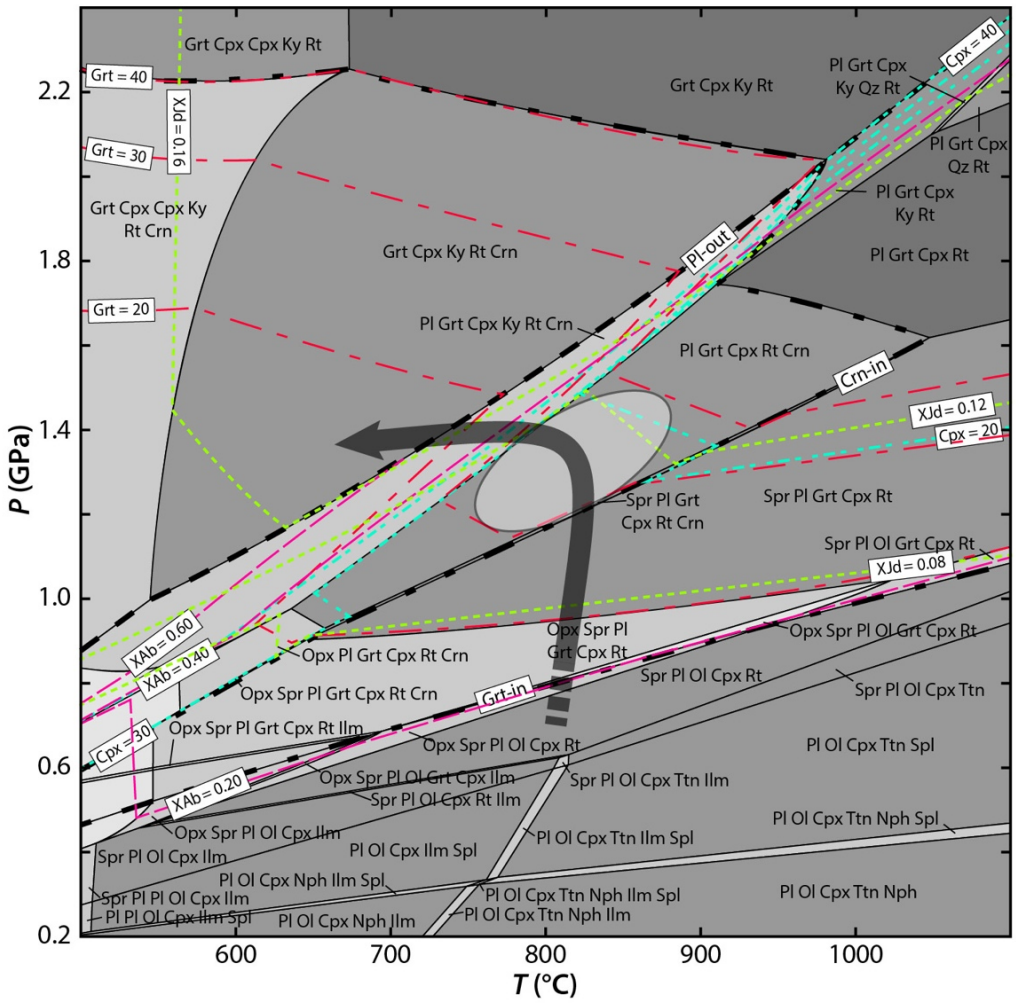

Figure 14. Pseudosection calculated for Grt-Cpx granulite sample CAT15-09A. Ellipse shows a region of stability consistent with modal amounts of Grt + Cpx. The arrow indicates an inferred path based on isopleths of clinopyroxene and plagioclase composition, as well as the presence of kyanite in symplectite.

garnet similar to observed compositional zoning. An increasing temperature path would not produce the same zoning.

Kyanite granulite (CAT15-24)

The assemblage of garnet + clinopyroxene + kyanite without plagioclase indicates that the rock equilibrated outside of the plagioclase stability field (Fig. 15). Isopleths of garnet composition (X_{prp} = 0.6, X_{grs} = 0.2, and X_{grs} = 0.2) intersect at 650-750°C and 1.2-

1.5 GPa. These are consistent with modal amounts of clinopyroxene (59%) in the sample (Table 1). The phase diagram accurately predicts other modal and compositional characteristics of the kyanite granulite. For example, X_{Jd} values between 0.08 and 0.12 agree with the region of intersection of garnet isopleths and modal clinopyroxene. Modal abundance of garnet in this region is within 5% of the observed value. Exceptions are modal abundances of kyanite and corundum, which have observed abundances ~6% higher and ~2% lower, respectively, than calculated values.

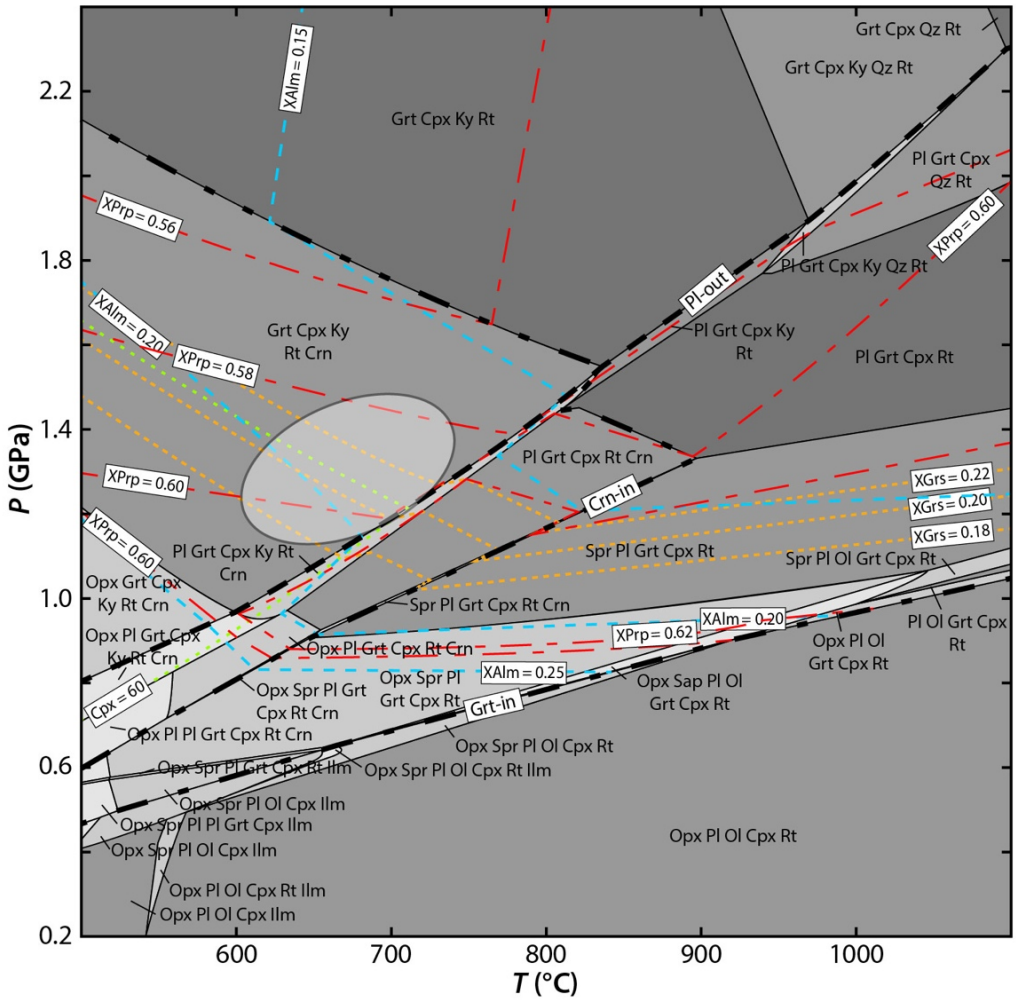

Figure 15. Pseudosection calculated for kyanite granulite sample CAT15-24. Ellipse indicates a region of stability inferred from modal abundance of clinopyroxene and isopleths of garnet composition.

Amphibolite (CAT15-23)

Field and petrographic evidence indicates that amphibolite formed by retrograde hydration of granulite. In order to characterize the retrograde *P-T* path, hornblende-plagioclase thermometers and barometers are applied to a sample of the amphibolite facies host rocks to granulite pods. As hornblende and plagioclase are both zoned, core and rim pairs were chosen for thermobarometry. The thermometer of Holland and Blundy (1994) and barometer of Molina et al. (2015), both of which are applicable to quartz-free assemblages, were applied to the sample (Fig. 16). Hornblende-plagioclase cores give estimates of $T = 700$°C and $P = 8$ GPa. Rim analyses give estimates of of $T = 615$°C and $P = 5$ GPa. It is noted, however, that the calculated rim T falls below the suggested temperature range for the hornblende-plagioclase barometer (i.e., < 650°C).

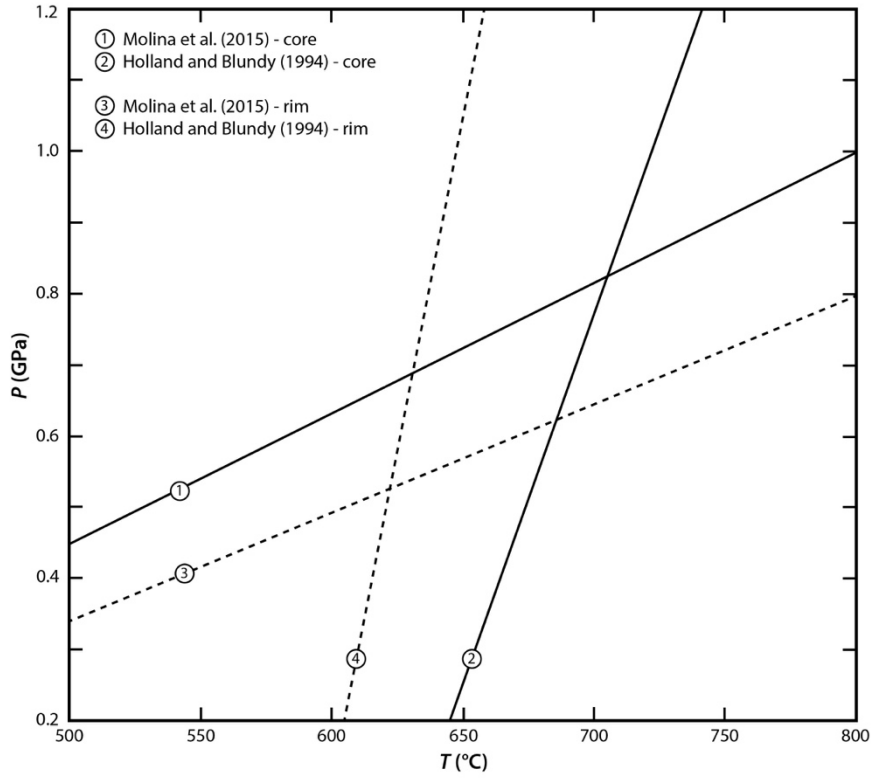

Figure 16. Pressure-temperature plot showing representative equilibria for hornblende-plagioclase thermometry and barometry of the amphibolite. Reported accuracies are ±40°C for the Holland and Blundy (1994) thermometer and ±0.23 GPa for the barometer of Molina et al. (2015).

Discussion

Interpretation of the formation and evolution of the Berit mafic granulites and associated rocks must address their protoliths, *P-T* conditions, and *P-T-d* paths. The following will discuss the implications of the geochemistry, petrography, and thermobarometry results for these interpretations. Whole-rock geochemistry is used to infer the protoliths for the Berit metaophiolitic rocks. Integrating the results of pseudosection modeling with analysis of key textures allows for the determination of *P-T* paths. In turn, the characteristics of the protoliths and *P-T* paths reflects the tectonic development of the Berit metaophiolite and the Tauride margin.

Interpretation of geochemical characteristics

The major and trace element geochemistry of the Berit granulites and host amphibolite indicate gabbroic cumulate protoliths (Fig. 12). Plotted on an AFM diagram, the Berit rocks fall along a tholeiitic trend consistent with crystallization and removal of Mg-rich phases (Fig. 12b). High wt% CaO and Al_2O_3 reflect Ca-plagioclase crystallization and accumulation. The relatively high values of Cr, Co, and Ni in the granulite and amphibolite rocks are in agreement with crystal accumulation or fractionation of clinopyroxene, spinel, and olivine. Low abundances of high field strength elements (e.g. Zr, Nb, Y) are similarly consistent with cumulus minerals. Minor and trace element discrimination diagrams suggest that the granulites and host amphibolites are similar to supra-subduction zone (SSZ) island-arc tholeiites or boninites (Fig. 12d, e). The differing trace (and major) element characteristics of the garnet-clinopyroxene amphibolite and garnet amphibolite may reflect different protoliths for those rocks. This

is similar to the results of previous work suggesting that the garnet-clinopyroxene amphibolites resemble normal mid-ocean ridge basalt (N-MORB) (Parlak et al., 2009; Karaoğlan et al., 2013).

The granulite pods and amphibolite host rocks appear to be geochemically similar to other Neotethyan SSZ ophiolites. Cumulate gabbro and troctolite from the Ispendere, Kömürhan, and Kızıldağ ophiolites fall within similar ranges as the Berit metaophiolite samples on classification and discrimination diagrams (Fig. 12) (Parlak et al., 2012; Karaoğlan, 2012). Despite the potential for element mobility during metamorphism and metasomatism, the Berit granulite and amphibolite facies rocks seem to maintain the geochemical characteristics of SSZ ophiolite cumulate gabbros. These interpretations are consistent with previous geochemical studies that have proposed subduction-influenced tholeiite protoliths for the granulites and amphibolites (Parlak et al., 2009; Karaoğlan et al., 2013).

Interpretation of key textures

Clinopyroxene-garnet coronas between orthopyroxene and plagioclase may have formed during prograde metamorphism of gabbro to high-pressure granulite facies. Pseudosection modeling of the corona granulite shows that garnet-in and orthopyroxene-out reactions are highly *P* dependent, as are isopleths of modal abundance of clinopyroxene and garnet (Fig. 13). The appearance of garnet with increasing pressure indicates the transition from medium- to high-pressure granulite facies (e.g., O'Brien and Rötzler, 2003). Incomplete transformation of orthopyroxene to garnet and clinopyroxene may reflect limited diffusion of elements owing to dry conditions and/or increasing

diffusion distances between plagioclase and orthopyroxene during *P* increase (Indares, 1993; Indares and Rivers, 1995; Arenas and Martínez Catalán, 2002). Progressive removal of orthopyroxene from the bulk composition in a *P-X* pseudosection predicts changes in garnet composition similar to observed zoning and consistent with a prograde increase in pressure (Fig. 13). Similar garnet and clinopyroxene coronas from the Ordenes Complex of the Iberian Massif (Spain) are interpreted to have been produced by a nearly isothermal increase in pressure from ~0.6 GPa to >1.5 GPa at ~700 °C (Arenas and Martínez Catalán, 2002). The Berit corona granulites may have experienced a similar *P-T* path involving relatively little change in temperature. Such a path requires a tectonic setting in which thickening, loading, or burial is achieved without dramatic changes in temperature.

The symplectic coronas of clinopyroxene-corundum around garnet appear to be related to the reaction of garnet, sapphirine, and plagioclase:

$$\mathrm{Grt + Spr + Pl = Cpx + Crn}$$

Pseudosection modeling suggests that this texture is produced by isobaric cooling from peak *T* (Fig. 13a). A decrease in temperature with negligible decompression would simultaneously stabilize corundum and increase modal clinopyroxene while decreasing modal abundance of garnet and consuming sapphirine. Based on the presence of coarse-grained plagioclase and the lack of corundum observed in equilibrium with garnet, it is unlikely that the symplectite could be formed by another mechanism (e.g. isothermal decompression).

The kyanite-clinopyroxene symplectites in garnet-clinopyroxene granulites and kyanite granulites could also be produced by isobaric cooling at high pressure. Previous

workers have suggested that kyanite-clinopyroxene-plagioclase symplectites in the Berit granulites formed as a result of the breakdown of garnet during isothermal decompression (Karaoğlan et al., 2013). However, plagioclase occurs as isolated anhedral grains surrounded by Cpx+Ky symplectite, suggesting that plagioclase is a reactant rather than a product (Fig. 9c). This interpretation is consistent with pseudosection modeling, which suggests that isobaric cooling at high pressures would result in the crystallization of kyanite and clinopyroxene at the expense of plagioclase and garnet (Fig. 14). This may reflect a reaction such as:

$$Grt + Pl = Cpx + Ky$$

Pseudosections similarly predict observed decreasing Mg in garnet from core to rim, increasing Na from core to rim in plagioclase, and symplectitic clinopyroxene with higher Jd content than matrix clinopyroxene. Cooling was probably rapid in order to create and preserve the symplectite texture (Griffin, 1971; Passchier and Trouw, 2005).

Comparable kyanite-omphacite intergrowths have been identified in gabbroic granulite and eclogite nodules in kimberlites from the Congo and Lesotho (Griffin et al., 1979; El Fadili and Demaiffe, 1999). These intergrowths are similarly interpreted as a product of the breakdown of plagioclase during high-pressure isobaric cooling.

P-T path and tectonic interpretations

The results of petrography and pseudosection modeling of the Berit granulites suggest that they followed an anticlockwise *P-T* path (Fig. 17). The presence of clinopyroxene and garnet coronas on orthopyroxene indicate prograde metamorphism from medium-pressure to high-pressure granulite facies. Corona granulites experienced

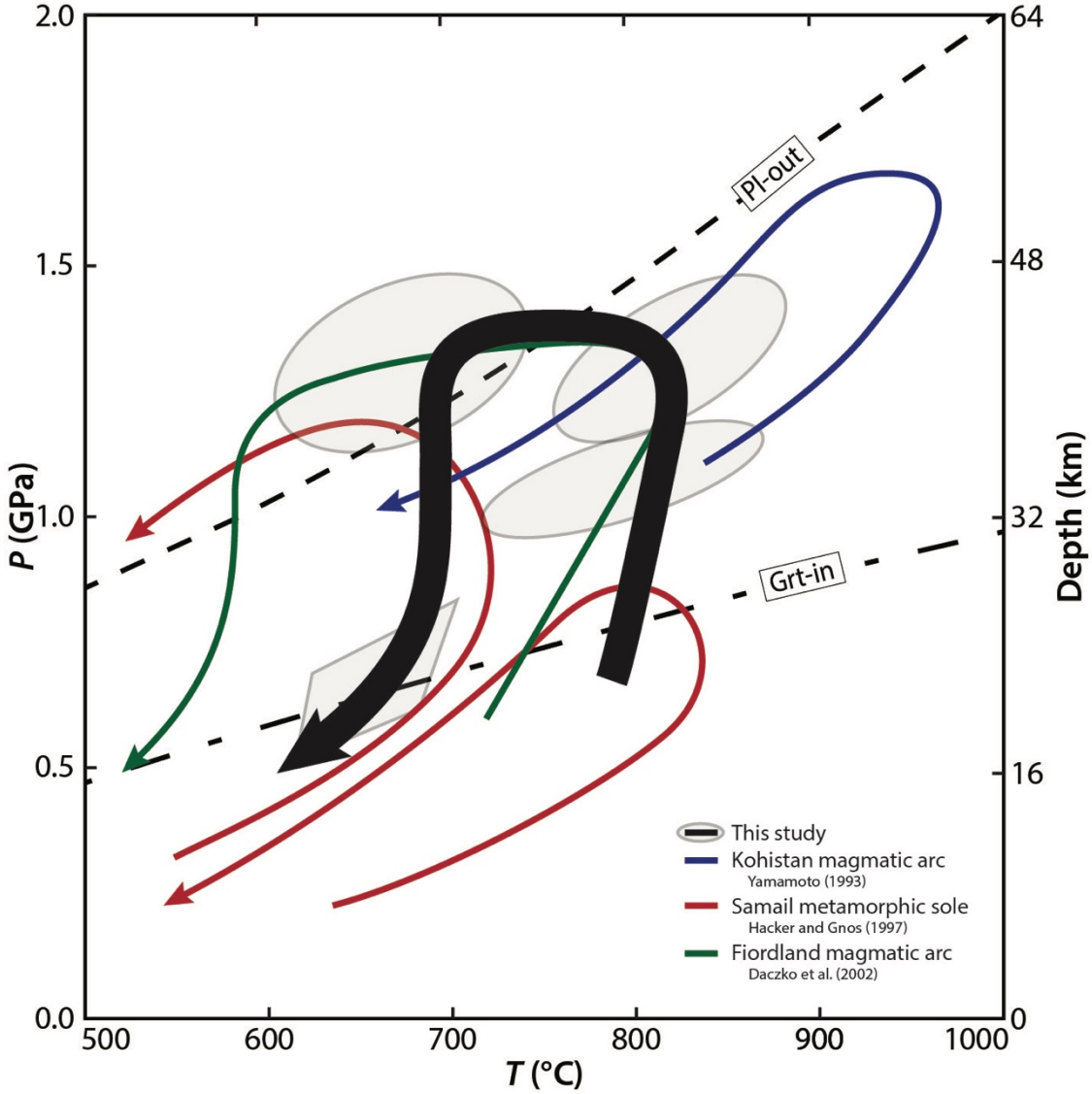

Figure 17. Pressure-temperature plot showing a generalized P-T path for the Berit granulites and ellipses from pseudosection modeling. Grt-in and Pl-out reactions are approximate. Also shown are comparative P-T paths from other granulites that show anticlockwise paths.

peak metamorphic conditions of 700-900 °C and 0.9-1.1 GPa, garnet-clinopyroxene granulites reached peak metamorphism at 750-900 °C and 1.1-1.5 GPa, and kyanite granulites are consistent with conditions of 650-750 °C and 1.2-1.5 GPa. Corundum-clinopyroxene and kyanite-clinopyroxene symplectites between garnet and plagioclase reflect isobaric cooling following the thermal peak. The occurrence of the granulite facies

rocks as pods hosted by amphibolite indicates a transition from isobaric cooling to decompression coupled with the infiltration of fluids at 615-700°C and 0.5-0.8 GPa.

The garnet-clinopyroxene granulites appear to share textural characteristics with both the kyanite granulites (Ky+Cpx symplectites) and the corona granulites (Grt coronas, Opx). The garnet-clinopyroxene granulite also occurs in close spatial proximity with both the kyanite and corona granulites. These characteristics suggest that the garnet-clinopyroxene granulites may be transitional between the kyanite granulites and corona granulites. All three lithologies are geochemically similar, although calculated CIPW norms suggest that some variation in protolith could result in the lithologic differences (Fig. 12). Alternatively, the transitional nature between the granulites could reflect variation in *P-T* conditions experienced by different structural levels of the Berit metaophiolite. The kyanite granulites would represent the highest pressure conditions (structurally lowest) portion of the Berit metagabbros, while the corona granulites suggest lower pressures (structurally highest).

Characterization of the *P-T* path experienced by the Berit granulites informs the setting and process of their formation. Two different scenarios have been proposed for the formation of the granulite facies metaophiolitic rocks in the Doğanşehir region. Parlak et al. (2004) suggested that the metaophiolitic rocks represent the metamorphic sole of oceanic crust equivalent to sole rocks in the Berit region described by Genç et al. (1993) and Yılmaz et al. (1993). More recently, Karaoğlan et al. (2013) proposed that the metamorphism of the Berit metaophiolite occurred in the root of an incipient island arc, with additional heat flow provided by a slab window or slab breakoff.

Anticlockwise *P-T* paths involving granulite facies metamorphism have been inferred for rocks in both of these tectonic settings. Metamorphic sole rocks from the Samail ophiolite (Oman) display anticlockwise paths that reach > 800 °C, ~0.9 GPa and ~700 °C, 1.2 GPa, respectively, followed by cooling and decompression (Fig. 17) (Hacker, 1991; Hacker and Gnos, 1997). Despite exhibiting similar peak conditions and *P-T* paths to the Samail ophiolite, it seems unlikely that the Berit metaophiolite rocks formed as part of a subophiolitic metamorphic sole, as they lack many of the typical characteristics of sole rocks. Metamorphic soles are typically thin (<500 m) zones of highly strained metamorphic rocks structurally underlying ophiolitic sequences (Wakabayashi and Dilek, 2003). Soles commonly display inverted metamorphic gradients from granulite to greenschist facies. The Berit metaophiolitic rocks in Doğanşehir demonstrate neither an inverted metamorphic gradient nor a thin zone of highly strained metamorphic rocks that would distinguish them as a metamorphic sole.

Anticlockwise *P-T* paths recorded by granulite facies rocks have also been attributed to magmatic loading or tectonic thickening of previously heated crust. Such a scenario is common among granulites formed at mid- to lower-crustal levels in continental and island arc settings (Bohlen, 1987; Harley, 1989). Granulites in the Jijal Complex of the Kohistan island arc are interpreted to have formed as a result of magmatic loading and show anticlockwise *P-T* paths similar to those of the Berit granulites (Fig. 17) (Yamamoto, 1993; Yamamoto and Yoshino, 1998; Dhuime et al., 2009; Petterson, 2010). The Jijal granulites reached comparable metamorphic conditions (1.0-1.7 GPa and 700-950 °C) and have been used to infer crustal thicknesses of 30-50 km (Petterson, 2010, and references therein). If the Berit granulites formed as a result of

similar processes within an island arc, it is likely that similar crustal thicknesses must have been attained. Karaoğlan et al. (2013) invoke an island-arc setting coupled with increased heat flow to explain the H*T* conditions displayed by the Berit granulites, however conditions experienced by the Jijal granulites suggest that these temperatures can be achieved in arcs with typical geothermal gradients.

Some continental magmatic arcs also display anticlockwise *P*-*T* paths similar to the Berit granulites. High-pressure granulite formation in the Fiordland Complex of New Zealand is attributed to initial magmatic loading and heating of a continental magmatic arc followed by contractional thickening (Fig. 17) (Brown, 1996; Daczko et al., 2002; Klepeis et al., 2004; Flowers et al., 2005). Granulites of the Arthur River Complex and Western Fiordland Orthogneiss preserve an early medium-*P* metamorphic event ($P < 0.8$ GPa, $T > 700$ °C) followed by high-*P* metamorphism ($P \leq 1.6$ GPa, $T > 750$ °C). The high-*P* metamorphic event is followed by ~200 °C of rapid isobaric cooling (Daczko et al., 2002; Flowers et al., 2005). Rapid cooling is attributed to the juxtaposition of cold upper crust with the hot rocks during convergence (Daczko et al., 2002).

Unlike the Berit metaophiolite, however, the Jijal and Fiordland granulites are associated with extensive exposure and thick sections of arc-related crust. Considering the exposed thickness of the Berit metaophiolitic rocks and lack of associated arc rocks, it is unclear whether the necessary crustal depths could have been attained within an island arc that was subsequently accreted to the Tauride plate. However, it is possible that these rocks simply lack exposure or have not yet been identified.

Magmatic loading/underplating of the Tauride continental margin could account for the necessary crustal thickness without requiring development of a 30-50 km thick

island arc. Ophiolitic rocks already emplaced within or at the base of the Tauride plate could experience H*P*-H*T* metamorphism as a result of magmatic underplating and intrusion into the crust.

In this scenario, the Berit ophiolitic rocks were accreted to the base of the overriding Tauride crust, similar to other Neotethyan ophiolites (e.g. Ispendere, Kömürhan, Guleman) (Parlak et al., 2004; Robertson et al., 2007; Parlak et al., 2009; Karaoğlan et al., 2013). Continued subduction along this margin could produce calc-alkaline magmas that underplated and/or intruded the accreted ophiolitic rocks and Tauride crust, producing the prograde pressure increase recorded by the Berit granulites. Crystallization ages for the Doğanşehir granitoids (54-46 Ma) suggest that their intrusion may have preceded exhumation of the Berit metaophiolite, and could be related to magmas responsible for loading and prograde metamorphism (Karaoğlan, et al., 2013; Karaoğlan et al., 2016). Alternatively, if loading was due primarily to underplating, there may not be exposure of the magmatic rocks responsible for the H*P* metamorphism. This could be the result of delamination of the underplated material following the H*P*-H*T* metamorphism, or simply a lack of surface exposure of these rocks.

Loading of the crust by intrusion or underplating triggered the H*P* granulite facies metamorphism of the ophiolitic rocks and was followed by rapid cooling to produce the symplectite textures. Thermal relaxation is often invoked for isobaric cooling of high-pressure rocks, but the conclusion that cooling must have been rapid requires a different mechanism. Rapid cooling at high pressure could be produced by juxtaposition of relatively cold crust with the hot granulites (Perchuk and Philippot, 1997; Daczko et al., 2002). Continued subduction of Neotethyan oceanic lithosphere beneath the Tauride

margin or intra-plate thrusting are potential mechanisms for juxtaposition of cooler crust with the H*T* granulite facies rocks.

Subsequent development of an inter-arc or back-arc rift (perhaps by slab rollback) and formation of the Maden rift basin likely resulted in the extension-driven exhumation of the granulite facies rocks. Continued arc magmatism and intrusion of the Doğanşehir granitoid occurred coevally with the granulite cooling and exhumation. Decompression and fluid infiltration related to extension caused the widespread retrogression (amphibolitization) of the Berit granulite-facies rocks. Folding of the Berit metaophiolitic rocks may have occurred during late contraction of the Tauride margin or Oligo-Miocene continental collision between the Tauride and Arabian plates.

Arguments can be made for the formation of the Berit granulites in both island arc and continental arc settings. However, without strong evidence of thickened arc crust accreted to the Tauride margin, the interpretation that metamorphism occurred in a Tauride continental magmatic arc is preferred. Intrusion or underplating of arc magmas is consistent with the prograde metamorphism of the granulites to temperatures and pressures of ~700-900 °C and 1.1-1.5 GPa followed by rapid isobaric cooling and subsequent decompression. Coeval cooling of the Berit granulites (52-50 Ma) and intrusion of the Doğanşehir granitoid are attributed to incipient rifting and basin formation recorded by the Maden Group sediments and volcanic rocks. This interpretation indicates that subduction of oceanic lithosphere in the Southern Neotethys continued well into the Eocene and that collision between the Tauride and Arabian plates could not have occurred until significantly later.

Conclusions

The Berit metaophiolite in Doğanşehir contains a suite of mafic granulite and amphibolite facies rocks that trace the geochemical, metamorphic, and structural evolution of the southeast Anatolian plate margin. The granulite facies metagabbroic rocks occur as meter-scale ellipsoidal pods hosted by folded amphibolite. Geochemically, the granulite pods and amphibolite host rocks resemble supra-subduction zone island arc tholeiites. High CaO, Al_2O_3, Cr, and Ni are consistent with accumulation of Ca-plagioclase, clinopyroxene, and olivine, indicating that the rocks had cumulate gabbro protoliths. Mineral textural evidence combined with pseudosection modeling suggest the granulite facies rocks followed an anticlockwise *P-T* path. Corona structures of clinopyroxene and garnet on orthopyroxene are indicative of an initial prograde pressure increase. Isopleths of mineral chemistry and modal abundance calculated for the granulites indicate peak conditions between 700-900 °C and 1.1-1.5 GPa. Corundum-clinopyroxene and kyanite-clinopyroxene symplectites are suggestive of rapid isobaric cooling from the thermal peak. Granulite-hosting amphibolites formed at 615-700 °C and 0.5-0.8 GPa as a result of retrograde hydration of the granulites. The anticlockwise *P-T* path is attributed to magmatic loading in an Eocene continental magmatic arc or island arc setting, followed by extension and exhumation. This interpretation suggests that subduction of oceanic crust in the Southern Neotethys occurred into the Eocene.

References

Allen, M.B., and Armstrong, H.A., 2008, Arabia-Eurasia collision and the forcing of mid-Cenozoic global cooling: Palaeogeography, Palaeoclimatology, Palaeoecology, v. 265, p. 52–58, doi: 10.1016/j.palaeo.2008.04.021.

Arenas, R., and Martínez Catalán, J.R., 2002, Prograde development of corona textures in metagabbros of the Sobrado unit (Ordenes Complex, northwestern Iberian Massif): Geological Society of America, v. Special Pa, p. 73–88.

Bard, J.P., 1983, Metamorphism of an obducted island arc: example of the Kohistan sequence (Pakistan) in the Himalayan collided range: Earth and Planetary Science Letters, v. 65, p. 133–144, doi: 10.1016/0012-821X(83)90195-4.

Bebout, G.E., and Penniston-Dorland, S.C., 2016, Fluid and mass transfer at subduction interfaces-The field metamorphic record: Lithos, v. 240-243, p. 228–258, doi: 10.1016/j.lithos.2015.10.007.

Bohlen, S.R., 1987, Pressure-Temperature-Time Paths and a Tectonic Model for the Evolution of Granulites: Journal of Geology, v. 95, p. 617–632.

Brown, E.H., 1996, High-pressure metamorphism caused by magma loading in Fiordland, New Zealand: Journal of Metamorphic Geology, v. 14, p. 441–452, doi: 10.1046/j.1525-1314.1996.06024.x.

Coleman, R., 1977, Emplacement and metamorphism of ophiolites: Rendiconti Società Italiana di Mineralogia e Paleontologia, v. 33, p. 161–190.

Connolly, J.A.D., 2009, The geodynamic equation of state: What and how: Geochemistry, Geophysics, Geosystems, v. 10, doi: 10.1029/2009GC002540.

Daczko, N.R., Clarke, G.L., and Klepeis, K.A., 2002, Kyanite-paragonite-bearing assemblages, northern Fiordland, New Zealand: Rapid cooling of the lower crustal root to a Cretaceous magmatic arc: Journal of Metamorphic Geology, v. 20, p. 887–902, doi: 10.1046/j.1525-1314.2002.00421.x.

Dewey, J.F., Hempton, M.R., Kidd, W.S.F., Şaroğlu, F., and Şengör, A.M.C., 1986, Shortening of continental lithosphere: the neotectonics of Eastern Anatolia - a young collision zone: Geological Society, London, Special Publications, v. 19, p. 1–36, doi: 10.1144/GSL.SP.1986.019.01.01.

Dhuime, B., Bosch, D., Garrido, C.J., Bodinier, J.L., Bruguier, O., Hussain, S.S., and Dawood, H., 2009, Geochemical architecture of the lower- to middle-crustal section of a Paleo-island arc (Kohistan Complex, Jijal-Kamila area, Northern Pakistan): Implications for the evolution of an oceanic subduction zone: Journal of Petrology, v. 50, p. 531–569, doi: 10.1093/petrology/egp010.

Diener, J.F.A., and Powell, R., 2012, Revised activity-composition models for clinopyroxene and amphibole: Journal of Metamorphic Geology, v. 30, p. 131–142, doi: 10.1111/j.1525-1314.2011.00959.x.

Dilek, Y., and Flower, M.F.J., 2003, Arc-trench rollback and forearc accretion: 2. A model template for ophiolites in Albania, Cyprus, and Oman: Geological Society, London, Special Publications, v. 218, p. 43–68, doi: 10.1144/GSL.SP.2003.218.01.04.

Ernst, W.G., 1973, Blueschist metamorphism and P-T regimes in active subduction zones: Tectonophysics, v. 17, p. 255–272.

Faccenda, M., 2014, Water in the slab: A trilogy: Tectonophysics, v. 614, p. 1–30, doi:

10.1016/j.tecto.2013.12.020.
El Fadili, S., and Demaiffe, D., 1999, Petrology of Eclogite and Granulite Nodules from the Mbuji Mayi Kimberlites (Kasai, Congo): Significance of Kyanite-Omphacite Intergrowths, *in* Gurney, J.J., Gurney, J.L., Pascoe, M.D., and Richardson, S.H. eds., Proceedings of the 7th International Kimberlite Conference, p. 205–213.
Flowers, R.M., Bowring, S.A., Tulloch, A.J., and Klepeis, K.A., 2005, Tempo of burial and exhumation within the deep roots of a magmatic arc, Fiordland, New Zealand: Geology, v. 33, p. 17–20, doi: 10.1130/G21010.1.
Garfunkel, Z., 1998, Constrains on the origin and history of the Eastern Mediterranean basin: Tectonophysics, v. 298, p. 5–35, doi: 10.1016/S0040-1951(98)00176-0.
Garfunkel, Z., and Derin, B., 1984, Permian-early Mesozoic tectonism and continental margin formation in Israel and its implications for the history of the Eastern Mediterranean: Geological Society, London, Special Publications, v. 17, p. 187–201, doi: 10.1144/GSL.SP.1984.017.01.12.
Genç, Ş.C., Yiğitbaş, E., and Yılmaz, Y., 1993, Geology of the Berit metaophiolite, *in* A. Suat Erk Geology Symposium, Expanded Abstracts, p. 37–52.
Goergen, E.T., and Whitney, D.L., 2012, Long length scales of element transport during reaction texture development in orthoamphibole-cordierite gneiss: Thor-Odin dome, British Columbia, Canada: Contributions to Mineralogy and Petrology, v. 163, p. 337–352, doi: 10.1007/s00410-011-0671-y.
Griffin, W., 1971, Mineral reactions at a peridotite-gneiss contact, Jotunheimen, Norway: Mineralogical Magazine, v. 38, p. 435–445.
Griffin, W., Carswell, D., and Nixon, P., 1979, Lower crustal granulites and eclogites from Lesotho, Southern Africa, *in* Boyd, F. and Meyer, H. eds., Proceedings of the Second International Kimberlite Conference, Washington, D.C., American Geophysical Union.
Hacker, B.R., 1991, The role of deformation in the formation of metamorphic gradients: Ridge subduction beneath the Oman Ophiolite: Tectonics, v. 10, p. 455–473, doi: 10.1029/90TC02779.
Hacker, B.R., and Gnos, E., 1997, The conundrum of Samail: explaining the metamorphic history: Tectonophysics, v. 279, p. 215–226.
Hacker, B.R., Mosenfelder, J., and Gnos, E., 1996, Rapid emplacement of the Oman ophiolite: Thermal and geochronologic constraints: Tectonics, v. 15, p. 1230–1247, doi: 10.1029/96TC01973.
Haifler, J., and Kotková, J., 2016, UHP–UHT peak conditions and near-adiabatic exhumation path of diamond-bearing garnet–clinopyroxene rocks from the Eger Crystalline Complex, North Bohemian Massif: Lithos, v. 251, p. 366–381, doi: 10.1016/j.lithos.2016.02.001.
Harley, S.L., 1989, The origins of granulites: a metamorphic perspective: Geological Magazine, v. 126, p. 215–247, doi: 10.1017/S0016756800022330.
Holland, T.J.B., and Blundy, J., 1994, Non-ideal interactions in calcic amphiboles and their bearing on amphibole-plagioclase thermometry: Contributions to Mineralogy and Petrology, v. 116, p. 433–447, doi: 10.1007/BF00310910.
Holland, T.J.B., and Powell, R., 1998, An internally consistent thermodynamic data set for phases of petrological interest: Journal of Metamorphic Geology, v. 16, p. 309–343, doi: 10.1111/j.1525-1314.1998.00140.x.

Indares, A., 1993, Eclogitized gabbros from the eastern Grenville Province: textures, metamorphic context, and implications: Canadian Journal of Earth Science, v. 30, p. 159–173.
Indares, A., and Rivers, T., 1995, Textures, metamorphic reactions and thermobarometry of eclogitized metagabbros: a Proterozoic example: European Journal of Mineralogy, v. 7, p. 43–56.
Jamieson, R.A., 1986, P-T paths from high temperature shear zones beneath ophiolites: Journal of metamorphic Geology, v. 4, p. 3–22, doi: 10.1111/j.1525-1314.1986.tb00335.x.
Jolivet, L., and Faccenna, C., 2000, Mediterranean extension and the Africa-Eurasia collision: Tectonics, v. 19, p. 1095–1106, doi: 10.1029/2000TC900018.
Karaoğlan, F., 2012, The geochronology of the ophiolitic and the granitic rocks along the southeast Anatolian orogenic belt: University of Cukurova, doi: 10.1017/CBO9781107415324.004.
Karaoğlan, F., Parlak, O., Hejl, E., Neubauer, F., and Klötzli, U., 2016, The temporal evolution of the active margin along the Southeast Anatolian Orogenic Belt (SE Turkey): Evidence from U–Pb, Ar–Ar and fission track chronology: Gondwana Research, doi: 10.1016/j.gr.2015.12.011.
Karaoğlan, F., Parlak, O., Klötzli, U., Koller, F., and Rızaoğlu, T., 2013, Age and duration of intra-oceanic arc volcanism built on a suprasubduction zone type oceanic crust in southern Neotethys, SE Anatolia: Geoscience Frontiers, v. 4, p. 399–408, doi: 10.1016/j.gsf.2012.11.011.
Karaoğlan, F., Parlak, O., Robertson, A.H.F., Thöni, M., Klötzli, U., Koller, F., and Okay, A.I., 2013, Evidence of Eocene high-temperature/high-pressure metamorphism of ophiolitic rocks and granitoid intrusion related to Neotethyan subduction processes (Dogansehir area, SE Anatolia): Geological Society, London, Special Publications, v. 372, p. 249–272, doi: 10.1144/SP372.21.
Kaymakçı, N., Inceöz, M., Ertepinar, P., and Koç, A., 2010, Late Cretaceous to Recent kinematics of SE Anatolia (Turkey): Geological Society, London, Special Publications, v. 340, p. 409–435, doi: 10.1144/SP340.18.
Klepeis, K. a., Clarke, G.L., Gehrels, G., and Vervoort, J.D., 2004, Processes controlling vertical coupling and decoupling between the upper and lower crust of orogens: Results from Fiordland, New Zealand: Journal of Structural Geology, v. 26, p. 765–791, doi: 10.1016/j.jsg.2003.08.012.
Koç, A., and Kaymakçı, N., 2013, Kinematics of Sürgü Fault Zone (Malatya, Turkey): A remote sensing study: Journal of Geodynamics, v. 65, p. 292–307, doi: 10.1016/j.jog.2012.08.001.
Le Maitre, R., Bateman, P., Dudek, A., Keller, J., Lameyre, J., Le Bas, M., Sabine, P., Schmid, R., Sorensen, H., Streckeisen, A., and A, W., 1989, A Classification of Igneous Rocks and Glossary of Terms, Recommendations of the International Union of Geological Sciences, Subcomission on the Systematics of Igneous Rocks: Oxford, Blackwell, 193 p.
McQuarrie, N., 2003, Cenozoic evolution of Neotethys and implications for the causes of plate motions: Geophysical Research Letters, v. 30, p. 30–33, doi: 10.1029/2003GL017992.
McQuarrie, N., and Van Hinsbergen, D.J.J., 2013, Retrodeforming the Arabia-Eurasia

collision zone: Age of collision versus magnitude of continental subduction: Geology, v. 41, p. 315–318, doi: 10.1130/G33591.1.
Middlemost, E.A.K., 1994, Naming Materials in the Magma Igneous Rock System: Earth-Science Reviews, v. 37, p. 215–224, doi: 10.1016/0012-8252(94)90029-9.
Miyashiro, A., 1961, Evolution of metamorphic belts: Journal of Petrology, v. 2, p. 277–311, doi: 10.1093/petrology/2.3.277.
Molina, J.F., Moreno, J.A., Castro, A., Rodriguez, C., and Fershtater, G.B., 2015, Calcic amphibole thermobarometry in metamorphic and igneous rocks: New calibrations based on plagioclase/amphibole Al-Si partitioning and amphibole/liquid Mg partitioning: Lithos, v. 232, p. 286–305, doi: 10.1016/j.lithos.2015.06.027.
Molnar, P., and Tapponnier, P., 1975, Cenozoic tectonics of Asia: effects of a continental collision: Science, v. 189, p. 419–426.
Mullen, E.D., 1983, MnO-TiO2/P2O5: a method of discriminating between oceanic and non oceanic basalts: Earth and Planetary Science Letters, v. 24.
Newton, R.C., Charlu, T. V., and Kleppa, O.J., 1980, Thermochemistry of the high structural state plagioclases: Geochimica et Cosmochimica Acta, v. 44, p. 933–941, doi: 10.1016/0016-7037(80)90283-5.
O'Brien, P.J., and Rötzler, J., 2003, High-pressure granulites: Formation, recovery of peak conditions and implications for tectonics: Journal of Metamorphic Geology, v. 21, p. 3–20, doi: 10.1046/j.1525-1314.2003.00420.x.
Okay, A.I., 1980, Mineralogy, petrology, and phase relations of glaucophane-lawsonite zone blueschists from the Tavşanli Region, Northwest Turkey: Contributions to Mineralogy and Petrology, v. 72, p. 243–255, doi: 10.1007/BF00376143.
Parlak, O., 2006, Geodynamic significance of granitoid magmatism in the southeast Anatolian orogen: Geochemical and geochronogical evidence from Goksun-Afsin (Kahramanmaras, Turkey) region: International Journal of Earth Sciences, v. 95, p. 609–627, doi: 10.1007/s00531-005-0058-2.
Parlak, O., Höck, V., Kozlu, H., and Delaloye, M., 2004, Oceanic crust generation in an island arc tectonic setting, SE Anatolian orogenic belt (Turkey): Geological Magazine, v. 141, p. 583–603, doi: 10.1017/S0016756804009458.
Parlak, O., Karaoğlan, F., Rızaoğlu, T., Nurlu, N., Bağci, U., Höck, V., Önal, A.O., Kürüm, S., and Topak, Y., 2012, Petrology of the Ispendere (Malatya) ophiolite from the Southeast Anatolia: implications for the Late Mesozoic evolution of the southern Neotethyan Ocean: Geological Society, London, Special Publications, v. 372, p. 219–247, doi: 10.1144/SP372.11.
Parlak, O., Rızaoğlu, T., Bağci, U., Karaoğlan, F., and Höck, V., 2009, Tectonic significance of the geochemistry and petrology of ophiolites in southeast Anatolia, Turkey: Tectonophysics, v. 473, p. 173–187, doi: 10.1016/j.tecto.2008.08.002.
Passchier, C.W., and Trouw, R.A.J., 2005, Microtectonics: Berlin, Springer.
Peacock, S.M., 2003, Thermal Structure and Metamorphic Evolution of Subducting Slabs: Geophysical Monograph 138, p. 7–22, doi: 10.1029/138GM02.
Perchuk, A., and Philippot, P., 1997, Rapid cooling and exhumation of eclogitic rocks from the Great Caucasus, Russia: Journal of Metamorphic Geology, v. 15, p. 299–310, doi: 10.1111/j.1525-1314.1997.00022.x.
Perinçek, D., and Kozlu, H., 1984, Stratigraphy and structural relations of the units in the Afsin-Elbistan-Doganşehir region (Eastern Taurus), *in* Geology of the Taurus Belt,

International Symposium, p. 181–198.
Petterson, M.G., 2010, A Review of the geology and tectonics of the Kohistan island arc, north Pakistan: Geological Society, London, Special Publications, v. 338, p. 287–327, doi: 10.1144/SP338.14.
Le Pichon, X., 1995, Geodetic determination of the kinematics of central Greece with respect to Europe: Implications for eastern Mediterranean tectonics: Journal of Geophysical Research, v. 100, p. 12675–12690, doi: 10.1029/95JB00317.
Powell, R., and Holland, T.J.B., 1999, Relating formulations of the thermodynamics of mineral solid solutions: Activity modeling of pyroxenes, amphiboles, and micas: American Mineralogist, v. 84, p. 1–14.
Robertson, A.H.F., 2006, Contrasting modes of ophiolite emplacement in the Eastern Mediterranean region: Journal of the Geological Society, v. 32, p. 235–261, doi: 10.1144/GSL.MEM.2006.032.01.14.
Robertson, A.H.F., Parlak, O., Rızaoğlu, T., Ünlügenç, Ü., İnan, N., Taşlı, K., and Ustaömer, T., 2007, Tectonic evolution of the South Tethyan ocean: evidence from the Eastern Taurus Mountains (Elazig region, SE Turkey): Geological Society, London, Special Publications, v. 272, p. 231–270, doi: 10.1144/GSL.SP.2007.272.01.14.
Robertson, A.H.F., Ustaömer, T., Parlak, O., Ünlügenç, Ü., Taşlı, K., and İnan, N., 2006, The Berit transect of the Tauride thrust belt, S Turkey: Late Cretaceous–Early Cenozoic accretionary/collisional processes related to closure of the Southern Neotethys: Journal of Asian Earth Sciences, v. 27, p. 108–145, doi: 10.1016/j.jseaes.2005.02.004.
Şengör, A.M.C., Görür, N., and Şaroğlu, F., 1985, Strike-slip faulting and related basin formation in zones of tectonic escape: Turkey as a case study: Special Publication - The Society of Economic Paleontologists and Mineralogists, v. 37, p. 227–264.
Şengör, A.M.C., and Yılmaz, Y., 1981, Tethyan evolution of Turkey: A plate tectonic approach: Tectonophysics, v. 75, doi: 10.1016/0040-1951(81)90275-4.
Shervais, J.W., 1982, TiV plots and the petrogenesis of modern and ophiolitic lavas: Earth and Planetary Science Letters, v. 59, p. 101–118, doi: 10.1016/0012-821X(82)90120-0.
Tinkham, D.K., and Ghent, E.D., 2005, Estimating P-T conditions of garnet growth with isochemical phase-diagram sections and the problem of effective bulk-composition: Canadian Mineralogist, v. 43, p. 35–50, doi: 10.2113/gscanmin.43.1.35.
Wakabayashi, J., 1990, Counterclockwise P-T-t Paths from Amphibolites, Franciscan Complex, California: Relics from the Early Stages of Subduction Zone Metamorphism: The Journal of Geology, v. 98, p. 657–680, doi: 10.1086/629432.
Wakabayashi, J., and Dilek, Y., 2003, What constitutes “emplacement” of an ophiolite?: Mechanisms and relationship to subduction initiation and formation of metamorphic soles: Geological Society, London, Special Publications, v. 218, p. 427–447, doi: 10.1144/GSL.SP.2003.218.01.22.
Whitney, D.L., and Evans, B.W., 2010, Abbreviations for names of rock-forming minerals: American Mineralogist, v. 95, p. 185–187, doi: 10.2138/am.2010.3371.
Yamamoto, H., 1993, Contrasting metamorphic P – T – time paths of the Kohistan granulites and tectonics of the western Himalayas: Journal of the Geological Society, v. 150, p. 843–856, doi: 10.1144/gsjgs.150.5.0843.

Yamamoto, H., and Yoshino, T., 1998, Superposition of replacements in the mafic granulites of the Jijal complex of the Kohistan Arc, northern Pakistan: dehydration and rehydration within deep arc crust: Lithos, v. 43, p. 219–234, doi: 10.1016/S0024-4937(98)00014-0.

Yiğitbaş, E., and Yılmaz, Y., 1996, New evidence and solution to the Maden complex controversy of the Southeast Anatolian orogenic belt (Turkey): Geologische Rundschau, v. 85, p. 250–263, doi: 10.1007/BF02422232.

Yılmaz, Y., 1993, New evidence and model on the evolution of the southeast Anatolian orogen: Geological Society of America Bulletin, v. 105, p. 251–271, doi: 10.1130/0016-7606(1993)105<0251:NEAMOT>2.3.CO;2.

Yılmaz, Y., Yiğitbaş, E., and Genç, Ş.C., 1993, Ophiolitic and metamorphic assemblages of southeast Anatolia and their significance in the geological evolution of the orogenic belt: Tectonics, v. 12, p. 1280–1297.

Appendix 1 – Samples

Sample	Easting	Northing	Rock Type	Foliation	Lineation	Amp	Bt	Chl	Cpx	Crn	Ep gp.	Grt	Kfs	Ky	Mag	Ol	Opx	Pl	Qz	Rt	Spr	Srp	Spl	Ttn	Zrn	Notes
CAT13-25A	404649	4209556	grt-cpx amphibolite			×		×	×		×	×						×	×							
CAT13-25B	404649	4209556	grt-cpx amphibolite			×		×	×			×						×	×	×						
CAT13-25C	404649	4209556	grt-cpx amphibolite			×		×			×	×						×	×	×						mylonite
CAT13-25D	404649	4209556	grt-cpx amphibolite			×		×	×		×	×						×	×	×						mylonite
CAT13-26A	404579	4209539	corona granulite			×			×			×					×	×								
CAT13-27C1	404536	4209586	corona granulite			×			×	×		×					×	×		×	×					
CAT13-27C2	404536	4209586	corona granulite			×			×	×		×					×	×		×			×			
25613A	403231	4211880	amphibolite			×				×	×							×	×							
25613B	403231	4211880	corona granulite			×			×	×		×					×	×		×	×		×			
25613C	403231	4211880	amphibolite			×				×	×							×	×							
25613D	403397	4211755	corona granulite			×			×	×		×					×	×					×			
25613E	403397	4211755	corona granulite	025/V		×			×									×	×							retrogressed pod rim
25613F	403339	4211740	corona granulite	162/60 NE		×			×	×		×					×	×		×						retrogressed pod rim
25613G	403339	4211740	corona granulite	078/70 N		×			×	×		×						×	×	×						retrogressed pod rim
25613H	403339	4211740	corona granulite	082/V		×			×	×		×					×	×		×						pod core
25613I	391658	4210695	corona granulite			×			×		×							×	×							retrogressed pod rim
25613J	391658	4210695	ky granulite	040/45 NW		×			×		×	×		×				×		×						retrogressed pod rim
25613K	391658	4210695	ky granulite	140/50 NE		×			×	×	×	×		×				×	×	×						pod core
25613M	391658	4210695	ky granulite			×			×	×	×	×		×				×		×						pod core
25613N	391650	4210656	ky granulite	090/40 N		×			×	×	×	×		×				×		×						pod core
25613O	391650	4210656	ky granulite			×			×		×	×		×				×		×						
25613P	391650	4210656	ky granulite			×			×	×	×	×		×				×								pod core
26613A	401907	4210877	grt-cpx granulite			×			×	×	×	×		×				×		×						
26613B	401907	4210877	grt-cpx amphibolite	170/15 E		×			×	×	×	×						×		×						
26613C	401907	4210877	grt-cpx amphibolite	020/40 W		×			×		×	×						×		×					×	
CAT15-01B	403181	4211019	corona granulite			×			×		×	×						×		×	×		×			
CAT15-01dw	403407	4211848	amphibolite			×		×		×										×						
CAT15-02	403375	4211576	corona granulite			×			×	×		×					×	×		×	×					
CAT15-03	401872	4210703	serpentinite	304/05 N											×	×						×				
CAT15-03dw	403371	4211582	corona granulite			×			×	×		×					×	×			×					
CAT15-04A	401654	4209409	amphibolite			×																				
CAT15-04B	401654	4209409	grt amphibolite			×						×								×						
CAT15-04C	401654	4209409	grt-cpx amphibolite			×		×	×		×	×						×	×	×						
CAT15-05	402530	4209024	corona granulite			×			×			×					×	×	×							
CAT15-05Adw	391711	4210378	grt-cpx granulite						×		×	×		×			×	×		×	×					
CAT15-05Bdw	391711	4210378	ky granulite			×			×	×	×			×						×						altered
CAT15-05Cdw	391711	4210378	grt-cpx granulite			×			×		×	×		×			×	×								
CAT15-05Edw	391711	4210378	grt-cpx granulite			×			×		×	×		×				×	×							altered
CAT15-06	391635	4210520	amphibolite	351/45 E		×		×			×															retrogressed pod rim
CAT15-06Bdw	392482	4210774	ky granulite			×			×		×	×		×												
CAT15-07	391681	4210500	amphibolite	215/56 NW		×				×	×								×							
CAT15-08B	391716	4210376	ky granulite			×		×	×		×	×		×					×	×						
CAT15-09A	391721	4210355	grt-cpx granulite	071/76 N		×		×	×	×		×		×			×	×		×	×					
CAT15-09B	391721	4210355	grt-cpx granulite	080/84 N		×		×	×	×		×		×			×	×		×	×					
CAT15-09C	391721	4210355	grt-cpx granulite	082/86 N		×			×	×	×	×		×				×		×						
CAT15-10	392482	4210776	ky granulite			×		×	×		×	×		×						×						retrogressed pod rim
CAT15-11	392483	4210827	ky granulite			×		×	×		×	×		×						×						
CAT15-12A	396478	4212281	grt amphibolite	062/46 N		×					×	×						×	×	×						
CAT15-12B	396478	4212281	grt amphibolite			×					×	×							×	×						
CAT15-12C	396478	4212281	amphibolite			×																				lens in metabasalt
CAT15-13	396041	4213083	granitoid	045/40 NW	15/235		×						×		×			×	×						×	
CAT15-14	396130	4213188	granitoid	185/40 W	20/235		×						×		×			×	×						×	
CAT15-15	396212	4210757	harzburgite	140/30 NE												×	×						×			

Sample	Easting	Northing	Rock Type	Foliation	Lineation	Amp	Bt	Chl	Cpx	Crn	Ep gp.	Grt	Kfs	Ky	Mag	Ol	Opx	Pl	Qz	Rt	Spr	Srp	Spl	Ttn	Zrn	Notes
CAT15-17B	401373	4209766	grt-cpx amphibolite			×			×		×	×						×	×					×		
CAT15-19A	391626	4210480	ky granulite			×			×		×	×		×				×								pod core
CAT15-19B	391626	4210480	amphibolite	151/78 W		×					×															retrogressed pod rim
CAT15-20	391629	4210483	ky granulite			×		×	×	×	×	×		×				×	×							
CAT15-21	391642	4210469	ky granulite			×			×		×	×		×						×						
CAT15-22	391673	4210493	amphibolite	355/40 W	15/315	×		×			×									×						
CAT15-23	391757	4210535	amphibolite	325/35 S	34/260	×					×							×		×				×		
CAT15-24.1	391653	4210376	ky granulite			×			×	×		×		×						×						
CAT15-25	392581	4210891	grt-cpx amphibolite			×		×	×		×	×						×		×				×		
CAT15-26A	392518	4210824	grt-cpx granulite			×			×	×	×	×		×				×		×	×					retrogressed pod rim
CAT15-26B	392518	4210824	grt-cpx granulite			×			×	×	×	×		×				×		×	×					pod core
CAT15-27	392147	4210478	amphibolite	084/11 SE	05/086	×					×							×								
CAT15-28	401743	4209693	grt-cpx amphibolite	005/45 W		×			×		×	×						×	×	×						
CAT15-29	403187	4211430	dunite													×							×			altered

Appendix 2 – Analytical Methods

Ninety-six samples of the Berit metaophiolite and Doğanşehir granitoid were collected from the Doğanşehir region of Turkey. Sixty-seven of these were made into thin sections for analysis. These include fifteen kyanite granulites, nine garnet-clinopyroxene granulites, fourteen corona granulites, eleven garnet-clinopyroxene amphibolites, eleven amphibolites, two garnet amphibolites, one dunite, one serpentinite, one harzburgite, and two samples of the Doğanşehir granitoid (Appendix 1).

Whole-rock analyses

Twenty-two samples were selected for whole-rock major-element analysis, from which a subset of fifteen samples was analyzed for whole-rock trace-element geochemistry (Table 2). Whole-rock analyses were determined by X-ray Fluorescence (XRF) at Macalester College using a Philips PW-2400 X-ray Fluorescence spectrometer with a Rh-anode, end window-ray tube, and Philips Super-Q software.

Samples were crushed using a Bico-Braun Chipmunk jaw crusher and separated into two aliquots using the cone and quarter method. Aliquots were ground to a fine powder (<75 μm) using a shatterbox with tungsten carbide (WC) and steel ring mills. Aliquots for major-element analysis were ground in the WC mill, while aliquots for trace-element analysis were ground in steel.

Major-element concentrations (SiO_2, TiO_2, Al_2O_3, Fe_2O_3, MnO, CaO, Na_2O, K_2O, and P_2O_5) were determined by XRF from fused lithium borate glass beads. Sample powders were dried at 105°C for two hours and then ignited at 1000°C for one hour. Loss on Ignition (LOI) values were calculated from the percent weight loss after ignition

relative to the dried sample powders. One gram of ignited sample powder was mixed with five grams of lithium tertraborate/metaborate (12:22) and 0.01 g of ammonium nitrate (NH_3NO_4). The mixture was homogenized by hand and then fused in platinum alloy (95% Pt, 5% Au) crucibles with two drops of 50% hydrobromic acid solution (HBr) using a Claisse® Fluxy. The fused samples were cast in 32 mm diameter platinum alloy molds which produced glass discs approximately 4 mm thick.

Trace-element concentrations (Sc, V, Cr, Co, Ni, Cu, Zn, Ga, Rb, Sr, Y, Zr, Nb, Ba, La, Ce, Nd, Sm, Yb, Hf, Ta, Pb, Th, and U) were determined from pressed powder pellets. Ten grams of sample powder were combined with 15-20 drops of 2% polyvinyl alcohol (PVA) and homogenized by hand. The mixture was then placed in a 40 mm diameter stainless steel die and formed into a 4 mm thick pellet by applying six tons of pressure in a manual press under vacuum for 60 seconds.

Mineral chemistry

Thirteen samples were analyzed for mineral chemistry (Appendix 3). Mineral compositions were determined using a JEOL JXA-8900 Electron Probe Microanalyzer with Probe for EPMA software at the University of Minnesota. Quantitative spot analyses were made by wavelength-dispersive spectrometry (WDS). Operating conditions for quantitative analyses were 15 keV accelerating voltage, 20 nA beam current, and 1-5 μm beam diameter (defocused for feldspar and amphibole analyses). On and off-peak counting times were 15-20 seconds for all elements. Natural mineral standards and the Armstrong/Love-Scott Phi-Rho-Z matrix correction routine were used. Standard intensities were corrected for deadtime and drift over time.

Appendix 3 – Representative electron microprobe analyses

Garnet analyses

Lithology	Corona granulite																				
Sample	CAT15-02										CAT15-27C1					CAT15-01B					
Location	Corona-I	Corona-C	Corona-O	Corona-O	Corona-I	Corona-C	Corona-I	Corona-C	Corona-C	Corona-O	Corona-I	Corona-C	Corona-O	Corona-C	Corona-O	Rim	Core	Rim	Core	Rim	Rim
SiO_2	41.82	41.23	41.11	41.79	42.47	42.13	42.16	42.40	42.01	42.40	40.61	40.54	40.78	41.19	41.13	41.53	41.45	41.16	40.91	40.91	41.42
TiO_2	0.02	0.02	0.00	0.01	0.02	0.04	0.01	0.02	0.03	0.02	0.02	0.00	0.00	0.01	0.02	0.01	0.01	0.00	0.03	0.02	0.02
Al_2O_3	23.90	24.13	23.60	23.72	23.66	23.69	23.35	23.39	23.20	23.57	24.52	24.37	24.30	24.26	24.46	24.59	24.87	24.59	24.75	24.52	25.42
Cr_2O_3	0.01	0.00	0.02	0.00	0.00	0.04	0.00	0.00	0.00	0.00	0.13	0.01	0.00	0.03	0.00	0.01	0.03	0.00	0.02	0.08	0.04
FeO	8.37	7.45	9.76	7.06	7.74	7.29	8.00	7.54	7.38	7.19	9.58	8.96	8.90	8.90	9.25	8.07	7.93	7.85	7.73	8.81	8.65
MnO	0.15	0.13	0.28	0.13	0.16	0.10	0.17	0.15	0.14	0.11	0.16	0.15	0.20	0.17	0.21	0.14	0.17	0.11	0.12	0.17	0.23
MgO	19.11	19.06	16.89	18.38	19.43	18.46	19.46	19.31	18.74	18.15	18.46	16.86	16.25	18.10	17.47	20.22	20.05	19.50	19.61	18.06	18.57
CaO	6.67	7.75	8.35	8.12	6.03	7.47	6.07	6.91	7.36	8.36	6.97	9.41	9.77	8.04	8.23	6.03	6.79	7.42	7.15	8.40	7.73
Na_2O	0.00	0.00	0.00	0.00	0.00	0.00	0.00	0.00	0.00	0.00	0.00	0.00	0.00	0.01	0.00	0.00	0.00	0.00	0.01	0.00	0.02
K_2O	0.00	0.00	0.00	0.00	0.00	0.01	0.00	0.00	0.00	0.01	0.00	0.00	0.01	0.00	0.00	0.00	0.02	0.02	0.00	0.00	0.01
Total	100.06	99.78	100.02	99.21	99.52	99.25	99.22	99.73	98.85	99.81	100.46	100.30	100.20	100.71	100.77	100.60	101.32	100.65	100.32	100.98	102.12
Si	2.97	2.94	2.96	2.99	3.02	3.01	3.01	3.01	3.02	3.02	2.90	2.91	2.93	2.93	2.93	2.93	2.91	2.91	2.90	2.91	2.90
Ti	0.00	0.00	0.00	0.00	0.00	0.00	0.00	0.00	0.00	0.00	0.00	0.00	0.00	0.00	0.00	0.00	0.00	0.00	0.00	0.00	0.00
Al	2.00	2.03	2.00	2.00	1.98	1.99	1.97	1.96	1.96	1.98	2.07	2.06	2.06	2.04	2.06	2.05	2.06	2.05	2.07	2.05	2.10
Fe^{3+}	0.07	0.13	0.10	0.02	0.00	0.00	0.01	0.02	0.01	0.00	0.18	0.16	0.11	0.14	0.12	0.14	0.18	0.18	0.18	0.18	0.14
Cr	0.00	0.00	0.00	0.00	0.00	0.00	0.00	0.00	0.00	0.00	0.01	0.00	0.00	0.00	0.00	0.00	0.00	0.00	0.00	0.00	0.00
Fe^{2+}	0.43	0.31	0.49	0.40	0.46	0.44	0.47	0.43	0.44	0.43	0.39	0.37	0.43	0.39	0.44	0.34	0.29	0.29	0.28	0.35	0.36
Mn	0.01	0.01	0.02	0.01	0.01	0.01	0.01	0.01	0.01	0.01	0.01	0.01	0.01	0.01	0.01	0.01	0.01	0.01	0.01	0.01	0.01
Mg	2.03	2.03	1.81	1.96	2.06	1.97	2.07	2.05	2.01	1.93	1.97	1.81	1.74	1.92	1.86	2.13	2.10	2.06	2.07	1.92	1.94
Ca	0.51	0.59	0.64	0.62	0.46	0.57	0.46	0.53	0.57	0.64	0.53	0.72	0.75	0.61	0.63	0.46	0.51	0.56	0.54	0.64	0.58
Na	0.00	0.00	0.00	0.00	0.00	0.00	0.00	0.00	0.00	0.00	0.00	0.00	0.00	0.00	0.00	0.00	0.00	0.00	0.00	0.00	0.00
K	0.00	0.00	0.00	0.00	0.00	0.00	0.00	0.00	0.00	0.00	0.00	0.00	0.00	0.00	0.00	0.00	0.00	0.00	0.00	0.00	0.00
X_{sps}	0.00	0.00	0.01	0.00	0.00	0.00	0.00	0.00	0.00	0.00	0.00	0.00	0.00	0.00	0.00	0.00	0.00	0.00	0.00	0.00	0.00
X_{prp}	0.68	0.69	0.61	0.66	0.69	0.66	0.69	0.68	0.66	0.64	0.68	0.62	0.59	0.66	0.63	0.73	0.72	0.71	0.71	0.66	0.67
X_{alm}	0.15	0.11	0.16	0.13	0.15	0.15	0.15	0.14	0.14	0.14	0.14	0.13	0.14	0.13	0.15	0.12	0.10	0.10	0.10	0.12	0.13
X_{grs}	0.17	0.20	0.22	0.21	0.15	0.19	0.15	0.17	0.19	0.21	0.18	0.25	0.26	0.21	0.21	0.16	0.18	0.19	0.19	0.22	0.20

Corona-C, corona core; Corona-I, corona inner rim; Corona-O, corona outer rim

Garnet analyses

Lithology	Garnet-clinopyroxene granulite																		
Sample	CAT15-09A												CAT15-06Bdw			CAT15-26Ba			
Location	Rim	Core	Core	Rim	Core	Core	Core	Rim	Rim	Core	Rim	Core	Core	Core	Core	Core	Rim	Core	Rim
SiO_2	40.62	41.21	41.35	40.97	41.88	42.27	41.86	40.53	40.90	41.66	40.77	41.52	40.50	40.23	40.39	41.64	41.70	41.51	41.75
TiO_2	0.00	0.00	0.00	0.00	0.00	0.00	0.00	0.02	0.01	0.00	0.00	0.02	0.02	0.03	0.06	0.01	0.00	0.00	0.00
Al_2O_3	24.33	24.57	24.69	24.19	24.07	24.22	24.25	24.34	24.53	25.01	24.31	24.71	23.52	23.46	22.58	23.85	23.86	24.31	23.78
Cr_2O_3	0.51	0.06	0.23	0.38	0.00	0.02	0.00	0.00	0.00	0.02	0.01	0.01	0.34	0.22	0.43	0.00	0.10	0.00	0.06
FeO	9.54	9.47	9.32	9.98	8.72	8.49	8.53	11.29	10.94	8.09	10.54	8.63	12.09	12.58	13.88	8.58	8.83	8.79	9.58
MnO	0.23	0.26	0.16	0.20	0.13	0.20	0.17	0.27	0.26	0.15	0.20	0.17	0.32	0.31	0.44	0.15	0.17	0.18	0.20
MgO	17.80	18.52	18.31	17.60	19.51	19.65	19.30	13.85	14.09	18.62	13.97	18.50	15.33	15.05	14.15	16.61	16.84	17.60	15.67
CaO	7.72	7.08	7.51	7.34	5.57	5.44	5.98	11.17	11.01	8.23	11.39	7.96	8.48	8.31	8.31	9.69	9.18	8.76	10.09
Na_2O	0.00	0.01	0.02	0.01	0.00	0.00	0.00	0.00	0.00	0.03	0.00	0.01	0.02	0.01	0.02	0.00	0.00	0.00	0.00
K_2O	0.01	0.00	0.02	0.02	0.00	0.00	0.00	0.00	0.02	0.01	0.00	0.01	0.01	0.00	0.00	0.00	0.02	0.01	0.00
Total	100.77	101.18	101.61	100.67	99.89	100.29	100.10	101.49	101.77	101.83	101.19	101.54	100.62	100.19	100.28	100.52	100.71	101.16	101.13
Si	2.90	2.92	2.92	2.93	2.98	2.99	2.97	2.92	2.93	2.92	2.94	2.93	2.94	2.94	2.97	2.98	2.98	2.95	2.98
Ti	0.00	0.00	0.00	0.00	0.00	0.00	0.00	0.00	0.00	0.00	0.00	0.00	0.00	0.00	0.00	0.00	0.00	0.00	0.00
Al	2.05	2.05	2.05	2.04	2.02	2.02	2.03	2.07	2.07	2.07	2.06	2.05	2.01	2.02	1.96	2.01	2.01	2.03	2.00
Fe^{3+}	0.17	0.15	0.14	0.12	0.04	0.01	0.04	0.13	0.09	0.14	0.09	0.14	0.14	0.14	0.12	0.06	0.06	0.12	0.04
Cr	0.03	0.00	0.01	0.02	0.00	0.00	0.00	0.00	0.00	0.00	0.00	0.00	0.02	0.01	0.03	0.00	0.01	0.00	0.00
Fe^{2+}	0.40	0.41	0.41	0.48	0.48	0.49	0.46	0.55	0.56	0.34	0.55	0.37	0.60	0.63	0.73	0.46	0.47	0.41	0.53
Mn	0.01	0.02	0.01	0.01	0.01	0.01	0.01	0.02	0.02	0.01	0.01	0.01	0.02	0.02	0.03	0.01	0.01	0.01	0.01
Mg	1.90	1.96	1.93	1.88	2.07	2.07	2.04	1.49	1.51	1.95	1.50	1.94	1.66	1.64	1.55	1.77	1.79	1.86	1.67
Ca	0.59	0.54	0.57	0.56	0.42	0.41	0.46	0.86	0.85	0.62	0.88	0.60	0.66	0.65	0.65	0.74	0.70	0.67	0.77
Na	0.00	0.00	0.00	0.00	0.00	0.00	0.00	0.00	0.00	0.00	0.00	0.00	0.00	0.00	0.00	0.00	0.00	0.00	0.00
K	0.00	0.00	0.00	0.00	0.00	0.00	0.00	0.00	0.00	0.00	0.00	0.00	0.00	0.00	0.00	0.00	0.00	0.00	0.00
X_{sps}	0.00	0.01	0.00	0.00	0.00	0.00	0.00	0.01	0.01	0.00	0.00	0.00	0.01	0.01	0.01	0.00	0.00	0.00	0.00
X_{prp}	0.65	0.67	0.66	0.64	0.69	0.69	0.69	0.51	0.51	0.67	0.51	0.67	0.57	0.56	0.52	0.59	0.60	0.63	0.56
X_{alm}	0.14	0.14	0.14	0.16	0.16	0.17	0.16	0.19	0.19	0.12	0.19	0.13	0.20	0.21	0.25	0.15	0.16	0.14	0.18
X_{grs}	0.20	0.18	0.20	0.19	0.14	0.14	0.15	0.30	0.29	0.21	0.30	0.21	0.22	0.22	0.22	0.25	0.24	0.23	0.26

Garnet analyses

Lithology	Kyanite granulite																									
Sample	CAT15-20										CAT15-24									25613K						
Location	Rim	Core	Rim	Core	Rim	Rim	Core	Rim	Core	Rim	Core	Rim	Core	Rim	Rim	Core	Rim	Core	Core	Core	Rim	Core	Rim	Core	Rim	Rim
SiO_2	40.80	41.81	41.27	41.88	41.44	40.93	41.58	41.37	41.65	40.81	41.29	40.76	41.21	41.01	40.84	41.32	41.51	41.03	41.03	40.80	40.52	40.24	40.32	41.41	40.72	41.28
TiO_2	0.00	0.03	0.03	0.05	0.05	0.02	0.00	0.03	0.02	0.00	0.00	0.02	0.00	0.00	0.03	0.02	0.00	0.00	0.01	0.03	0.02	0.05	0.01	0.03	0.00	0.03
Al_2O_3	23.18	23.65	23.37	23.41	23.39	23.42	23.76	23.20	23.68	23.03	23.24	22.88	23.27	22.97	23.07	23.17	23.09	22.84	24.24	23.98	23.43	23.57	23.15	23.38	23.24	23.61
Cr_2O_3	0.12	0.20	0.12	0.12	0.07	0.11	0.03	0.16	0.04	0.27	0.32	0.38	0.23	0.43	0.25	0.36	0.41	0.37	0.49	0.04	0.14	0.18	0.19	0.08	0.23	0.06
FeO	14.79	10.71	14.15	10.90	12.75	14.23	11.56	13.58	11.65	13.86	11.27	11.97	10.45	11.43	10.96	9.92	10.42	9.93	10.00	14.68	11.95	12.72	14.29	13.41	13.03	12.69
MnO	0.53	0.35	0.45	0.29	0.47	0.49	0.32	0.38	0.43	0.45	0.33	0.37	0.30	0.30	0.29	0.23	0.35	0.27	0.28	0.55	0.26	0.35	0.36	0.48	0.24	0.26
MgO	13.49	17.19	14.69	16.87	15.33	14.21	16.72	15.41	16.41	12.83	16.28	15.16	16.80	15.82	16.02	17.06	17.15	16.54	17.47	14.31	14.67	15.77	14.63	15.27	13.85	14.53
CaO	8.39	6.91	7.34	7.19	7.18	7.73	7.32	6.91	6.93	10.07	7.81	8.14	7.40	7.75	7.74	7.88	7.18	7.84	7.63	7.53	9.29	7.96	7.65	7.56	9.45	9.08
Na_2O	0.01	0.02	0.01	0.01	0.00	0.01	0.00	0.01	0.01	0.01	0.00	0.01	0.00	0.00	0.00	0.00	0.00	0.02	0.02	0.00	0.01	0.02	0.00	0.02	0.01	0.00
K_2O	0.00	0.00	0.00	0.01	0.00	0.00	0.00	0.00	0.00	0.02	0.00	0.00	0.02	0.01	0.00	0.00	0.02	0.00	0.00	0.00	0.02	0.02	0.01	0.01	0.00	0.00
Total	101.32	100.87	101.41	100.72	100.67	101.14	101.30	101.04	100.82	101.36	100.53	99.69	99.68	99.72	99.21	99.97	100.12	98.83	101.18	101.91	100.29	100.89	100.61	101.65	100.76	101.55
Si	2.97	2.99	2.98	3.00	3.00	2.97	2.97	2.99	2.99	2.98	2.98	2.98	2.98	2.99	2.98	2.98	2.99	2.99	2.92	2.95	2.95	2.92	2.95	2.98	2.97	2.97
Ti	0.00	0.00	0.00	0.00	0.00	0.00	0.00	0.00	0.00	0.00	0.00	0.00	0.00	0.00	0.00	0.00	0.00	0.00	0.00	0.00	0.00	0.00	0.00	0.00	0.00	0.00
Al	1.99	1.99	1.99	1.98	1.99	2.00	2.00	1.98	2.00	1.98	1.98	1.97	1.98	1.97	1.98	1.97	1.96	1.96	2.04	2.04	2.01	2.02	2.00	1.98	2.00	2.00
Fe^{3+}	0.08	0.04	0.05	0.03	0.01	0.06	0.08	0.05	0.03	0.09	0.08	0.07	0.06	0.05	0.06	0.07	0.06	0.05	0.13	0.09	0.11	0.20	0.14	0.08	0.09	0.07
Cr	0.01	0.01	0.01	0.01	0.00	0.01	0.00	0.01	0.00	0.02	0.02	0.02	0.01	0.02	0.01	0.02	0.02	0.02	0.03	0.00	0.01	0.01	0.01	0.00	0.01	0.00
Fe^{2+}	0.82	0.60	0.80	0.63	0.76	0.80	0.61	0.77	0.67	0.76	0.60	0.67	0.57	0.64	0.61	0.52	0.57	0.56	0.46	0.79	0.61	0.57	0.73	0.72	0.71	0.70
Mn	0.03	0.02	0.03	0.02	0.03	0.03	0.02	0.02	0.03	0.03	0.02	0.02	0.02	0.02	0.02	0.01	0.02	0.02	0.02	0.03	0.02	0.02	0.02	0.03	0.01	0.02
Mg	1.47	1.83	1.58	1.80	1.65	1.54	1.78	1.66	1.76	1.39	1.75	1.65	1.81	1.72	1.74	1.83	1.84	1.80	1.86	1.54	1.59	1.70	1.59	1.64	1.50	1.56
Ca	0.66	0.53	0.57	0.55	0.56	0.60	0.56	0.54	0.53	0.79	0.60	0.64	0.57	0.60	0.61	0.61	0.55	0.61	0.58	0.58	0.73	0.62	0.60	0.58	0.74	0.70
Na	0.00	0.00	0.00	0.00	0.00	0.00	0.00	0.00	0.00	0.00	0.00	0.00	0.00	0.00	0.00	0.00	0.00	0.00	0.00	0.00	0.00	0.00	0.00	0.00	0.00	0.00
K	0.00	0.00	0.00	0.00	0.00	0.00	0.00	0.00	0.00	0.00	0.00	0.00	0.00	0.00	0.00	0.00	0.00	0.00	0.00	0.00	0.00	0.00	0.00	0.00	0.00	0.00
X_{sps}	0.01	0.01	0.01	0.01	0.01	0.01	0.01	0.01	0.01	0.01	0.01	0.01	0.01	0.01	0.01	0.00	0.01	0.01	0.01	0.01	0.01	0.01	0.01	0.01	0.00	0.01
X_{prp}	0.49	0.61	0.53	0.60	0.55	0.52	0.60	0.56	0.59	0.47	0.59	0.55	0.61	0.58	0.58	0.62	0.62	0.60	0.64	0.52	0.54	0.59	0.54	0.55	0.51	0.52
X_{alm}	0.27	0.20	0.27	0.21	0.25	0.27	0.21	0.26	0.22	0.26	0.20	0.22	0.19	0.22	0.21	0.18	0.19	0.19	0.16	0.27	0.21	0.20	0.25	0.24	0.24	0.23
X_{grs}	0.22	0.18	0.19	0.18	0.19	0.20	0.19	0.18	0.18	0.27	0.20	0.21	0.19	0.20	0.20	0.20	0.19	0.21	0.20	0.20	0.25	0.21	0.20	0.20	0.25	0.24

Garnet analyses

Lithology	Garnet-clinopyroxene amphibolite									
Sample	CAT15-17B							CAT15-28		
Location	Rim	Mantle	Core	Mantle	Rim	Core	Rim	Core	Core	Core
SiO_2	38.55	38.64	38.38	38.26	38.69	38.48	38.57	38.12	37.88	38.96
TiO_2	0.07	0.09	0.11	0.07	0.01	0.09	0.28	0.08	0.04	0.04
Al_2O_3	22.29	21.98	22.01	21.85	22.12	21.86	21.70	22.26	22.44	22.46
Cr_2O_3	0.10	0.07	0.06	0.04	0.13	0.03	0.01	0.04	0.01	0.07
FeO	20.02	20.11	19.87	20.44	19.97	20.59	20.55	20.20	19.98	19.92
MnO	0.49	0.54	0.55	1.28	0.46	1.70	1.65	1.62	1.59	1.19
MgO	8.18	7.86	7.68	6.86	7.92	6.37	6.31	6.73	6.63	7.39
CaO	10.96	11.29	11.47	11.65	10.96	11.44	11.52	11.44	11.38	10.90
Na_2O	0.02	0.02	0.01	0.01	0.00	0.03	0.04	0.04	0.01	0.00
K_2O	0.00	0.00	0.00	0.01	0.01	0.01	0.02	0.00	0.01	0.00
Total	100.69	100.59	100.13	100.47	100.27	100.60	100.64	100.53	99.96	100.93
Si	2.93	2.95	2.94	2.94	2.95	2.96	2.96	2.93	2.92	2.96
Ti	0.00	0.01	0.01	0.00	0.00	0.01	0.02	0.00	0.00	0.00
Al	2.00	1.97	1.99	1.98	1.99	1.98	1.96	2.01	2.04	2.01
Fe^{3+}	0.20	0.18	0.18	0.20	0.15	0.15	0.13	0.19	0.17	0.10
Cr	0.01	0.00	0.00	0.00	0.01	0.00	0.00	0.00	0.00	0.00
Fe^{2+}	1.08	1.10	1.09	1.11	1.12	1.17	1.19	1.10	1.11	1.16
Mn	0.03	0.04	0.04	0.08	0.03	0.11	0.11	0.11	0.10	0.08
Mg	0.93	0.89	0.88	0.79	0.90	0.73	0.72	0.77	0.76	0.84
Ca	0.89	0.92	0.94	0.96	0.90	0.94	0.95	0.94	0.94	0.89
Na	0.00	0.00	0.00	0.00	0.00	0.00	0.01	0.01	0.00	0.00
K	0.00	0.00	0.00	0.00	0.00	0.00	0.00	0.00	0.00	0.00
X_{sps}	0.01	0.01	0.01	0.03	0.01	0.04	0.04	0.04	0.04	0.03
X_{prp}	0.32	0.30	0.30	0.27	0.31	0.25	0.24	0.26	0.26	0.28
X_{alm}	0.37	0.37	0.37	0.38	0.38	0.40	0.40	0.38	0.38	0.39
X_{grs}	0.30	0.31	0.32	0.33	0.30	0.32	0.32	0.32	0.32	0.30

Clinopyroxene analyses

Lithology	Corona granulite																													
Sample	CAT15-02									CAT13-27C1													CAT15-01B							
Location	Corona-I	Corona-O	Corona-C	Corona-O	Corona-C	Corona-I	Sympl	Sympl	Sympl	Rim	Core	Rim	Core	Core	Incl	Incl	Corona-C	Corona-I	Corona-C	Corona-O	Sympl	Rim	Core	Core	Core	Core	Rim	Rim	Rim
SiO_2	52.65	52.52	51.66	51.23	52.65	53.96	51.28	51.34	50.45	48.72	51.84	48.26	51.40	52.65	52.43	50.62	52.38	52.54	49.91	52.12	48.37	50.34	52.19	51.47	52.57	51.87	50.75	50.75	49.59
TiO_2	0.02	0.01	0.04	0.05	0.00	0.03	0.06	0.02	0.01	0.28	0.18	0.25	0.08	0.26	0.22	0.41	0.16	0.11	0.12	0.11	0.19	0.36	0.26	0.34	0.28	0.09	0.15	0.17	0.28
Al_2O_3	5.45	6.13	6.78	7.40	5.56	3.30	8.67	9.27	9.22	9.03	3.16	8.65	4.99	3.09	3.23	5.99	4.25	4.31	4.66	4.99	9.21	8.73	3.63	3.64	3.66	6.61	8.39	9.27	11.28
Cr_2O_3	0.00	0.00	0.12	0.20	0.04	0.04	0.00	0.03	0.00	0.50	0.59	0.32	0.63	0.60	0.00	0.00	0.10	0.13	0.23	0.11	0.04	0.72	1.18	1.16	1.29	0.07	0.00	0.05	0.12
FeO	1.51	1.40	1.30	1.48	1.59	1.23	1.37	1.31	1.28	1.68	1.99	1.84	1.81	2.50	2.07	3.33	1.97	2.27	2.10	1.96	1.63	1.56	1.91	2.00	1.88	1.81	1.54	1.23	1.38
MnO	0.00	0.02	0.05	0.00	0.02	0.00	0.00	0.00	0.03	0.03	0.04	0.05	0.02	0.08	0.05	0.10	0.03	0.04	0.01	0.04	0.02	0.04	0.04	0.05	0.00	0.02	0.02	0.00	0.00
MgO	15.97	15.62	14.76	14.66	15.51	16.56	14.79	13.78	13.48	13.98	16.55	14.33	15.48	16.38	16.66	14.69	16.27	16.34	16.30	16.03	14.29	14.17	16.14	16.33	16.22	15.64	14.60	14.12	13.03
CaO	23.08	23.23	23.57	23.54	23.21	24.35	23.84	23.19	23.58	24.32	24.44	23.94	23.83	23.64	24.84	24.46	23.47	23.31	23.15	23.65	23.67	22.29	23.13	22.84	22.86	22.63	22.71	22.77	22.81
Na_2O	0.98	1.04	1.00	0.96	0.99	0.73	0.95	1.16	1.09	0.65	0.63	0.77	0.76	0.80	0.46	0.51	0.75	0.82	0.76	0.77	0.81	1.50	1.06	1.08	1.19	1.26	1.54	1.49	1.50
K_2O	0.00	0.00	0.00	0.00	0.01	0.01	0.00	0.02	0.01	0.00	0.00	0.01	0.00	0.02	0.00	0.00	0.00	0.00	0.02	0.00	0.01	0.00	0.00	0.00	0.00	0.02	0.02	0.00	0.01
Total	99.66	99.97	99.29	99.52	99.57	100.21	100.97	100.13	99.15	99.20	99.42	98.41	99.00	100.01	99.96	100.11	99.39	99.87	97.26	99.78	98.25	99.70	99.55	98.91	99.95	100.01	99.72	99.85	100.00
Si	1.90	1.89	1.88	1.86	1.91	1.94	1.83	1.85	1.84	1.78	1.89	1.77	1.88	1.91	1.90	1.84	1.90	1.90	1.85	1.89	1.77	1.82	1.90	1.88	1.90	1.86	1.83	1.83	1.78
Ti	0.00	0.00	0.00	0.00	0.00	0.00	0.00	0.00	0.00	0.01	0.00	0.01	0.00	0.01	0.01	0.01	0.00	0.00	0.00	0.00	0.01	0.01	0.01	0.01	0.01	0.00	0.00	0.00	0.01
Al^{iv}	0.10	0.11	0.12	0.14	0.09	0.06	0.17	0.15	0.16	0.22	0.11	0.23	0.12	0.09	0.10	0.16	0.10	0.10	0.15	0.11	0.23	0.18	0.10	0.12	0.10	0.14	0.17	0.17	0.22
Al^{vi}	0.13	0.15	0.17	0.17	0.14	0.08	0.19	0.24	0.23	0.17	0.02	0.15	0.09	0.04	0.04	0.10	0.08	0.08	0.05	0.10	0.17	0.19	0.05	0.04	0.06	0.14	0.18	0.22	0.26
Fe^{3+}	0.03	0.03	0.02	0.03	0.02	0.02	0.04	0.00	0.01	0.07	0.11	0.11	0.06	0.08	0.09	0.07	0.05	0.07	0.14	0.06	0.10	0.06	0.08	0.11	0.08	0.07	0.09	0.05	0.04
Cr	0.00	0.00	0.00	0.01	0.00	0.00	0.00	0.00	0.00	0.01	0.02	0.01	0.02	0.02	0.00	0.00	0.00	0.00	0.01	0.00	0.00	0.02	0.03	0.03	0.04	0.00	0.00	0.00	0.00
Fe^{2+}	0.01	0.01	0.02	0.02	0.03	0.01	0.00	0.04	0.03	0.00	0.00	0.00	0.00	0.00	0.00	0.03	0.01	0.00	0.00	0.00	0.00	0.00	0.00	0.00	0.00	0.00	0.00	0.00	0.00
Mn	0.00	0.00	0.00	0.00	0.00	0.00	0.00	0.00	0.00	0.00	0.00	0.00	0.00	0.00	0.00	0.00	0.00	0.00	0.00	0.00	0.00	0.00	0.00	0.00	0.00	0.00	0.00	0.00	0.00
Mg	0.86	0.84	0.80	0.79	0.84	0.89	0.79	0.74	0.73	0.76	0.90	0.78	0.84	0.88	0.90	0.80	0.88	0.88	0.90	0.86	0.78	0.76	0.87	0.89	0.87	0.84	0.78	0.76	0.70
Ca	0.89	0.90	0.92	0.91	0.90	0.94	0.91	0.89	0.92	0.95	0.95	0.94	0.93	0.92	0.96	0.95	0.91	0.90	0.92	0.92	0.93	0.86	0.90	0.89	0.89	0.87	0.88	0.88	0.88
Na	0.07	0.07	0.07	0.07	0.07	0.05	0.07	0.08	0.08	0.05	0.04	0.05	0.05	0.06	0.03	0.04	0.05	0.06	0.05	0.05	0.06	0.10	0.07	0.08	0.08	0.09	0.11	0.10	0.10
K	0.00	0.00	0.00	0.00	0.00	0.00	0.00	0.00	0.00	0.00	0.00	0.00	0.00	0.00	0.00	0.00	0.00	0.00	0.00	0.00	0.00	0.00	0.00	0.00	0.00	0.00	0.00	0.00	0.00
Wo	0.50	0.50	0.52	0.52	0.50	0.50	0.52	0.53	0.54	0.53	0.49	0.51	0.51	0.49	0.49	0.51	0.49	0.49	0.47	0.50	0.51	0.51	0.49	0.47	0.48	0.49	0.50	0.52	0.54
En	0.48	0.47	0.45	0.45	0.47	0.48	0.45	0.44	0.43	0.43	0.46	0.43	0.46	0.47	0.46	0.43	0.47	0.48	0.46	0.47	0.43	0.45	0.47	0.47	0.48	0.47	0.45	0.45	0.43
Fs	0.03	0.02	0.02	0.03	0.03	0.02	0.02	0.02	0.02	0.04	0.06	0.06	0.03	0.04	0.05	0.06	0.03	0.04	0.07	0.03	0.06	0.03	0.04	0.06	0.04	0.04	0.05	0.03	0.03
Quad	0.93	0.92	0.92	0.93	0.93	0.95	0.93	0.91	0.92	0.95	0.95	0.94	0.94	0.94	0.97	0.96	0.94	0.94	0.94	0.94	0.94	0.89	0.92	0.92	0.91	0.91	0.89	0.89	0.88
Jd	0.06	0.07	0.07	0.07	0.07	0.04	0.06	0.09	0.08	0.04	0.01	0.04	0.04	0.02	0.01	0.03	0.04	0.04	0.02	0.04	0.05	0.10	0.04	0.02	0.04	0.07	0.09	0.10	0.11
Ae	0.01	0.01	0.01	0.01	0.01	0.01	0.01	0.00	0.00	0.01	0.04	0.02	0.02	0.04	0.02	0.01	0.02	0.02	0.04	0.02	0.02	0.02	0.04	0.06	0.04	0.02	0.03	0.01	0.01

Sympl, symplectite; Corona-C, corona core; Corona-I, corona inner rim; Corona-O, corona outer rim

Clinopyroxene analyses

Lithology	Garnet-clinopyroxene granulite																				
Sample	CAT15-09A								CAT15-06Bdw						CAT15-26Ba						
Location	Core	Rim	Core	Sympl	Sympl	Sympl	Sympl	Sympl	Core	Core	Rim	Core	Core	Incl	Sympl	Sympl	Core	Rim	Sympl	Sympl	
SiO_2	51.77	51.84	53.72	52.22	51.33	52.10	52.02	51.79	50.85	50.69	50.74	51.63	51.20	51.27	50.93	52.60	51.21	51.05	51.85	51.10	
TiO_2	0.18	0.23	0.00	0.03	0.00	0.04	0.02	0.04	0.26	0.33	0.31	0.15	0.22	0.42	0.06	0.09	0.13	0.18	0.07	0.23	
Al_2O_3	5.79	7.11	3.69	9.85	9.56	9.83	8.61	10.27	8.02	8.63	8.12	7.59	7.39	6.70	11.23	8.87	8.93	10.50	9.36	12.18	
Cr_2O_3	1.10	0.42	0.07	0.03	0.01	0.00	0.00	0.01	0.37	0.63	0.43	0.20	0.20	0.36	0.00	0.03	1.00	0.20	0.84	0.45	
FeO	1.93	1.53	1.84	1.63	1.42	1.59	1.67	1.57	2.18	2.15	2.32	2.58	2.40	2.53	1.90	1.86	1.53	1.45	1.81	1.83	
MnO	0.00	0.01	0.00	0.02	0.00	0.02	0.02	0.04	0.00	0.01	0.04	0.00	0.00	0.00	0.00	0.04	0.02	0.02	0.01	0.07	
MgO	15.32	14.78	16.24	12.98	13.44	12.93	13.02	12.67	13.88	13.49	13.96	14.27	14.16	14.32	12.61	13.12	13.65	13.31	12.68	11.93	
CaO	22.26	22.36	23.18	21.08	22.77	21.66	21.75	22.27	22.75	22.42	22.78	22.72	22.74	22.76	22.27	21.33	22.73	22.32	21.31	20.98	
Na_2O	1.17	1.43	0.65	2.26	1.58	2.08	2.05	1.91	1.36	1.27	1.28	1.28	1.21	1.27	1.81	2.22	1.54	1.79	2.22	2.45	
K_2O	0.00	0.00	0.00	0.01	0.01	0.00	0.01	0.01	0.00	0.00	0.00	0.00	0.02	0.00	0.00	0.00	0.00	0.00	0.00	0.01	
Total	99.51	99.71	99.39	100.12	100.11	100.25	99.17	100.58	99.68	99.62	99.97	100.41	99.53	99.65	100.80	100.14	100.74	100.83	100.15	101.24	
Si	1.88	1.87	1.95	1.87	1.84	1.87	1.89	1.85	1.84	1.84	1.84	1.86	1.86	1.86	1.82	1.89	1.84	1.82	1.87	1.82	
Ti	0.00	0.01	0.00	0.00	0.00	0.00	0.00	0.00	0.01	0.01	0.01	0.00	0.01	0.01	0.00	0.00	0.00	0.00	0.00	0.01	
Al^{iv}	0.12	0.13	0.05	0.13	0.16	0.13	0.11	0.15	0.16	0.16	0.16	0.14	0.14	0.14	0.18	0.11	0.16	0.18	0.13	0.18	
Al^{vi}	0.13	0.17	0.11	0.29	0.25	0.28	0.25	0.29	0.19	0.21	0.18	0.18	0.18	0.15	0.29	0.26	0.21	0.26	0.26	0.33	
Fe^{3+}	0.03	0.03	0.00	0.00	0.02	0.00	0.00	0.00	0.04	0.00	0.04	0.04	0.03	0.04	0.01	0.00	0.02	0.03	0.00	0.00	
Cr	0.03	0.01	0.00	0.00	0.00	0.00	0.00	0.00	0.01	0.02	0.01	0.01	0.01	0.01	0.00	0.00	0.03	0.01	0.02	0.01	
Fe^{2+}	0.02	0.02	0.06	0.05	0.03	0.05	0.05	0.05	0.02	0.07	0.03	0.04	0.04	0.03	0.05	0.06	0.02	0.02	0.05	0.05	
Mn	0.00	0.00	0.00	0.00	0.00	0.00	0.00	0.00	0.00	0.00	0.00	0.00	0.00	0.00	0.00	0.00	0.00	0.00	0.00	0.00	
Mg	0.83	0.80	0.88	0.69	0.72	0.69	0.70	0.68	0.75	0.73	0.75	0.77	0.77	0.78	0.67	0.70	0.73	0.71	0.68	0.63	
Ca	0.87	0.87	0.90	0.81	0.88	0.83	0.85	0.85	0.88	0.87	0.88	0.88	0.89	0.89	0.85	0.82	0.87	0.85	0.82	0.80	
Na	0.08	0.10	0.05	0.16	0.11	0.14	0.14	0.13	0.10	0.09	0.09	0.09	0.09	0.09	0.13	0.15	0.11	0.12	0.16	0.17	
K	0.00	0.00	0.00	0.00	0.00	0.00	0.00	0.00	0.00	0.00	0.00	0.00	0.00	0.00	0.00	0.00	0.00	0.00	0.00	0.00	
Wo	0.49	0.51	0.49	0.52	0.53	0.53	0.53	0.54	0.52	0.52	0.52	0.51	0.51	0.51	0.54	0.52	0.53	0.53	0.53	0.54	
En	0.47	0.47	0.48	0.45	0.44	0.44	0.44	0.43	0.44	0.44	0.44	0.45	0.44	0.45	0.42	0.44	0.44	0.44	0.44	0.42	
Fs	0.03	0.03	0.03	0.03	0.03	0.03	0.03	0.03	0.04	0.04	0.04	0.05	0.04	0.04	0.04	0.04	0.03	0.03	0.04	0.04	
Quad	0.91	0.89	0.95	0.83	0.88	0.84	0.85	0.86	0.90	0.90	0.90	0.90	0.91	0.90	0.86	0.84	0.88	0.86	0.83	0.81	
Jd	0.08	0.10	0.05	0.17	0.12	0.16	0.15	0.14	0.09	0.10	0.09	0.09	0.08	0.08	0.13	0.16	0.11	0.13	0.17	0.18	
Ae	0.01	0.01	0.00	0.00	0.00	0.00	0.00	0.00	0.01	0.00	0.01	0.01	0.01	0.01	0.00	0.00	0.01	0.01	0.00	0.00	

Clinopyroxene analyses

Lithology	Kyanite granulite																				
Sample	CAT15-20								CAT15-24						25613K						
Location	Rim	Core	Sympl	Sympl	Sympl	Sympl	Core	Rim	Rim	Core	Rim	Core	Rim	Core	Core	Core	Core	Core	Core	Incl	Core
SiO_2	52.92	52.54	52.50	52.19	52.87	52.33	52.32	52.73	52.37	52.57	52.11	52.20	51.33	51.58	50.65	50.68	50.84	50.48	51.06	51.52	51.11
TiO_2	0.09	0.13	0.17	0.15	0.13	0.08	0.16	0.14	0.12	0.19	0.16	0.13	0.10	0.13	0.26	0.25	0.28	0.25	0.22	0.18	0.33
Al_2O_3	7.33	7.21	8.69	8.43	6.93	8.05	6.48	7.35	6.59	6.41	6.55	7.94	7.87	7.90	8.24	8.07	8.70	8.00	8.21	6.40	8.31
Cr_2O_3	0.18	0.15	0.30	0.00	0.06	0.05	0.47	0.72	0.53	0.66	0.90	0.36	0.56	0.68	0.06	0.15	0.16	0.15	0.11	0.18	0.05
FeO	1.99	1.69	1.76	1.76	1.78	1.84	1.92	1.99	1.57	1.78	1.73	1.83	1.83	1.77	2.50	2.41	2.60	2.25	2.64	2.65	2.43
MnO	0.05	0.00	0.00	0.00	0.00	0.02	0.06	0.05	0.08	0.02	0.02	0.06	0.04	0.00	0.04	0.02	0.01	0.01	0.01	0.06	0.02
MgO	14.42	14.70	13.38	13.71	14.20	14.16	15.38	14.22	14.98	15.04	14.76	14.62	14.27	14.34	13.41	13.78	13.52	13.03	13.46	14.52	13.61
CaO	22.17	22.68	21.20	21.69	21.93	22.01	23.22	22.18	23.05	22.82	22.62	22.28	22.29	22.11	22.37	21.87	21.79	20.97	21.85	22.35	22.44
Na_2O	1.81	1.42	2.21	1.91	1.89	1.62	0.95	1.68	1.23	1.20	1.31	1.27	1.36	1.44	1.74	1.59	1.64	1.58	1.70	1.55	1.47
K_2O	0.01	0.00	0.00	0.00	0.00	0.00	0.01	0.00	0.01	0.00	0.00	0.01	0.00	0.00	0.00	0.00	0.00	0.00	0.00	0.00	0.00
Total	100.98	100.53	100.21	99.83	99.78	100.14	100.96	101.05	100.52	100.69	100.15	100.70	99.64	99.94	99.27	98.83	99.52	96.73	99.25	99.41	99.78
Si	1.89	1.88	1.88	1.88	1.91	1.88	1.87	1.88	1.88	1.89	1.88	1.87	1.86	1.86	1.84	1.85	1.84	1.89	1.86	1.87	1.85
Ti	0.00	0.00	0.00	0.00	0.00	0.00	0.00	0.00	0.00	0.01	0.00	0.00	0.00	0.00	0.01	0.01	0.01	0.01	0.01	0.00	0.01
Al^{iv}	0.11	0.12	0.12	0.12	0.09	0.12	0.13	0.12	0.12	0.11	0.12	0.13	0.14	0.14	0.16	0.15	0.16	0.11	0.14	0.13	0.15
Al^{vi}	0.19	0.19	0.25	0.24	0.20	0.22	0.15	0.19	0.16	0.16	0.16	0.21	0.19	0.20	0.19	0.20	0.22	0.24	0.21	0.14	0.21
Fe^{3+}	0.04	0.02	0.00	0.01	0.02	0.00	0.03	0.01	0.03	0.01	0.02	0.00	0.02	0.02	0.07	0.05	0.04	0.00	0.04	0.08	0.03
Cr	0.01	0.00	0.01	0.00	0.00	0.00	0.01	0.02	0.02	0.02	0.03	0.01	0.02	0.02	0.00	0.00	0.00	0.00	0.00	0.01	0.00
Fe^{2+}	0.02	0.03	0.05	0.04	0.04	0.05	0.03	0.05	0.02	0.04	0.03	0.05	0.03	0.04	0.00	0.03	0.04	0.07	0.04	0.00	0.05
Mn	0.00	0.00	0.00	0.00	0.00	0.00	0.00	0.00	0.00	0.00	0.00	0.00	0.00	0.00	0.00	0.00	0.00	0.00	0.00	0.00	0.00
Mg	0.77	0.78	0.72	0.74	0.76	0.76	0.82	0.76	0.80	0.80	0.79	0.78	0.77	0.77	0.73	0.75	0.73	0.73	0.73	0.79	0.73
Ca	0.85	0.87	0.81	0.84	0.85	0.85	0.89	0.85	0.89	0.88	0.87	0.85	0.86	0.85	0.87	0.86	0.85	0.84	0.85	0.87	0.87
Na	0.13	0.10	0.15	0.13	0.13	0.11	0.07	0.12	0.09	0.08	0.09	0.09	0.10	0.10	0.12	0.11	0.12	0.11	0.12	0.11	0.10
K	0.00	0.00	0.00	0.00	0.00	0.00	0.00	0.00	0.00	0.00	0.00	0.00	0.00	0.00	0.00	0.00	0.00	0.00	0.00	0.00	0.00
Wo	0.51	0.51	0.51	0.51	0.51	0.51	0.50	0.51	0.51	0.51	0.51	0.51	0.51	0.51	0.52	0.51	0.51	0.51	0.51	0.50	0.52
En	0.46	0.46	0.45	0.45	0.46	0.46	0.46	0.45	0.46	0.46	0.46	0.46	0.46	0.46	0.43	0.45	0.44	0.44	0.44	0.45	0.44
Fs	0.04	0.03	0.03	0.03	0.03	0.03	0.03	0.04	0.03	0.03	0.03	0.03	0.03	0.03	0.05	0.04	0.05	0.04	0.05	0.05	0.04
Quad	0.87	0.90	0.84	0.86	0.86	0.88	0.93	0.88	0.91	0.91	0.90	0.91	0.90	0.89	0.87	0.88	0.88	0.88	0.87	0.88	0.89
Jd	0.12	0.10	0.16	0.14	0.13	0.12	0.06	0.12	0.08	0.08	0.09	0.09	0.10	0.10	0.11	0.10	0.11	0.12	0.11	0.08	0.10
Ae	0.02	0.01	0.00	0.00	0.01	0.00	0.01	0.01	0.01	0.00	0.01	0.00	0.01	0.01	0.03	0.02	0.01	0.00	0.01	0.03	0.01

Clinopyroxene analyses

Lithology	Garnet-clinopyroxene amphibolite							
Sample	CAT15-17B					CAT15-28		
Location	Rim	Core	Core	Core	Core	Core	Core	Core
SiO_2	51.70	51.42	51.62	51.11	51.59	51.43	51.88	51.72
TiO_2	0.41	0.42	0.37	0.46	0.35	0.26	0.31	0.27
Al_2O_3	6.83	6.52	6.58	6.79	6.12	5.11	5.76	5.26
Cr_2O_3	0.03	0.00	0.06	0.00	0.05	0.01	0.00	0.01
FeO	5.64	6.33	6.23	6.45	5.92	6.63	6.44	6.38
MnO	0.02	0.04	0.04	0.05	0.00	0.18	0.16	0.14
MgO	12.79	12.62	12.33	12.22	12.52	12.78	12.34	12.56
CaO	21.24	21.67	21.79	21.50	21.44	22.00	21.71	21.69
Na_2O	1.94	1.66	1.77	1.77	1.78	1.52	1.68	1.73
K_2O	0.00	0.00	0.01	0.01	0.00	0.00	0.01	0.01
Total	100.59	100.70	100.80	100.37	99.77	99.91	100.28	99.78
Si	1.87	1.87	1.87	1.87	1.89	1.89	1.90	1.90
Ti	0.01	0.01	0.01	0.01	0.01	0.01	0.01	0.01
Al^{iv}	0.13	0.13	0.13	0.13	0.11	0.11	0.10	0.10
Al^{vi}	0.16	0.15	0.16	0.16	0.16	0.11	0.15	0.13
Fe^{3+}	0.07	0.08	0.07	0.08	0.06	0.09	0.06	0.08
Cr	0.00	0.00	0.00	0.00	0.00	0.00	0.00	0.00
Fe^{2+}	0.10	0.12	0.12	0.12	0.12	0.11	0.14	0.11
Mn	0.00	0.00	0.00	0.00	0.00	0.01	0.00	0.00
Mg	0.69	0.68	0.67	0.66	0.68	0.70	0.67	0.69
Ca	0.82	0.84	0.85	0.84	0.84	0.87	0.85	0.85
Na	0.14	0.12	0.12	0.13	0.13	0.11	0.12	0.12
K	0.00	0.00	0.00	0.00	0.00	0.00	0.00	0.00
Wo	0.49	0.49	0.50	0.49	0.49	0.49	0.49	0.49
En	0.41	0.40	0.39	0.39	0.40	0.39	0.39	0.39
Fs	0.10	0.11	0.11	0.12	0.11	0.12	0.12	0.12
Quad	0.86	0.88	0.87	0.87	0.87	0.89	0.87	0.87
Jd	0.11	0.09	0.10	0.10	0.10	0.07	0.10	0.08
Ae	0.04	0.03	0.03	0.04	0.03	0.05	0.03	0.05

Orthopyroxene analyses

Lithology	Corona granulite									Garnet-clinopyroxene granulite			
Sample	CAT15-02							CAT13-27C1		CAT15-09A			
Location	Core	Core	Core	Core	Core	Core	Core	Core	Core	Core	Core	Core	Core
SiO_2	55.38	54.98	55.52	55.06	55.22	55.07	55.35	55.04	54.87	54.92	55.22	55.53	55.53
TiO_2	0.00	0.00	0.01	0.01	0.02	0.00	0.00	0.00	0.04	0.00	0.02	0.04	0.00
Al_2O_3	4.67	4.74	4.31	4.33	4.47	4.74	4.43	4.39	4.51	3.57	2.78	3.86	3.95
Cr_2O_3	0.00	0.02	0.00	0.02	0.01	0.00	0.04	0.01	0.04	0.04	0.03	0.01	0.00
FeO	4.74	4.70	4.77	4.79	4.83	4.85	4.86	6.09	6.32	5.17	5.17	5.21	5.26
MnO	0.01	0.04	0.06	0.07	0.05	0.04	0.04	0.05	0.06	0.04	0.04	0.09	0.00
MgO	35.40	35.68	35.70	35.48	34.97	35.17	34.94	34.78	34.82	35.57	35.86	35.68	35.89
CaO	0.32	0.25	0.24	0.28	0.28	0.26	0.27	0.19	0.32	0.32	0.27	0.35	0.31
Na_2O	0.00	0.00	0.00	0.02	0.01	0.00	0.02	0.00	0.03	0.02	0.01	0.02	0.02
K_2O	0.01	0.01	0.00	0.01	0.00	0.00	0.00	0.01	0.01	0.00	0.00	0.00	0.00
Total	100.54	100.42	100.61	100.08	99.86	100.14	99.94	100.57	101.02	99.64	99.40	100.80	100.97
Si	1.88	1.86	1.88	1.87	1.89	1.88	1.89	1.87	1.86	1.88	1.89	1.88	1.87
Ti	0.00	0.00	0.00	0.00	0.00	0.00	0.00	0.00	0.00	0.00	0.00	0.00	0.00
Al^{iv}	0.12	0.14	0.12	0.13	0.11	0.12	0.11	0.13	0.14	0.12	0.11	0.12	0.13
Al^{vi}	0.06	0.05	0.05	0.05	0.07	0.07	0.07	0.05	0.04	0.02	0.01	0.03	0.03
Fe^{3+}	0.06	0.08	0.07	0.08	0.04	0.06	0.04	0.07	0.10	0.10	0.10	0.09	0.09
Cr	0.00	0.00	0.00	0.00	0.00	0.00	0.00	0.00	0.00	0.00	0.00	0.00	0.00
Fe^{2+}	0.08	0.05	0.07	0.06	0.09	0.08	0.10	0.10	0.08	0.05	0.05	0.06	0.05
Mn	0.00	0.00	0.00	0.00	0.00	0.00	0.00	0.00	0.00	0.00	0.00	0.00	0.00
Mg	1.79	1.80	1.80	1.80	1.78	1.79	1.78	1.77	1.76	1.81	1.83	1.80	1.81
Ca	0.01	0.01	0.01	0.01	0.01	0.01	0.01	0.01	0.01	0.01	0.01	0.01	0.01
Na	0.00	0.00	0.00	0.00	0.00	0.00	0.00	0.00	0.00	0.00	0.00	0.00	0.00
K	0.00	0.00	0.00	0.00	0.00	0.00	0.00	0.00	0.00	0.00	0.00	0.00	0.00
Wo	0.01	0.00	0.00	0.01	0.01	0.00	0.01	0.00	0.01	0.01	0.01	0.01	0.01
En	0.92	0.93	0.93	0.92	0.92	0.92	0.92	0.91	0.90	0.92	0.92	0.92	0.92
Fs	0.07	0.07	0.07	0.07	0.07	0.07	0.07	0.09	0.09	0.08	0.07	0.08	0.08

Feldspar analyses

Lithology	Corona granulite														Garnet-clinopyroxene granulite											
Sample	CAT15-02						CAT13-27C1		CAT15-01B						CAT15-09A						CAT15-26Ba					
Location	Rim	Core	Core	Core	Rim	Rim	Core	Core	Rim	Core	Rim	Core	Core	Core	Rim	Core	Rim	Sympl-C	Sympl-C	Sympl-R	Core	Rim	Sympl	Core	Sympl	Core
SiO_2	45.75	45.91	45.57	45.50	45.96	45.63	45.38	44.83	49.47	50.59	50.63	51.82	48.39	48.89	58.89	48.31	56.95	57.39	56.57	59.20	49.03	59.07	59.25	48.42	59.42	50.42
TiO_2	0.01	0.03	0.03	0.00	0.00	0.00	0.00	0.01	0.02	0.00	0.00	0.00	0.01	0.00	0.03	0.02	0.00	0.00	0.01	0.00	0.00	0.01	0.00	0.00	0.00	0.04
Al_2O_3	34.37	34.98	35.21	34.81	34.76	34.60	34.61	35.83	31.89	30.97	32.25	31.28	33.23	33.31	26.10	33.86	27.75	27.27	27.88	26.07	33.14	26.12	26.42	33.11	25.75	32.14
Cr_2O_3	0.00	0.00	0.00	0.01	0.02	0.00	0.00	0.00	0.00	0.04	0.00	0.04	0.00	0.00	0.00	0.00	0.01	0.00	0.00	0.00	0.00	0.00	0.03	0.08	0.00	0.00
FeO	0.01	0.02	0.04	0.05	0.02	0.02	0.02	0.04	0.00	0.08	0.03	0.00	0.00	0.04	0.02	0.03	0.16	0.00	0.07	0.02	0.01	0.03	0.00	0.10	0.01	0.00
MnO	0.00	0.00	0.00	0.03	0.00	0.00	0.00	0.00	0.02	0.00	0.02	0.00	0.00	0.03	0.00	0.02	0.00	0.02	0.01	0.00	0.00	0.01	0.00	0.00	0.00	0.00
MgO	0.00	0.00	0.00	0.00	0.00	0.00	0.00	0.00	0.00	0.02	0.00	0.00	0.01	0.01	0.01	0.01	0.00	0.00	0.00	0.00	0.00	0.00	0.00	0.01	0.01	0.00
CaO	17.69	17.90	17.88	17.77	17.87	17.79	17.57	18.49	14.41	13.29	13.37	13.33	15.62	15.51	6.52	15.01	8.26	7.94	8.55	6.57	15.71	7.60	7.82	15.82	7.32	14.66
Na_2O	1.61	1.47	1.41	1.50	1.55	1.54	1.51	1.05	3.64	4.19	3.97	4.13	2.78	2.83	7.36	2.48	6.43	6.66	6.27	7.41	2.55	7.25	7.30	2.63	7.34	3.28
K_2O	0.00	0.00	0.02	0.00	0.01	0.01	0.00	0.01	0.02	0.04	0.02	0.00	0.00	0.03	0.00	0.00	0.02	0.03	0.03	0.01	0.01	0.03	0.04	0.01	0.03	0.02
Total	99.44	100.31	100.14	99.68	100.20	99.61	99.09	100.25	99.47	99.21	100.28	100.60	100.05	100.64	98.93	99.76	99.59	99.31	99.40	99.28	100.45	100.12	100.88	100.16	99.88	100.56
Si	2.12	2.11	2.10	2.10	2.11	2.11	2.11	2.06	2.27	2.32	2.29	2.34	2.21	2.22	2.65	2.21	2.56	2.58	2.55	2.65	2.23	2.63	2.62	2.21	2.65	2.28
Ti	0.00	0.00	0.00	0.00	0.00	0.00	0.00	0.00	0.00	0.00	0.00	0.00	0.00	0.00	0.00	0.00	0.00	0.00	0.00	0.00	0.00	0.00	0.00	0.00	0.00	0.00
Al	1.88	1.89	1.91	1.90	1.88	1.89	1.89	1.94	1.72	1.67	1.72	1.66	1.79	1.78	1.38	1.82	1.47	1.44	1.48	1.38	1.78	1.37	1.38	1.78	1.35	1.72
Cr	0.00	0.00	0.00	0.00	0.00	0.00	0.00	0.00	0.00	0.00	0.00	0.00	0.00	0.00	0.00	0.00	0.00	0.00	0.00	0.00	0.00	0.00	0.00	0.00	0.00	0.00
Fe^{2+}	0.00	0.00	0.00	0.00	0.00	0.00	0.00	0.00	0.00	0.00	0.00	0.00	0.00	0.00	0.00	0.00	0.01	0.00	0.00	0.00	0.00	0.00	0.00	0.00	0.00	0.00
Mn	0.00	0.00	0.00	0.00	0.00	0.00	0.00	0.00	0.00	0.00	0.00	0.00	0.00	0.00	0.00	0.00	0.00	0.00	0.00	0.00	0.00	0.00	0.00	0.00	0.00	0.00
Mg	0.00	0.00	0.00	0.00	0.00	0.00	0.00	0.00	0.00	0.00	0.00	0.00	0.00	0.00	0.00	0.00	0.00	0.00	0.00	0.00	0.00	0.00	0.00	0.00	0.00	0.00
Ca	0.88	0.88	0.88	0.88	0.88	0.88	0.87	0.91	0.71	0.65	0.65	0.64	0.77	0.75	0.31	0.73	0.40	0.38	0.41	0.32	0.77	0.36	0.37	0.77	0.35	0.71
Na	0.14	0.13	0.13	0.13	0.14	0.14	0.14	0.09	0.32	0.37	0.35	0.36	0.25	0.25	0.64	0.22	0.56	0.58	0.55	0.64	0.22	0.63	0.63	0.23	0.63	0.29
K	0.00	0.00	0.00	0.00	0.00	0.00	0.00	0.00	0.00	0.00	0.00	0.00	0.00	0.00	0.00	0.00	0.00	0.00	0.00	0.00	0.00	0.00	0.00	0.00	0.00	0.00
Total	5.02	5.01	5.01	5.02	5.02	5.02	5.01	5.01	5.03	5.03	5.02	5.01	5.02	5.01	4.98	4.99	4.99	4.99	4.99	4.98	5.00	5.00	5.00	5.01	4.99	5.00
X_{Ab}	0.14	0.13	0.12	0.13	0.14	0.14	0.13	0.09	0.31	0.36	0.35	0.36	0.24	0.25	0.67	0.23	0.58	0.60	0.57	0.67	0.23	0.63	0.63	0.23	0.64	0.29
X_{An}	0.86	0.87	0.87	0.87	0.86	0.86	0.87	0.91	0.69	0.64	0.65	0.64	0.76	0.75	0.33	0.77	0.42	0.40	0.43	0.33	0.77	0.37	0.37	0.77	0.35	0.71
X_{Or}	0.00	0.00	0.00	0.00	0.00	0.00	0.00	0.00	0.00	0.00	0.00	0.00	0.00	0.00	0.00	0.00	0.00	0.00	0.00	0.00	0.00	0.00	0.00	0.00	0.00	0.00

Sympl, adjacent to or within symplectite; C, core; R, rim.

Feldspar analyses

Lithology	Kyanite granulite				Amphibolite										Garnet-clinopyroxene amphibolite											
Sample	CAT15-20				CAT15-23										CAT15-17B							CAT15-28				
Location	Sympl	Sympl	Sympl	Sympl	Rim	Core	Rim	Core	Core	Rim	Core	Core	Core	Rim	Core	Core	Rim	Rim	Rim	Core	Core	Core	Core	Rim	Rim	Rim
SiO_2	58.46	60.08	58.85	59.98	61.92	61.10	62.80	60.04	60.68	62.86	60.49	60.37	60.79	64.22	60.17	59.69	61.39	61.72	61.63	60.23	60.47	60.70	60.17	61.51	62.76	61.82
TiO_2	0.00	0.00	0.00	0.00	0.02	0.01	0.00	0.01	0.00	0.01	0.01	0.02	0.00	0.02	0.00	0.01	0.01	0.02	0.03	0.02	0.00	0.00	0.00	0.01	0.00	0.00
Al_2O_3	26.52	25.61	26.20	25.73	24.06	24.79	23.56	25.71	24.95	23.68	25.25	25.12	25.09	22.47	25.24	25.43	24.72	24.28	24.38	24.98	25.04	25.61	25.73	25.11	24.60	25.15
Cr_2O_3	0.00	0.00	0.00	0.01	0.03	0.02	0.00	0.02	0.00	0.01	0.04	0.00	0.04	0.00	0.03	0.01	0.00	0.01	0.01	0.00	0.00	0.00	0.00	0.00	0.00	0.00
FeO	0.02	0.05	0.03	0.06	0.08	0.04	0.08	0.06	0.11	0.04	0.08	0.03	0.03	0.04	0.03	0.03	0.10	0.01	0.00	0.00	0.05	0.06	0.06	0.13	0.14	0.07
MnO	0.01	0.02	0.00	0.00	0.00	0.02	0.00	0.03	0.00	0.00	0.00	0.00	0.00	0.03	0.02	0.00	0.01	0.02	0.00	0.00	0.07	0.00	0.00	0.00	0.00	0.02
MgO	0.00	0.00	0.00	0.00	0.00	0.00	0.00	0.00	0.02	0.00	0.00	0.00	0.00	0.01	0.00	0.00	0.00	0.00	0.00	0.00	0.00	0.00	0.00	0.00	0.00	0.00
CaO	7.31	6.06	7.02	6.45	4.99	5.66	4.28	6.54	5.83	4.46	5.98	5.99	5.97	3.07	6.48	6.83	5.83	5.29	5.70	6.38	6.52	6.29	6.49	5.76	5.35	5.73
Na_2O	7.15	7.88	7.54	7.72	8.51	8.33	9.10	7.91	8.11	9.09	8.20	8.08	8.27	9.76	7.92	7.74	8.38	8.51	8.25	7.81	7.81	8.04	7.95	8.41	8.58	8.32
K_2O	0.03	0.01	0.01	0.00	0.06	0.02	0.04	0.05	0.05	0.07	0.03	0.05	0.04	0.06	0.02	0.01	0.04	0.04	0.02	0.03	0.02	0.01	0.00	0.01	0.03	0.01
Total	99.49	99.72	99.65	99.96	99.69	99.99	99.86	100.37	99.75	100.21	100.07	99.68	100.23	99.68	99.92	99.74	100.49	99.89	100.01	99.46	99.99	100.71	100.41	100.95	101.46	101.12
Si	2.62	2.68	2.63	2.67	2.75	2.71	2.78	2.66	2.70	2.77	2.69	2.69	2.70	2.84	2.68	2.66	2.71	2.74	2.73	2.69	2.69	2.68	2.67	2.71	2.74	2.71
Ti	0.00	0.00	0.00	0.00	0.00	0.00	0.00	0.00	0.00	0.00	0.00	0.00	0.00	0.00	0.00	0.00	0.00	0.00	0.00	0.00	0.00	0.00	0.00	0.00	0.00	0.00
Al	1.40	1.34	1.38	1.35	1.26	1.30	1.23	1.34	1.31	1.23	1.32	1.32	1.31	1.17	1.32	1.34	1.29	1.27	1.27	1.32	1.31	1.33	1.34	1.30	1.27	1.30
Cr	0.00	0.00	0.00	0.00	0.00	0.00	0.00	0.00	0.00	0.00	0.00	0.00	0.00	0.00	0.00	0.00	0.00	0.00	0.00	0.00	0.00	0.00	0.00	0.00	0.00	0.00
Fe^{2+}	0.00	0.00	0.00	0.00	0.00	0.00	0.00	0.00	0.00	0.00	0.00	0.00	0.00	0.00	0.00	0.00	0.00	0.00	0.00	0.00	0.00	0.00	0.00	0.00	0.01	0.00
Mn	0.00	0.00	0.00	0.00	0.00	0.00	0.00	0.00	0.00	0.00	0.00	0.00	0.00	0.00	0.00	0.00	0.00	0.00	0.00	0.00	0.00	0.00	0.00	0.00	0.00	0.00
Mg	0.00	0.00	0.00	0.00	0.00	0.00	0.00	0.00	0.00	0.00	0.00	0.00	0.00	0.00	0.00	0.00	0.00	0.00	0.00	0.00	0.00	0.00	0.00	0.00	0.00	0.00
Ca	0.35	0.29	0.34	0.31	0.24	0.27	0.20	0.31	0.28	0.21	0.28	0.29	0.28	0.15	0.31	0.33	0.28	0.25	0.27	0.31	0.31	0.30	0.31	0.27	0.25	0.27
Na	0.62	0.68	0.65	0.67	0.73	0.72	0.78	0.68	0.70	0.78	0.71	0.70	0.71	0.84	0.68	0.67	0.72	0.73	0.71	0.68	0.67	0.69	0.68	0.72	0.73	0.71
K	0.00	0.00	0.00	0.00	0.00	0.00	0.00	0.00	0.00	0.00	0.00	0.00	0.00	0.00	0.00	0.00	0.00	0.00	0.00	0.00	0.00	0.00	0.00	0.00	0.00	0.00
Total	4.99	4.99	5.00	4.99	4.99	5.00	5.00	5.01	5.00	5.00	5.01	5.00	5.01	5.00	5.00	5.00	5.00	4.99	4.99	4.99	4.99	5.00	5.00	5.00	4.99	4.99
X_{Ab}	0.64	0.70	0.66	0.68	0.75	0.73	0.79	0.68	0.71	0.78	0.71	0.71	0.71	0.85	0.69	0.67	0.72	0.74	0.72	0.69	0.68	0.70	0.69	0.72	0.74	0.72
X_{An}	0.36	0.30	0.34	0.32	0.24	0.27	0.21	0.31	0.28	0.21	0.29	0.29	0.28	0.15	0.31	0.33	0.28	0.26	0.28	0.31	0.32	0.30	0.31	0.27	0.26	0.28
X_{Or}	0.00	0.00	0.00	0.00	0.00	0.00	0.00	0.00	0.00	0.00	0.00	0.00	0.00	0.00	0.00	0.00	0.00	0.00	0.00	0.00	0.00	0.00	0.00	0.00	0.00	0.00

Amphibole analyses

Lithology	Corona granulite																					
Sample	CAT15-02										CAT13-27C1				CAT15-01B							
Location	Core	Core	Core	Core	Core	Core	Core	Core	Core	Core	Core	Core	Core	Core	Core	Core	Rim	Core	Rim	Rim	Rim	Core
SiO_2	45.56	46.23	45.87	47.57	46.72	45.17	46.99	42.64	45.79	42.85	44.18	47.37	43.20	43.36	42.00	41.71	41.16	43.08	43.32	42.97	42.50	42.20
TiO_2	0.05	0.08	0.05	0.02	0.04	0.04	0.03	0.07	0.01	0.04	0.41	0.27	0.31	0.35	0.54	0.57	0.52	1.22	0.37	0.34	0.45	0.48
Al_2O_3	16.57	15.01	14.97	13.51	15.03	17.44	13.87	17.97	14.82	17.35	18.07	13.65	20.23	19.94	19.08	19.47	19.54	17.31	18.85	19.00	19.78	19.84
Cr_2O_3	0.00	0.01	0.06	0.03	0.10	0.20	0.00	0.01	0.00	0.04	0.30	0.27	0.00	0.04	0.65	0.58	0.56	1.14	0.14	0.07	0.15	0.09
FeO	2.14	2.12	2.28	2.05	2.47	3.13	3.18	4.40	3.61	3.15	3.55	3.38	3.41	3.64	3.20	3.43	3.68	3.52	2.08	2.05	2.70	2.68
MnO	0.02	0.04	0.01	0.01	0.06	0.00	0.06	0.03	0.08	0.05	0.01	0.03	0.07	0.03	0.07	0.02	0.01	0.00	0.01	0.00	0.01	0.02
MgO	18.55	19.04	18.63	19.63	18.71	17.51	18.04	16.37	17.57	16.78	16.74	18.31	16.59	16.77	17.25	16.73	16.83	17.05	18.25	18.16	17.53	17.44
CaO	12.83	12.54	12.91	12.81	12.88	12.30	12.73	12.77	13.17	13.07	13.33	13.43	13.13	12.99	12.22	12.14	12.00	12.35	12.42	12.46	12.44	12.35
Na_2O	1.86	1.63	1.51	1.47	1.49	1.63	1.37	2.27	1.47	1.81	1.61	1.19	1.73	1.83	2.77	2.95	2.95	2.93	2.62	2.61	2.82	2.86
K_2O	0.03	0.00	0.01	0.01	0.00	0.00	0.00	0.00	0.02	0.03	0.09	0.04	0.05	0.03	0.07	0.10	0.10	0.10	0.08	0.09	0.09	0.09
H_2O*	2.16	2.15	2.16	2.17	2.16	2.16	2.16	2.12	2.15	2.14	2.06	2.10	2.09	2.07	2.02	2.01	2.02	1.85	2.07	2.08	2.05	2.04
Total	99.77	98.86	98.44	99.27	99.66	99.59	98.43	98.64	98.69	97.32	100.37	100.03	100.81	101.05	99.87	99.70	99.36	100.54	100.21	99.83	100.53	100.10
Si	6.30	6.44	6.42	6.59	6.46	6.26	6.59	6.04	6.44	6.12	6.12	6.55	5.94	5.95	5.88	5.86	5.80	6.02	6.00	5.98	5.89	5.87
Ti	0.01	0.01	0.01	0.00	0.00	0.00	0.00	0.01	0.00	0.00	0.04	0.03	0.03	0.04	0.06	0.06	0.06	0.13	0.04	0.04	0.05	0.05
Al^{iv}	1.70	1.56	1.58	1.41	1.54	1.74	1.42	1.96	1.56	1.88	1.89	1.45	2.06	2.05	2.12	2.14	2.20	1.98	2.00	2.03	2.11	2.13
Al^{vi}	1.00	0.90	0.89	0.80	0.91	1.11	0.88	1.04	0.89	1.04	1.06	0.78	1.22	1.18	1.02	1.08	1.05	0.87	1.08	1.09	1.12	1.13
Cr	0.00	0.00	0.01	0.00	0.01	0.02	0.00	0.00	0.00	0.00	0.03	0.03	0.00	0.00	0.07	0.07	0.06	0.13	0.02	0.01	0.02	0.01
Fe^{3+}	0.23	0.24	0.27	0.23	0.26	0.28	0.29	0.36	0.29	0.33	0.38	0.33	0.39	0.40	0.33	0.31	0.36	0.31	0.22	0.23	0.27	0.27
Fe^{2+}	0.02	0.01	0.00	0.01	0.02	0.09	0.09	0.16	0.14	0.04	0.03	0.06	0.01	0.02	0.04	0.09	0.07	0.10	0.02	0.01	0.05	0.05
Mn	0.00	0.00	0.00	0.00	0.01	0.00	0.01	0.00	0.01	0.00	0.00	0.00	0.01	0.00	0.01	0.00	0.00	0.00	0.00	0.00	0.00	0.00
Mg	3.82	3.95	3.89	4.05	3.86	3.62	3.77	3.46	3.68	3.57	3.46	3.78	3.40	3.43	3.60	3.50	3.54	3.55	3.77	3.76	3.62	3.62
Ca	1.90	1.87	1.94	1.90	1.91	1.83	1.91	1.94	1.98	2.00	1.98	1.99	1.94	1.91	1.83	1.83	1.81	1.85	1.84	1.86	1.85	1.84
Na	0.50	0.44	0.41	0.40	0.40	0.44	0.37	0.62	0.40	0.50	0.43	0.32	0.46	0.49	0.75	0.80	0.81	0.79	0.70	0.70	0.76	0.77
K	0.01	0.00	0.00	0.00	0.00	0.00	0.00	0.00	0.00	0.01	0.02	0.01	0.01	0.01	0.01	0.02	0.02	0.02	0.01	0.02	0.02	0.02
OH*	1.99	1.98	1.99	2.00	1.99	1.99	1.99	1.99	2.00	1.99	1.92	1.94	1.94	1.93	1.89	1.88	1.89	1.74	1.92	1.93	1.91	1.90
Mg#	99.40	99.72	99.97	99.78	99.38	97.70	97.77	95.58	96.39	98.81	99.08	98.38	99.82	99.48	98.82	97.39	97.98	97.29	99.47	99.68	98.72	98.72

Amphibole analyses

Lithology	Garnet-clinopyroxene granulite																
Sample	CAT15-09A									CAT15-06Bdw					CAT15-26Ba	
Location	Core	Core	Rim	Core	Core	Core	Core	Core	Rim	Core	Core	Core	Core	Rim	Core	Core
SiO_2	44.88	44.58	44.78	47.69	46.82	47.69	48.74	45.74	43.84	45.12	45.38	45.24	45.46	45.24	44.89	44.48
TiO_2	0.49	0.54	0.57	0.15	0.13	0.09	0.14	0.15	0.09	0.28	0.37	0.27	0.36	0.33	0.30	0.31
Al_2O_3	15.79	16.28	16.19	12.69	13.87	12.98	12.13	15.13	17.93	16.56	16.55	16.18	16.19	16.39	18.58	19.18
Cr_2O_3	0.65	0.64	0.76	0.00	0.08	0.04	0.07	0.02	0.02	0.34	0.21	0.27	0.32	0.27	0.40	0.48
FeO	2.59	2.50	2.47	2.15	2.23	2.08	2.18	2.31	2.84	4.42	4.29	4.44	4.45	4.57	2.24	2.39
MnO	0.01	0.00	0.00	0.00	0.00	0.02	0.02	0.00	0.01	0.02	0.01	0.03	0.04	0.03	0.00	0.01
MgO	18.34	18.17	18.15	20.09	19.66	19.91	20.25	19.00	17.49	16.84	16.79	16.79	16.87	16.73	17.55	17.44
CaO	11.90	11.99	12.23	12.08	11.96	12.10	12.11	11.75	12.31	12.14	12.21	12.30	12.53	12.31	12.10	12.19
Na_2O	2.56	2.54	2.19	2.22	2.29	2.18	1.96	2.43	2.58	2.03	2.12	2.05	2.10	2.03	2.62	2.63
K_2O	0.07	0.06	0.03	0.03	0.02	0.03	0.05	0.05	0.04	0.17	0.18	0.13	0.16	0.12	0.07	0.11
H_2O*	2.04	2.03	2.03	2.13	2.14	2.15	2.14	2.13	2.13	2.08	2.06	2.08	2.06	2.07	2.09	2.09
Total	99.31	99.34	99.40	99.23	99.20	99.26	99.77	98.72	99.28	99.99	100.17	99.78	100.54	100.09	100.84	101.31
Si	6.29	6.25	6.25	6.64	6.53	6.63	6.73	6.41	6.14	6.29	6.31	6.32	6.33	6.31	6.17	6.10
Ti	0.05	0.06	0.06	0.02	0.01	0.01	0.02	0.02	0.01	0.03	0.04	0.03	0.04	0.03	0.03	0.03
Al^{iv}	1.71	1.75	1.75	1.36	1.48	1.37	1.27	1.59	1.86	1.71	1.69	1.68	1.67	1.69	1.83	1.91
Al^{vi}	0.90	0.94	0.92	0.72	0.80	0.76	0.71	0.91	1.10	1.01	1.03	0.99	0.99	1.00	1.18	1.19
Cr	0.07	0.07	0.08	0.00	0.01	0.00	0.01	0.00	0.00	0.04	0.02	0.03	0.04	0.03	0.04	0.05
Fe^{3+}	0.15	0.15	0.23	0.13	0.13	0.12	0.13	0.14	0.17	0.26	0.25	0.26	0.15	0.27	0.13	0.14
Fe^{2+}	0.15	0.15	0.06	0.13	0.13	0.12	0.13	0.14	0.17	0.26	0.25	0.26	0.37	0.26	0.13	0.14
Mn	0.00	0.00	0.00	0.00	0.00	0.00	0.00	0.00	0.00	0.00	0.00	0.00	0.01	0.00	0.00	0.00
Mg	3.83	3.80	3.78	4.17	4.09	4.13	4.17	3.97	3.65	3.50	3.48	3.50	3.50	3.48	3.60	3.56
Ca	1.79	1.80	1.83	1.80	1.79	1.80	1.79	1.77	1.85	1.81	1.82	1.84	1.87	1.84	1.78	1.79
Na	0.70	0.69	0.59	0.60	0.62	0.59	0.53	0.66	0.70	0.55	0.57	0.55	0.57	0.55	0.70	0.70
K	0.01	0.01	0.01	0.01	0.00	0.01	0.01	0.01	0.01	0.03	0.03	0.02	0.03	0.02	0.01	0.02
OH*	1.90	1.89	1.88	1.97	1.97	1.98	1.97	1.97	1.98	1.94	1.92	1.94	1.92	1.93	1.94	1.94
Mg#	96.18	96.27	98.41	97.07	96.92	97.17	97.09	96.69	95.65	93.14	93.28	92.98	90.56	92.94	96.54	96.30

Amphibole analyses

Lithology	Kyanite granulite													
Sample	CAT15-20						CAT15-24				25613K			
Location	Core	Core	Core	Core	Core	Core	Core	Rim	Core	Core	Core	Core	Core	Incl
SiO_2	45.66	45.92	46.02	45.82	46.15	47.34	49.00	47.31	46.81	46.48	48.66	44.75	44.20	49.16
TiO_2	0.29	0.26	0.26	0.22	0.04	0.11	0.20	0.26	0.27	0.25	0.31	0.51	0.58	0.21
Al_2O_3	15.96	15.85	15.78	15.84	15.94	14.34	12.01	13.62	14.73	14.10	10.61	15.91	16.02	11.73
Cr_2O_3	0.44	0.50	0.43	0.44	0.13	0.21	0.57	0.48	0.73	0.67	0.14	0.17	0.28	0.14
FeO	3.61	3.64	3.63	4.41	4.24	4.54	2.89	3.03	3.14	3.18	4.23	4.51	4.52	3.27
MnO	0.02	0.04	0.05	0.07	0.03	0.05	0.00	0.00	0.00	0.02	0.02	0.03	0.01	0.00
MgO	16.88	17.17	17.41	16.93	17.55	17.45	18.99	18.67	17.83	17.94	18.82	16.83	16.77	18.90
CaO	11.63	11.63	11.72	11.65	11.56	11.92	12.78	12.24	11.95	12.22	12.49	12.07	12.32	12.26
Na_2O	2.43	2.45	2.42	2.37	2.22	2.03	1.29	1.66	1.94	1.83	1.34	2.08	1.97	1.71
K_2O	0.04	0.03	0.02	0.04	0.02	0.01	0.03	0.07	0.09	0.04	0.01	0.08	0.05	0.07
H_2O*	2.09	2.10	2.10	2.10	2.15	2.13	2.12	2.11	2.10	2.10	2.09	2.03	2.01	2.12
Total	99.06	99.58	99.84	99.90	100.02	100.15	99.88	99.44	99.59	98.82	98.73	98.97	98.74	99.56
Si	6.40	6.40	6.40	6.39	6.40	6.55	6.77	6.58	6.50	6.52	6.82	6.30	6.24	6.81
Ti	0.03	0.03	0.03	0.02	0.01	0.01	0.02	0.03	0.03	0.03	0.03	0.05	0.06	0.02
Al^{iv}	1.60	1.60	1.60	1.62	1.60	1.45	1.24	1.42	1.50	1.48	1.18	1.70	1.76	1.19
Al^{vi}	1.04	1.01	0.99	0.99	1.01	0.89	0.72	0.81	0.92	0.85	0.57	0.94	0.91	0.73
Cr	0.05	0.06	0.05	0.05	0.01	0.02	0.06	0.05	0.08	0.07	0.02	0.02	0.03	0.02
Fe^{3+}	0.21	0.21	0.21	0.26	0.25	0.35	0.23	0.25	0.24	0.25	0.38	0.37	0.42	0.25
Fe^{2+}	0.21	0.21	0.21	0.25	0.25	0.17	0.10	0.11	0.12	0.12	0.11	0.16	0.11	0.13
Mn	0.00	0.01	0.01	0.01	0.00	0.01	0.00	0.00	0.00	0.00	0.00	0.00	0.00	0.00
Mg	3.53	3.57	3.61	3.52	3.63	3.60	3.91	3.87	3.69	3.75	3.93	3.53	3.53	3.90
Ca	1.75	1.74	1.75	1.74	1.72	1.77	1.89	1.82	1.78	1.84	1.88	1.82	1.86	1.82
Na	0.66	0.66	0.65	0.64	0.60	0.54	0.35	0.45	0.52	0.50	0.36	0.57	0.54	0.46
K	0.01	0.01	0.00	0.01	0.00	0.00	0.01	0.01	0.02	0.01	0.00	0.01	0.01	0.01
OH*	1.94	1.95	1.95	1.95	1.99	1.98	1.96	1.95	1.94	1.95	1.93	1.89	1.88	1.96
Mg#	94.36	94.42	94.53	93.26	93.67	95.41	97.50	97.31	96.80	96.80	97.18	95.74	96.98	96.85

Amphibole analyses

Lithology	Amphibolite																			
Sample	CAT15-23									CAT15-01dw										
Location	Core	Rim	Rim	Core	Rim	Core	Rim	Core	Rim	Core	Core	Core	Core	Core	Core	Core	Core	Core	Core
SiO_2	47.05	43.79	47.01	45.09	44.88	45.90	47.81	45.33	45.45	43.56	44.16	43.86	43.84	43.87	43.85	43.89	44.16	43.63	43.67
TiO_2	0.58	0.49	0.36	0.64	0.52	0.68	0.38	0.56	0.54	0.03	0.07	0.04	0.07	0.06	0.07	0.07	0.05	0.06	0.07
Al_2O_3	11.41	9.94	9.79	12.41	11.57	12.72	9.70	13.09	11.58	17.40	17.30	17.03	16.74	16.03	16.78	17.22	16.33	17.03	17.93
Cr_2O_3	0.10	0.04	0.03	0.11	0.02	0.08	0.02	0.11	0.18	0.71	0.46	0.44	0.24	1.04	0.56	0.39	0.57	0.60	0.85
FeO	10.71	10.72	10.17	10.15	10.25	10.13	9.98	10.24	10.74	4.61	4.71	4.30	4.33	4.97	5.07	4.43	4.68	4.41	4.57
MnO	0.22	0.17	0.24	0.15	0.23	0.24	0.24	0.18	0.19	0.06	0.11	0.05	0.04	0.10	0.06	0.08	0.12	0.01	0.06
MgO	14.01	15.52	15.38	14.29	14.89	14.16	15.86	13.80	14.49	16.37	16.07	16.60	17.03	16.28	16.42	16.31	16.34	16.59	16.10
CaO	10.79	12.07	11.91	11.15	12.16	11.24	12.26	11.08	12.13	12.31	12.02	12.16	12.06	11.80	11.89	12.28	12.15	12.23	12.22
Na_2O	1.89	1.56	1.45	2.06	1.47	2.04	1.22	2.14	1.58	1.75	1.74	1.64	1.69	1.83	1.85	1.73	1.79	1.76	1.69
K_2O	0.12	0.17	0.13	0.10	0.18	0.10	0.13	0.12	0.13	0.12	0.08	0.12	0.09	0.10	0.12	0.17	0.09	0.11	0.13
H_2O*	1.97	1.97	2.02	1.94	1.97	1.94	2.02	1.96	1.96	2.14	2.13	2.14	2.13	2.13	2.13	2.13	2.13	2.13	2.13
Total	98.85	96.44	98.50	98.08	98.15	99.23	99.63	98.62	98.97	99.07	98.83	98.39	98.27	98.20	98.81	98.68	98.41	98.57	99.42
Si	6.78	6.48	6.79	6.58	6.52	6.61	6.81	6.58	6.57	6.13	6.21	6.19	6.19	6.23	6.19	6.19	6.25	6.16	6.12
Ti	0.06	0.05	0.04	0.07	0.06	0.07	0.04	0.06	0.06	0.00	0.01	0.01	0.01	0.01	0.01	0.01	0.01	0.01	0.01
Al^{iv}	1.22	1.52	1.21	1.42	1.49	1.39	1.19	1.42	1.44	1.88	1.79	1.81	1.81	1.77	1.82	1.81	1.75	1.84	1.89
Al^{vi}	0.71	0.21	0.46	0.71	0.50	0.77	0.43	0.82	0.54	1.01	1.08	1.03	0.98	0.92	0.97	1.05	0.97	0.99	1.08
Cr	0.01	0.00	0.00	0.01	0.00	0.01	0.00	0.01	0.02	0.08	0.05	0.05	0.03	0.12	0.06	0.04	0.06	0.07	0.09
Fe^{3+}	0.40	0.92	0.48	0.28	0.66	0.26	0.54	0.25	0.55	0.44	0.39	0.41	0.43	0.43	0.45	0.40	0.41	0.42	0.41
Fe^{2+}	0.89	0.41	0.75	0.95	0.59	0.96	0.65	1.00	0.75	0.11	0.16	0.10	0.08	0.16	0.15	0.13	0.14	0.10	0.13
Mn	0.03	0.02	0.03	0.02	0.03	0.03	0.03	0.02	0.02	0.01	0.01	0.01	0.01	0.01	0.01	0.01	0.01	0.00	0.01
Mg	3.01	3.42	3.31	3.11	3.22	3.04	3.37	2.98	3.12	3.43	3.37	3.49	3.59	3.45	3.45	3.43	3.45	3.49	3.36
Ca	1.67	1.91	1.84	1.74	1.89	1.73	1.87	1.72	1.88	1.86	1.81	1.84	1.83	1.80	1.80	1.86	1.84	1.85	1.83
Na	0.53	0.45	0.41	0.58	0.42	0.57	0.34	0.60	0.44	0.48	0.47	0.45	0.46	0.51	0.51	0.47	0.49	0.48	0.46
K	0.02	0.03	0.03	0.02	0.03	0.02	0.02	0.02	0.02	0.02	0.01	0.02	0.02	0.02	0.02	0.03	0.02	0.02	0.02
OH*	1.87	1.89	1.92	1.86	1.89	1.85	1.92	1.88	1.88	1.99	1.99	1.99	1.98	1.99	1.99	1.99	1.99	1.99	1.99
Mg#	77.09	89.42	81.62	76.52	84.59	75.94	83.81	74.96	80.62	97.00	95.44	97.14	97.82	95.54	95.86	96.43	96.02	97.11	96.36

Amphibole analyses

Lithology	Garnet-clinopyroxene amphibolite																			
Sample	CAT15-17B										CAT15-28									
Location	Core	Rim	Rim	Core	Core	Core	Core	Rim	Core	Core	Core	Rim	Rim	Rim	Core	Rim	Core	Core	Core	Core
SiO_2	44.49	44.58	44.40	44.34	46.95	46.93	44.31	44.75	44.11	44.42	45.08	44.08	45.02	44.08	44.89	45.52	44.65	45.16	44.36	45.94
TiO_2	1.10	1.10	1.15	1.09	0.55	0.44	0.96	1.00	1.01	1.10	0.94	0.99	0.24	0.34	0.98	0.38	0.96	0.80	0.96	0.76
Al_2O_3	14.77	15.23	15.36	15.36	9.45	9.53	14.30	15.15	15.47	15.23	14.87	14.25	11.08	11.88	14.50	10.87	15.20	14.12	15.18	13.64
Cr_2O_3	0.10	0.03	0.03	0.09	0.01	0.05	0.09	0.00	0.00	0.09	0.08	0.07	0.16	0.02	0.06	0.01	0.04	0.01	0.09	0.08
FeO	8.56	9.25	9.65	9.27	14.79	13.53	9.56	9.37	9.85	9.48	9.37	10.51	15.38	16.53	10.80	15.53	9.53	9.47	9.81	9.29
MnO	0.04	0.03	0.06	0.03	0.33	0.32	0.01	0.00	0.03	0.02	0.11	0.20	0.43	0.47	0.23	0.47	0.07	0.10	0.07	0.10
MgO	14.85	14.16	13.74	14.27	13.41	13.82	14.67	14.11	14.18	14.14	14.03	13.87	12.22	11.42	13.39	12.22	14.53	14.82	14.24	15.14
CaO	12.47	11.53	11.71	11.29	11.15	11.78	12.25	11.32	11.64	11.36	11.56	12.25	11.99	12.05	11.33	12.14	11.37	12.23	12.08	11.38
Na_2O	2.11	2.28	2.16	2.52	1.49	1.46	2.06	2.22	2.26	2.43	2.47	2.12	1.77	1.87	2.31	1.55	2.63	1.98	2.32	2.38
K_2O	0.07	0.09	0.07	0.07	0.01	0.03	0.08	0.10	0.12	0.10	0.05	0.03	0.04	0.05	0.05	0.03	0.06	0.03	0.05	0.04
H_2O*	1.85	1.85	1.84	1.85	1.94	1.97	1.88	1.87	1.87	1.85	1.88	1.86	1.99	1.96	1.86	1.96	1.88	1.92	1.88	1.93
Total	100.41	100.14	100.18	100.17	100.07	99.84	100.17	99.90	100.54	100.22	100.45	100.22	100.32	100.67	100.41	100.69	100.92	100.64	101.05	100.67
Si	6.30	6.35	6.32	6.32	6.76	6.77	6.30	6.38	6.25	6.33	6.41	6.30	6.55	6.42	6.42	6.59	6.32	6.38	6.27	6.50
Ti	0.12	0.12	0.12	0.12	0.06	0.05	0.10	0.11	0.11	0.12	0.10	0.11	0.03	0.04	0.11	0.04	0.10	0.09	0.10	0.08
Al^{iv}	1.70	1.65	1.68	1.68	1.24	1.23	1.70	1.62	1.75	1.67	1.59	1.70	1.46	1.58	1.58	1.42	1.68	1.62	1.73	1.50
Al^{vi}	0.77	0.91	0.90	0.90	0.37	0.39	0.70	0.93	0.83	0.89	0.91	0.70	0.44	0.46	0.87	0.44	0.86	0.73	0.80	0.77
Cr	0.01	0.00	0.00	0.01	0.00	0.01	0.01	0.00	0.00	0.01	0.01	0.01	0.02	0.00	0.01	0.00	0.00	0.00	0.01	0.01
Fe^{3+}	0.45	0.27	0.40	0.29	0.75	0.62	0.56	0.28	0.53	0.28	0.21	0.53	0.63	0.70	0.27	0.66	0.30	0.51	0.47	0.29
Fe^{2+}	0.56	0.84	0.75	0.81	1.03	1.01	0.58	0.84	0.64	0.85	0.90	0.73	1.24	1.31	1.02	1.21	0.83	0.61	0.70	0.81
Mn	0.01	0.00	0.01	0.00	0.04	0.04	0.00	0.00	0.00	0.00	0.01	0.03	0.05	0.06	0.03	0.05	0.01	0.01	0.01	0.01
Mg	3.13	3.01	2.92	3.03	2.88	2.97	3.11	3.00	3.00	3.01	2.98	2.96	2.65	2.48	2.86	2.64	3.07	3.12	3.00	3.19
Ca	1.89	1.76	1.79	1.72	1.72	1.82	1.87	1.73	1.77	1.74	1.76	1.88	1.87	1.88	1.74	1.88	1.73	1.85	1.83	1.72
Na	0.58	0.63	0.60	0.70	0.42	0.41	0.57	0.62	0.62	0.67	0.68	0.59	0.50	0.53	0.64	0.44	0.72	0.54	0.64	0.65
K	0.01	0.02	0.01	0.01	0.00	0.01	0.01	0.02	0.02	0.02	0.01	0.01	0.01	0.01	0.01	0.01	0.01	0.01	0.01	0.01
OH*	1.77	1.76	1.75	1.77	1.88	1.91	1.80	1.79	1.79	1.76	1.80	1.79	1.95	1.93	1.79	1.92	1.80	1.83	1.80	1.84
Mg#	84.75	78.22	79.54	78.84	73.58	74.57	84.24	78.13	82.42	77.99	76.78	80.24	68.09	65.44	73.72	68.40	78.67	83.61	81.19	79.76

Sapphirine analyses

Lithology	Corona granulite				
Sample	CAT15-02				
Location	Sympl	Sympl	Sympl	Sympl	Sympl
SiO_2	12.08	12.08	12.23	11.92	12.08
TiO_2	0.00	0.00	0.01	0.00	0.00
Al_2O_3	67.51	67.62	66.58	67.23	67.09
Cr_2O_3	0.01	0.01	0.02	0.00	0.00
FeO	1.76	1.73	1.64	1.77	1.66
MnO	0.01	0.02	0.00	0.00	0.03
MgO	19.13	19.44	19.06	18.84	19.28
CaO	0.04	0.03	0.03	0.05	0.05
Na_2O	0.00	0.00	0.00	0.02	0.00
K_2O	0.00	0.01	0.00	0.00	0.02
Total	100.55	100.93	99.57	99.81	100.21
Si	0.70	0.69	0.71	0.69	0.70
Ti	0.00	0.00	0.00	0.00	0.00
Al	4.58	4.58	4.56	4.60	4.57
Cr	0.00	0.00	0.00	0.00	0.00
Fe^{+2}	0.08	0.08	0.08	0.09	0.08
Mn	0.00	0.00	0.00	0.00	0.00
Mg	1.64	1.66	1.65	1.63	1.66
Ca	0.00	0.00	0.00	0.00	0.00
Na	0.00	0.00	0.00	0.00	0.00
K	0.00	0.00	0.00	0.00	0.00